



ScuDo

Scuola di Dottorato - Doctoral School  
WHAT YOU ARE, TAKES YOU FAR



Doctoral Dissertation

Doctoral Program in Mechanical Engineering (31<sup>st</sup> cycle)

# Experimental and theoretical investigation of under-platform dampers

By

**Muhammad Umer**

\*\*\*\*\*

**Supervisor(s):**

Prof. Daniele Botto

**Doctoral Examination Committee:**

Prof. Xu Chao, Northwestern Polytechnical University, China

Prof. Matthew Robert Brake, Rice University, USA

Politecnico di Torino

2019

## **Declaration**

I hereby declare that, the contents and organization of this dissertation constitute my own original work and does not compromise in any way the rights of third parties, including those relating to the security of personal data.

Muhammad Umer  
2019

\* This dissertation is presented in partial fulfillment of the requirements for **Ph.D. degree** in the Graduate School of Politecnico di Torino (ScuDo).

*I would like to dedicate this thesis to my loving parents*

## **Acknowledgements**

First and foremost, I would to thank my PhD Supervisor Prof. Daniele Botto whose guidance, trust and continuous support helped me to carry out this research activity. I highly appreciate his ideology to provide the intellectual freedom to his student, which assisted me to improve significantly as a researcher. Thank you for being so kind and supportive in all the matters. I would also like to express my profound gratitude towards the most senior Prof. Muzio Gola of our research group, whose priceless advice and useful comments were always there throughout my research journey. Moreover, I would like to thank all the AERMEC research group members Prof. Stefano Zucca, Prof. Christian Firrone, Prof. Teresa Berruti, Dr. Mario Lavella, Dr. Chiara Gastaldi, Dr. Giuseppe Battiato and Dr. Farhad Alinejad for providing me a great working environment with useful technical and general discussions.

I extend my gratitude towards the Higher Education Commission of Pakistan for providing me scholarship for higher studies. The support from my department and the administrative staff was also phenomenal.

Next I would like to thank my parents and my family whose love, prayers and encouragement got me going through all the times. I can,t forget to mention here the the whole family of uncle Rahat Ashfaq whose care, affection and trust helped me to reach this milestone. Especially, I would like to emphasize the confidence and belief given to me by uncle Rahat Ashfaq which provided me the very foundation of this career. Last but not the least, a special thanks goes to my wife Iqra and my lovely son Mohid Umer who brought me the great happiness of my life during my PhD. Without their love and company, this journey wouldn't have been so pleasant.

## **Abstract**

In the field of turbomachinery, the most common failure of the turbine blades is High Cycle Fatigue (HCF) caused by the fluctuating stresses at the blade resonance conditions. Due to the tremendous environment inside the turbine, a blade with resonance-free working range is not possible. HCF in the turbines is so malignant in nature that a very small crack invisible to the naked eye on a single blade can lead to a complete failure of the engine. Therefore, one of the prime concerns of designers is to limit these stresses and overcome these kinds of failures. In this regard, different friction damping devices e.g. shrouds, lacing wires, ring dampers and under-platform dampers are introduced in the system to reduce the response amplitude of the blades by dissipating their vibration energy.

In this thesis, an extensive experimental as well as numerical based research activity has been carried out to investigate the under-platform dampers. Due to the complex nature and locally introduced nonlinearities by the friction, simulation and prediction of the damper behavior is still an open problem. In all numerical modeling techniques of the under-platform dampers, information corresponding to the damper contact parameters are complementary. A novel test rig has been developed in this thesis, which is capable to directly measure the damper contact forces and relative displacement, in addition to the measurements of the blade standard FRFs. These direct measurements are then post-processed to estimate the equivalent contact parameters and for the very first time, an attempt has been made to relate the local/contact behavior of the damper in terms of contact parameters with the macro dynamic/global behavior of the damper-blade system in terms of frequency response variation. This newly proposed idea of associating the local/contact and macro behavior of the dampers provides a distinct and more realistic prospect of studying the under-platform dampers.

Moreover, during this activity, a dummy blade was also developed to test the semi-cylindrical dampers and verify the working potential and accuracy of this novel test rig by comparing the results obtained on a different test rig for the same damper. Finally, the measured contact forces are used as external forces in the numerical model of the blade and the final results are validated with the experimentally measured frequency response of the blade.

# Contents

<b>List of Figures</b>	<b>xi</b>
<b>List of Tables</b>	<b>xix</b>
<b>1 Introduction</b>	<b>1</b>
1.1 Background and motivation . . . . .	1
1.2 State of the Art . . . . .	3
1.2.1 Damper-blade Numerical Investigation . . . . .	4
1.2.2 Experimental Investigation of UPDs . . . . .	11
1.3 Objectives and Dissertation Layout . . . . .	17
<b>2 Novel test rig design for under-platform dampers</b>	<b>21</b>
2.1 Introduction . . . . .	21
2.1.1 Background and motivation . . . . .	21
2.1.2 Basic test rig design criteria . . . . .	23
2.2 Design of the test rig . . . . .	23
2.2.1 Clamping of the blade on the test rig . . . . .	24
2.2.2 Contact Force Measurement system . . . . .	28
2.2.3 Design of the L-Separator . . . . .	28
2.2.4 Modeling of the L-separator . . . . .	31

---

2.2.5	Calculation of contact forces . . . . .	32
2.2.6	Contact force measurement accuracy . . . . .	34
2.3	Electronic Instrumentation connected to the rig . . . . .	40
2.4	Final assembly and overall characteristics of the test rig . . . . .	41
2.5	Experimental setup . . . . .	41
2.5.1	Blade Excitation . . . . .	42
2.6	Conclusion . . . . .	44
<b>3</b>	<b>Design of the Dummy Blade</b>	<b>46</b>
3.1	Introduction . . . . .	46
3.1.1	Problem Specification . . . . .	47
3.1.2	Modeling of the blade . . . . .	47
3.1.3	FE Modal Analysis of the blade . . . . .	48
3.1.4	Design of removable blade-platform . . . . .	51
3.1.5	Assembly of the dummy blade on the Test Rig . . . . .	52
3.2	Conclusions . . . . .	54
<b>4</b>	<b>Model Identification and model order reduction of blades</b>	<b>55</b>
4.1	Introduction . . . . .	55
4.2	Dummy blade model . . . . .	56
4.2.1	Dummy blade model order reduction . . . . .	59
4.3	Real blade model . . . . .	62
4.3.1	Real blade model order reduction . . . . .	64
4.4	Conclusion . . . . .	65
<b>5</b>	<b>Investigation of dummy Blade dynamics in presence of dampers</b>	<b>68</b>
5.1	Introduction . . . . .	68



---

5.2	Experimental Procedure and Measurements . . . . .	69
5.2.1	Testing Conditions . . . . .	69
5.2.2	Measured Quantities . . . . .	70
5.2.3	Derived Quantities . . . . .	71
5.3	Results and Discussion . . . . .	73
5.3.1	Understanding the puzzling FRFs with measured hysteresis loops . . . . .	75
5.3.2	Experimental results comparison of two independent test rigs	77
5.3.3	Blade platform motion reconstruction . . . . .	81
5.3.4	Numerical simulation of the damper performance . . . . .	82
5.4	Conclusions . . . . .	83
<b>6</b>	<b>Contact force measurements and contact parameters estimation</b>	<b>86</b>
6.1	Introduction . . . . .	86
6.2	Damper Contact Forces . . . . .	88
6.3	Estimation of Contact Parameters . . . . .	92
6.3.1	Nonlinear SDOF model . . . . .	94
6.4	Novel method to associate the contact parameters with the blade dynamic . . . . .	97
6.4.1	Results and observations . . . . .	97
6.5	Conclusions . . . . .	103
<b>7</b>	<b>Effect of contact force harmonic variation on the blade response</b>	<b>105</b>
7.1	Introduction . . . . .	105
7.2	Forced response calculation . . . . .	105
7.2.1	Experimental and Numerical blade frequency response comparison . . . . .	107
7.3	Conclusions . . . . .	113

<b>8</b>	<b>Conclusions</b>	<b>116</b>
8.1	Conclusions on the Test Rig capabilities . . . . .	116
8.2	Linear Numerical Blade models . . . . .	117
8.3	Dummy Blade investigation . . . . .	118
8.4	Real Turbine Blade investigation . . . . .	119
8.5	Future Work . . . . .	121
	<b>Bibliography</b>	<b>123</b>
	<b>Appendix A Appendix to Chap. 2</b>	<b>133</b>
A.1	Sensors . . . . .	133
A.2	Friction loss calculation in the blade clamp . . . . .	134
A.3	Contact force formulation . . . . .	136
A.3.1	ODD SIDE . . . . .	136
A.3.2	EVEN SIDE . . . . .	139
A.4	Important things to consider before experiments . . . . .	141
A.5	Overall characteristics of the Novel Test Rig . . . . .	143
	<b>Appendix B Appendix to Chap. 3</b>	<b>151</b>
B.1	Design details of the Dummy blade . . . . .	151
	<b>Appendix C Appendix to Chap. 4</b>	<b>154</b>
C.1	Dummy blade FE Model . . . . .	154
C.2	Real blade FE Model . . . . .	155
	<b>Appendix D Appendix to Chap. 6</b>	<b>156</b>
D.1	Experimental procedure to measure FRFs and Hysteresis Loops . . .	156
D.2	Rigid rotation of the damper . . . . .	157

# List of Figures

1.1	Fatigue failure of a turbine blade . . . . .	2
1.2	Three different Under platforms placed between two consecutive blades . . . . .	3
1.3	working principle of under platform dampers. A relative displacement between the blade and damper instigate dry friction. . . . .	4
1.4	contact model enlisted as type A and B with their resulting hysteresis loops . . . . .	9
1.5	contact model enlisted as type C and D . . . . .	10
1.6	Frequency response of the blade without dampers (free) and with dampers at the same blade excitation level . . . . .	15
1.7	Normalized inertance peak as a function of the force ratio $F_C/F_E$ . . . . .	16
1.8	Normalized resonance frequency as a function of the force ratio $F_C/F_E$ . . . . .	16
1.9	Hysteresis loops of the tangential contact force (friction force) as function of relative displacement . . . . .	18
2.1	Damper-Only test rig with semi-cylindrical damper installed on the rig. Left platform is connected with the piezo electric actuator while the right platform connected with the sub-assembly of two load cells measuring contact forces [1] . . . . .	22
2.2	A top and section views of the test rig to present the its details . . . . .	25
2.3	An enlarged section-view of the clamp mechanism showing arrangement of the wedge blocks and inner parts of the assembly . . . . .	25

2.4	Design of the blade adapter with a fir-tree dove tail groove to fix a blade on the rig . . . . .	27
2.5	Assembly of two dampers on a single blade at their nominal positions and contact forces representation at damper static equilibrium condition. . . . .	29
2.6	Architect of the test rig to replicate the configuration of damper-blade contact setup of an actual turbine . . . . .	29
2.7	A complete sub-assembly of odd side contact forces measuring system and nominal contact point on L-separator . . . . .	30
2.8	Even side contact forces measuring system . . . . .	30
2.9	Basic model and dimensional details of the L-Separator . . . . .	31
2.10	defining the design point for L-Separator by plotting degree of separation of the forces with respect to its dimensional parameters. . . . .	32
2.11	FE model of L-Separator with load cell assembly. Eccentricity $e$ depicts the misalignment error of contact forces due to limitation in manufacturing accuracy. . . . .	33
2.12	Details of contact forces on the load cells LC11/LC13 odd side. Positive forces and angles are shown . . . . .	34
2.13	Details of contact forces on the load cells LC12/LC14 even side. Positive forces and angles are shown . . . . .	35
2.14	Images taken on the rig to measure directly the contact and other geometrical angles by post processing with "NI image builder" software. . . . .	39
2.15	Top view of finally assembled test rig with a real turbine blade and dampers . . . . .	41
2.16	The front view of the blade with two dampers in their nominal position. The damper on the left is hidden inside a cavity . . . . .	43
2.17	configuration-I with data acquisition-I(DAS-I) to measure the amplitude response of the blade as a function of excitation frequency with and without dampers. . . . .	43

---

2.18	configuration-II with data acquisition-II (DAS-II) to measure the static and dynamic contact force components of the dampers and relative displacement of the contact interfaces. . . . .	44
2.19	A combined layout of both data acquisition systems to highlight the additional experimental evidences available on this novel test rig, along with the commonly measured FRFs . . . . .	45
3.1	Final sketch of the dummy blade . . . . .	48
3.2	Initial design of the blade with variable and fixed geometry parameters	49
3.3	Variation in blade fundamental frequencies w.r.t it variable length at thickness $t=12\text{mm}$ . . . . .	50
3.4	First 6 natural frequencies and their corresponding mode shapes of the dummy blade . . . . .	51
3.5	Dummy blade FEM modal analysis, first two mode shapes . . . . .	52
3.6	Dummy blade with its removable contact pad . . . . .	53
3.7	Dummy blade and damper assembly on the rig with platforms and shaker . . . . .	53
3.8	Assembly the shaker with stinger on the blade at an inclination of 30deg with the horizontal to avoid touching the table . . . . .	54
4.1	Measured FRFs with impact hammer test on the dummy blade for different levels of the blade clamping force . . . . .	57
4.2	Effect of the different clamping force on the response amplitude and shift in frequency of the dummy blade . . . . .	57
4.3	Measured FRFs of the dummy blade at clamp force 50KN . . . . .	59
4.4	Selected root nodes to match the numerical and experimental dynamic response of the blade without dampers . . . . .	60
4.5	Finite element meshed model of the dummy blade with the selected excitation, contact and response nodes as master nodes . . . . .	61

4.6	3D spring compliance introduced in the blade numerical model to include the effect of the compliance of the clamp adapter . . . . .	63
4.7	Blade root areas in contact with blade adapter at final clamp position	63
4.8	Finite element meshed model of the real blade with the selected excitation, contact and response nodes as master nodes . . . . .	66
4.9	Comparison between the experimental and numerical FRFs at fundamental frequency of the real blade without dampers . . . . .	67
5.1	Assembly of the dummy blade with two semi-cylindrical dampers on the test rig. Each damper forms the flat on-flat and cylinder on-flat contact interfaces with the blade and ground platform respectively .	69
5.2	Overall set-up of the test rig (a) applied static damper force $F_C$ , applied blade excitation force $F_E$ and measured contact damper contact forces (b) pointing laser beams to record the blade platform in-plane motion (c) to measure the contact relative displacement along tangential direction at the flat on-flat and cylinder on-flat contact interfaces . . . . .	70
5.3	Static equilibrium of the forces on both blade side semi-cylindrical dampers. $T_{cyl}$ or $T_{flat}$ and $N_{cyl}$ or $N_{flat}$ are the tangential and normal contact forces of the cylindrical/flat damper contact respectively . .	72
5.4	Frequency response function at damper static load level of $F_C$ 46N (a) free blade without any dampers and (b) blade with dampers. Investigation of several excitation force levels $F_E$ . . . . .	77
5.5	Comparison of the measured and simulated hysteresis cycles along the damper cylindrical contact, with refer to the working conditions shown in 5.4 . . . . .	78
5.6	Frequency response functions (FRFs) of the damped-blade system: (a) applied static load on the dampers $F_C = 26$ N and (b) applied static load on the dampers $F_C = 66$ N . . . . .	78

---

5.7	(a) Comparison of frequency response function and (b) hysteresis loops at the damper cylindrical contact with different initial conditions. In the comparison the dampers were loaded with $F_C = 46\text{N}$ , and the blade was excited with a force $F_E = 20\text{ N}$ . . . . .	79
5.8	Damper force equilibrium , the corresponding FRFs and hysteresis loops at given load conditions are shown in Fig. 5.7; force scale shown in the figure. . . . .	79
5.9	(a) Force ratio between the tangential an normal force component and (b) hysteresis loop along the cylinder on-flat contact interface (excitation force level $F_E = 100\text{ N}$ ; static load on dampers $F_C = 46\text{ N}$ ). (c) Comparing the slopes of the hysteresis loops at the cylinder on-flat contact interface of the same damper measured on the two different and independent test rigs. . . . .	84
5.10	Reconstruction of the in plane motion of the blade: (a) free blade with excitation force level $F_E = 5\text{ N}$ , (b) damper loaded with static load level $F_C = 46\text{ N}$ and blade excitation force level $F_E = 5\text{ N}$ and (c) damper loaded with static load level $F_C = 46\text{ N}$ and excitation force level $F_E = 100\text{ N}$ (c) . . . . .	85
5.11	Numerical model of the damper . . . . .	85
5.12	Comparison of the measured and simulated damper force equilibrium (a) Measured and (b) simulated contact forces on the damper for $F_C = 46\text{ N}$ and $F_E = 100\text{ N}$ . . . . .	85
6.1	Actual turbine blade with two cylindrical dampers. On the right side a damper front and top views are enlarged to show its dimensions . .	87
6.2	Static forces on the odd side . . . . .	89
6.3	Static forces on the even side . . . . .	90
6.4	Frequency response of the blade without dampers and with dampers loaded with $94\text{ N}$ . . . . .	91

6.5	results of the best fit performed in Loading and UnLoading condition with centrifugal force $F_C = 94$ N. The objective function is a single degree of freedom model. Modal stiffness and damping are reported also for blade without dampers. . . . .	92
6.6	Top and front view of the damper-blade assembly with differential laser points to measure the tangential relative displacement between the damper and blade . . . . .	93
6.7	hysteresis loops measured in Loading and UnLoading conditions. The equivalent stiffness (slope) is reported for both conditions. The applied centrifugal force is 94 N. . . . .	93
6.8	a) Nonlinear single degree of freedom system with Jenkin contact element b) linearized equivalent system with equivalent contact stiffness $K_{eq}$ and damping $C_{eq}$ . . . . .	95
6.9	Result comparison between the linear and equivalent nonlinear system	96
6.10	Variations in numerically computed equivalent contact stiffness and damping w.r.t force ratio for the system shown in Fig.6.8 a. In stick region the contact behaves as a simple spring and no additional damping is added to the system. . . . .	96
6.11	A graphical representation of the strategy to associate the damper contact behavior with the macro-dynamic behavior of the damper-blade system . . . . .	98
6.12	Frequency response of the blade without damper (Free) and with dampers loaded with different static force $F_C$ . The excitation force $F_E$ is 1N in all cases. . . . .	99
6.13	Inertance peak as a function of the force ratio $F_C/F_E$ . . . . .	100
6.14	Resonance frequency as a function of the force ratio $F_C/F_E$ . . . . .	100
6.15	Measured hysteresis loops for different excitation force levels at damper static load $F_c=96$ N . . . . .	101
6.16	Relationship between resonance frequencies and contact stiffness at different excitation levels and different static load $F_C$ . . . . .	101



6.17	Estimated equivalent contact stiffness $K_{eq}$ for three damper static load levels $F_C$ . . . . .	102
6.18	Relationship between blade response amplitude and contact damping at different excitation levels and different static load $F_C$ . . . . .	102
6.19	Variations in experimentally measured equivalent contact stiffness w.r.t force ratio, the dotted blue line shows the overall trend of the data obtained by best curve-fit method . . . . .	103
6.20	Variations in experimentally measured equivalent contact damping w.r.t force ratio, the dotted red line shows the overall trend of the data obtained by best curve-fit method . . . . .	104
7.1	Representation of the measured contact forces $F_{NL}$ of both side dampers as external forces on the blade along with its general excitation force $F_E$ . . . . .	107
7.2	(a) Difference between the numerical and experimental results while both dampers are placed, $F_C = 26\text{N}$ , error example-2. (b) Difference between the numerical and experimental results while both dampers are placed, $F_C = 26\text{N}$ , error example-2 . . . . .	109
7.3	(a) Even side damper placed at its nominal position to measure contact forces. (b) Odd side damper placed at its nominal position to measure contact forces . . . . .	110
7.4	(a) Numerical and experimental result for test configuration-1 with even side dampers only (b) Numerical and experimental result for test configuration-2 with even side dampers only. . . . .	110
7.5	(a) Typical contact forces harmonic variation when only the "even" side damper is present. (b) Typical contact forces harmonic variation when only the "odd" side damper is present. . . . .	111
7.6	Error sensitivity of blade response amplitude while applying only even side contact forces measurement at $F_C = 26\text{ N}$ . . . . .	112
7.7	Comparison of numerical and experiment results for a static damper centrifugal load values $F_C = 26\text{ N}$ . . . . .	113

7.8	Comparison of numerical and experiment results for a static damper centrifugal load values $F_C = 46$ N . . . . .	114
7.9	Comparison of numerical and experiment results for a static damper centrifugal load values $F_C = 86$ N . . . . .	115
A.1	Clamp forces free body diagram. . . . .	134
A.2	Forces on the L-Separator; odd load cells LC11/LC13-1 . . . . .	136
A.3	Forces on the L-Separator; odd load cells LC11/LC13-2 . . . . .	137
A.4	Forces on the damper; odd load cells LC11/LC13-3 . . . . .	138
A.5	Forces on the damper; odd load cells LC11/LC13-4 . . . . .	138
A.6	Forces on the L-Separator; Even load cells LC12/LC14-1 . . . . .	139
A.7	Forces on the L-Separator; Even load cells LC12/LC14-2 . . . . .	140
A.8	Forces on the damper; Even load cells LC12/LC14-3 . . . . .	140
A.9	Forces on the damper; Even load cells LC12/LC14-4 . . . . .	141
A.10	load cell of shaker to control excitation force . . . . .	144
A.11	Accelerometer1 to measure blade response . . . . .	145
A.12	Accelerometer2 to measure blade response . . . . .	146
A.13	strain gage based load cell to measure the clamping force . . . . .	147
A.14	Load cell amplifiers to measure damper contact force measurements 1	148
A.15	Load cell amplifiers to measure damper contact force measurements 1	149
A.16	Differential laser polytec sensor head with vibrometer controller . .	150
B.1	dummy blade drawing 1/2 . . . . .	152
B.2	dummy blade drawing 2/2 . . . . .	153
D.1	Measuring the rigid rotation of the damper with differential laser. $p_1$ and $p_2$ are the two points on damper where the beams of differential laser are placed. . . . .	158

# List of Tables

1.1	Contact models characteristics . . . . .	8
2.1	derived contact force components on the blade and L-Separator contacts for both even and odd side. . . . .	36
2.2	Sensitivity of contact forces to the specific damper/blade geometry .	40
4.1	Comparison between the numerically computed and experimentally measured frequencies of the dummy blade without any damper . . .	58
4.2	Comparison between the numerically computed and experimentally measured frequencies of the real blade without any damper . . . . .	64
4.3	Comparison between the numerically computed and experimentally measured frequencies of the real blade without any damper . . . . .	65
5.1	List of all observed and derived quantities with refer to <a href="#">5.3</a> . . . . .	74
5.2	Comparison between the damper contact parameters measured at two different test rigs . . . . .	81

# Chapter 1

## Introduction

*“The greatest challenge to any thinker is stating the problem in a way that will allow a solution.”*

- Bertrand Russel

### 1.1 Background and motivation

Steam and gas turbines are a common source of power and thrust generation and widely used technologies in the industry. In these machines, small accidents can lead to fatal consequences such as jeopardizing human lives, and can result in an immense financial loss. Therefore, the operational safety of the turbo-machinery is a prime concern of the industries. In particular, the gas turbine blades are designed to withstand very high temperature and pressure at continuously load varying conditions. To operate in such extreme circumstances, the blades and their disks are made with high strength unconventional materials like super-alloys and ceramic matrix composites (CMCs), those also possess a high modal density [2–4]. Due to their high modal density it is unavoidable for the designers to design the blades with operating frequencies away from their resonances. Thus, a large frequency span of the fluctuating stresses resulted from the blade vibrations, can lead to a high cycle fatigue failure (HCF) of the blades at the resonance conditions [5, 6]. An example of a turbine blade with crack caused by the HCF which resulted in a shut down of a

complete engine is shown in Fig. 1.1 and is taken from [7] which states that "*a single intermediate-pressure turbine blade failed as a result of high-cycle fatigue cracking, producing high levels of vibration and the subsequent commanded shut-down of the No.4 engine.*". Therefore, in this field an imperative attribute of a turbine blade to withstand against this HCF by mitigating the vibration amplitude of the blades. However, the internal structural or aerodynamic damping of the blade is insufficient to absorb all blade vibrations in case of fluctuating stresses at such a high temperature. Nevertheless, additional damping is introduced in the blade structure in the form of friction contact damping [8–10]. Contact friction damping is an efficient technique

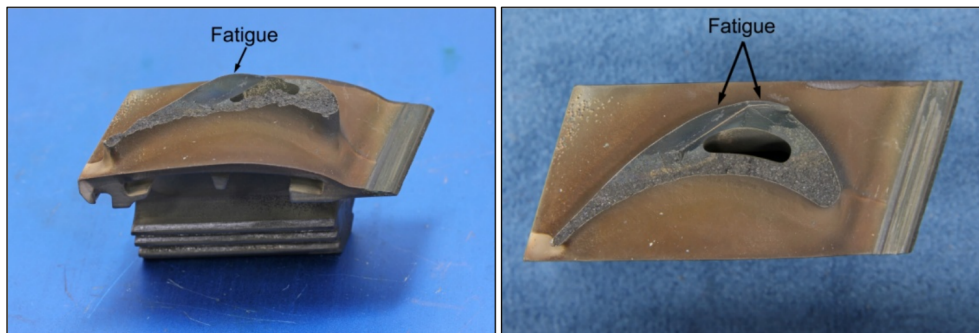


Fig. 1.1 Fatigue failure of a turbine blade

to absorb the blade vibration with dissipation of energy by virtue of friction between two interfaces at such a high pressure and temperature conditions. In addition to the friction present at the blade root interfaces [11], external contact damping sources are also introduced in the form of *under platform dampers* (UPDs), shrouds, lacing wire and damper rings etc [12]. Among the other friction damping devices, UPDs are considered to be most effective source of contact friction damping in the turbines [13, 14]. These dampers are small metallic pieces placed in the underside of two consecutive turbine blades thus also seal the gap between two adjacent blades as shown in 1.2. Moreover, unlike blade shrouds or lacing wires, any aerodynamic losses are avoided by placing these dampers on the underneath surface of the blades that isolate them from the hot gases [15]. Due to the centrifugal force produced by the rotation of the turbine, the UPDs experience an outward pulling force that ensures their contact with the bottom surface of the blade platforms as shown in the Fig. 1.3. A relative displacement induced by the vibrations of two adjacent blades instigates the sliding of damper surface on blade under-platform. The non-conservative friction

force and relative motion between the contact surfaces dissipate part of vibration energy thus reducing the oscillating amplitude of the blade[13].

To estimate the effect of resonant stresses on the fatigue life of turbine blades with and without the under-platform dampers, a numerical and experimental study has been presented in [16] in which a wheel sector, containing three blades with and three blades without under-platform dampers, was investigated. In this work [16], it was concluded that the lightest damper with chosen parameters showed 30% reduction in the resonant stresses of first mode vibrations. Moreover, as given in [17], the numerical simulations of elastic contact of vibrating parts can be further used to estimate the qualitative fatigue life prediction. However, the accuracy of this type of assessment depends upon the correctness of the contact parameters used in the numerical model.

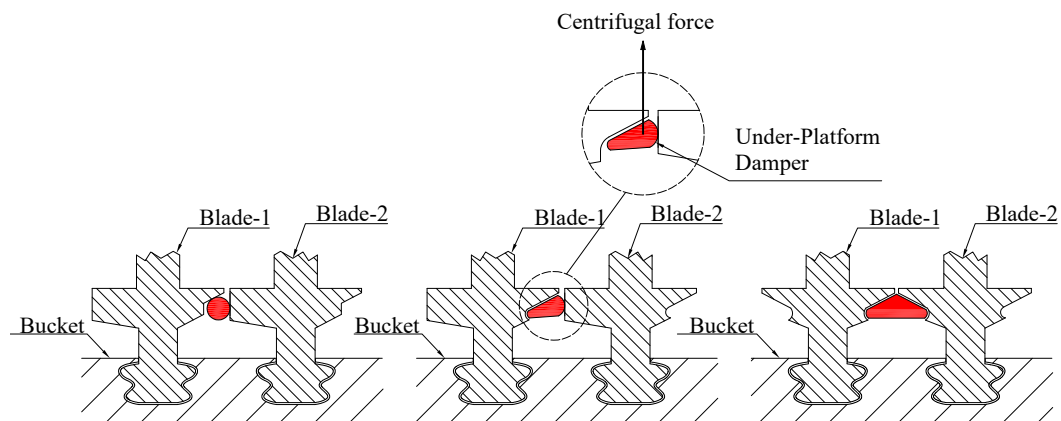


Fig. 1.2 Three different Under platforms placed between two consecutive blades

## 1.2 State of the Art

Despite the simple geometry and assembly of the under-platform dampers, the kinematics of the dampers coupled with the blade dynamics are still not fully understood yet. The complex nature of the contact friction and resulting nonlinear contact forces complicate their investigation. The solution lies in a combined numerical and experimental approach. In the proceeding subsections, a detailed introduction of the

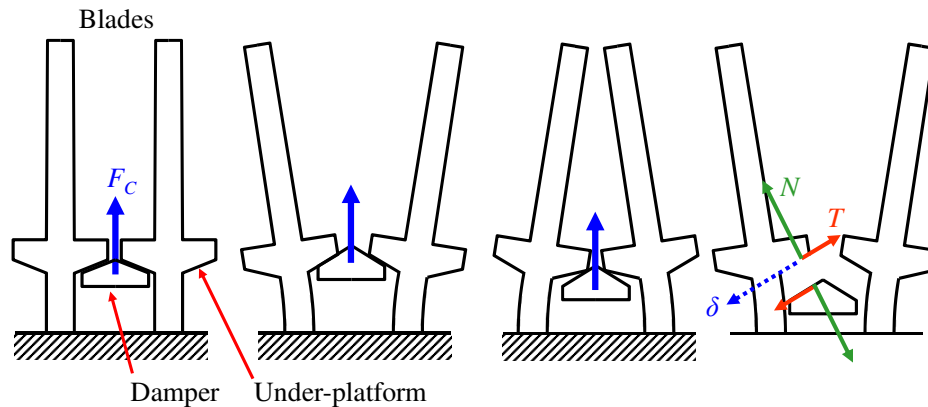


Fig. 1.3 working principle of under platform dampers. A relative displacement between the blade and damper instigate dry friction.

damper-blade numerical modeling and summary of the state of the art experimental investigations are described.

### 1.2.1 Damper-blade Numerical Investigation

Numerically modeling and designing a device, that work on the effective contact friction between the relatively vibrating surfaces, is a challenging task for the engineers. Due to locally introduced nonlinearities by the friction, simulation and prediction of the damper behavior is still an open problem. A review about modeling the bladed-disk contact friction has been presented in [18] that summarized a number of cumbersome techniques to solve a frictionally induced nonlinear system of equations. With refer to the damper geometry, commonly considered cross-section for damper are triangular also called cottage-roof/wedge-shaped damper and cylindrical dampers [19]. However, as compared to the wedge shaped damper, cylindrical damper are more susceptible to rolling effect which results in a significant loss of friction damping [13, 20]. Several comparative studies with respect to damper geometry are available [21, 22]. As referred in [23] that the damper with mixed geometry damper i.e. curved contact surface on one side and flat on the other side, is more effective. A detailed experimental and numerical study on mixed geometry dampers (curved-flat) have been performed in [24–27]. Another latest study with this perspective is presented in [28] that compares a cottage roof damper with a thin flat-flexible damper.

### Numerical techniques for fictionally damped structure

While modeling a damper-blade system, a suitable technique and mathematical formulation is required to define the contact interfaces. In this regard, the main requirement of the numerical model is to define the tangential and normal contact conditions. In the dynamic study of UPDs, two basic contact modeling strategies are usually adopted by the researchers i.e. **Dynamic Lagrange method** and **Contact Element method** also called **Penalty method**. In first technique the Dynamic Lagrange method is applied on the contact patch and contact constraints does not add any extra stiffness to the structure [29–31]. Whereas, in the method of "Contact Element/Penalty" penalty means that any violation of the contact condition will be punished by generating an opposing contact load. The only penalty operator that can produce this effect is the "Stiffness" operator. Therefore, in this method tangential and normal contact stiffnesses are introduced with a valid friction coefficient between the nodes of two contact surfaces facing each other [22, 32–34]. This approach require the determination of complex kinematics of the UPDs and a reasonable assumption of considering the damper as a rigid body.

A damper-blade system can be written in the form of nonlinear force equations as given in Eq. 1.1.

$$\mathbf{M}\ddot{\mathbf{Q}}(t) + \mathbf{C}\dot{\mathbf{Q}}(t) + \mathbf{K}\mathbf{Q}(t) = \mathbf{F}_E(t) + \mathbf{F}_{NL}(t) \quad (1.1)$$

Whereas,  $\mathbf{M}$ ,  $\mathbf{C}$  and  $\mathbf{K}$  are mass, damping and stiffness matrices respectively and  $\mathbf{Q}$  is the displacement.  $\mathbf{F}_E$  is the periodical excitation force vector and  $\mathbf{F}_{NL}$  is nonlinear contact force vector computed by the respective contact model. Nevertheless, the use of "contact element" to simulate a frictional contact is more appreciated than the former approach due to physics defined by the contact parameters which simulate the contact behavior close to the actual conditions [35–37]. Moreover, these contact parameters are easy to use and interpret in the system of equation of a vibrating structure. For this reason, the latter method is used in this thesis (in **Chap. 5**) to numerically model the damper-blade contact.

The presence of frictional force in a system of equations makes it nonlinear due to its dependency on the relative displacement and time. A common method to solve this kind of nonlinear system is to use the "Harmonic Balance method" in which



the system is linearized by considering the harmonic response of the system if it is excited by a harmonic force [38–40]. In this method, the nonlinear friction contact forces are computed as function of relative displacement between two contacting surfaces by applying a suitable contact model [22]. However, the most critical point in this method is to select the number of harmonics to represent relative displacement and contact forces. In case of frictional damper, it is common to consider only first harmonic term for the computation of the system response and this method is known as "SHBM (single harmonic balance method)". But sometimes it is not possible to compute the system response accurately by considering only first harmonic. In that case more than one harmonics are considered to represent the contact friction forces and relative displacement. However, this consideration of higher harmonics in the calculation results in high computational cost. This method is known as "multi-Harmonic balance method (MHBM)". Several efforts are made in [41–43] to identify the best possible number of harmonics with compare to the computational time. Conclusively, it is a compromise between the required level of accuracy and computational cost which is estimated through different convergence techniques. Due to periodical nature of the external force, the nonlinear system of equation given in Eq. 1.1 is solved by using MHBM method by approximating the displacement  $\mathbf{Q}$  and nonlinear forces  $\mathbf{F}_D$  with a truncated Fourier series as follows:

$$\mathbf{Q}(t) = \mathbf{Q}^{(0)} + \Re\left(\sum_{n=1}^{N_h} \mathbf{Q}^{(n)} e^{in\omega t}\right) \quad (1.2)$$

$$\mathbf{F}_E(t) = \mathbf{F}_E^{(0)} + \Re\left(\sum_{n=1}^{N_h} \mathbf{F}_E^{(n)} e^{in\omega t}\right) \quad (1.3)$$

$$\mathbf{F}_{NL}(t) = \mathbf{F}_{NL}^{(0)} + \Re\left(\sum_{n=1}^{N_h} \mathbf{F}_{NL}^{(n)} e^{in\omega t}\right) \quad (1.4)$$

Whereas,  $N_h$  is the total number of harmonics and  $\omega$  is the fundamental frequency of the external force  $F_E$ . If we consider only the first harmonic or SHBM i.e.  $N_h=1$ , these equations can be simplified as,

$$\mathbf{Q}(t) = \mathbf{Q}^{(0)} + \Re(\mathbf{Q}^{(1)} e^{i\omega t}) \quad (1.5)$$

$$\mathbf{F}_E(t) = \mathbf{F}_E^{(0)} + \Re(\mathbf{F}_E^{(1)} e^{i\omega t}) \quad (1.6)$$

$$\mathbf{F}_{\text{NL}}(t) = \mathbf{F}_{\text{NL}}^{(0)} + \Re(\mathbf{F}_{\text{NL}}^{(1)} e^{i\omega t}) \quad (1.7)$$

Furthermore, these nonlinear system of differential equations can be transformed into nonlinear algebraic equations with complex coefficients.

$$\mathbf{K}\mathbf{Q}(t)^0 = -\mathbf{F}_{\text{NL}}(t) \quad (1.8)$$

$$\mathbf{D}(\omega)\mathbf{Q}^1 = \mathbf{F}_{\text{E}}^1 + \mathbf{F}_{\text{NL}}^1 \quad (1.9)$$

$\mathbf{D}(\omega)$  is the dynamic stiffness i.e.  $\mathbf{D}(\omega) = \mathbf{K} + i\omega\mathbf{C} - \omega^2\mathbf{M}$  and  $0^{\text{th}}$  order given in Eq. 1.8 corresponds to the static balance whereas, Eq. 1.9 represents the dynamics balance of the nonlinear system.

### Different types of contact models

The next step in the numerical study of damper-blade system by penalty method is to choose a suitable contact element which represents the friction in the formulation of the problem. The contact elements used in the field of turbomachinery generally falls in the category of "spring-slider". These kind of contact elements only depends upon the relative displacement between contact interfaces (e.g. Jenkin, Iwan) and does not consider any effect of viscous forces or velocity[44–46]. The Iwan contact model is generally used for modeling the bolted joints interactions due to more precise consideration of the effect micro-slip [45, 47–49]. In the classical Iwan contact model the contact interface of the joints are modeled generally with a single or a couple of contact elements which relates the excitation amplitude variation with the dissipation of the energy and change in contact stiffnesses. Iwan model is generally classified on the bases of the assumption to consider the distribution of critical slipping force. A famous type of Iwan model called Sandia Iwan Model [47, 48] consider the distribution of the force by truncated power series and Dirac Delta function. In this model, Brake [48] introduced pinning of the bolted joint and methods to extract model parameters from the experimentally measured information. In a classical model [45, 49], the slipping force distribution is considered as uniformly distributed which means the contact pressure is considered to be maximum in the center of the contact decreasing proportionally towards the contact boundaries. Due to difficulties in the estimation of parameters of the Iwan model, tuning of the model is required for the given contact geometry or material under consideration. In general,

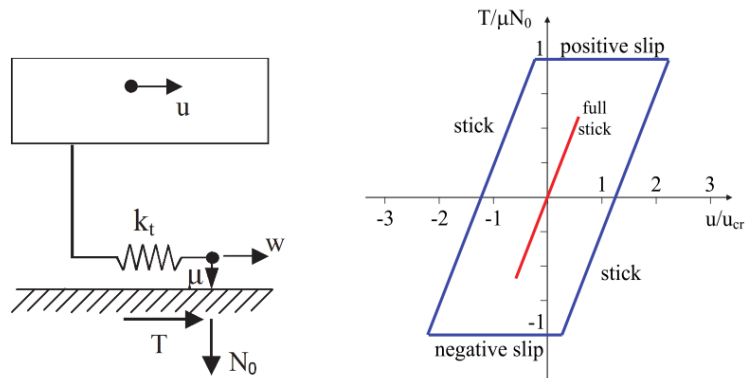
the variation in the frequency and damping of the each mode of the structure are used to tune this model [50–52]. In contrast to the generic friction contact model given in [53], the work presented in [48] does not consider the coupled in-plane and out of plane relative displacement in the model. Recently, a modified Iwan model has been presented in [54] to study the under-platform dampers in which a variable normal load is consider to define the different states of the contact. This newly proposed model has the same number of contact parameters as a classical gross-slip model. In general, a number of valid contact models commonly used to study the under-platform dampers with "spring slider" contact elements are summarized in Tab. 1.1 as follows:

Table 1.1 Contact models characteristics

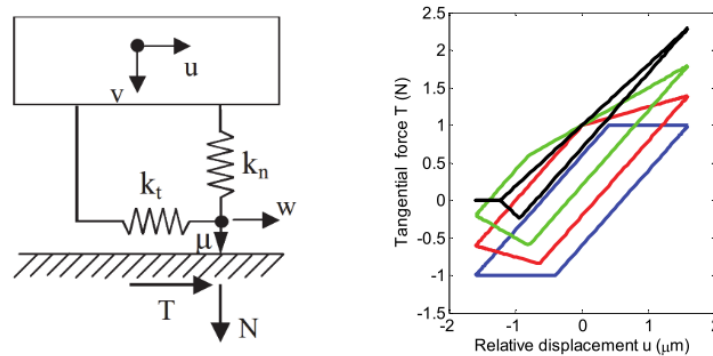
	<b>Contact Model description</b>	<b>Reference</b>
A	1D tangential relative displacement and constant normal load	Griffin 1980 [10]
B	1D tangential relative displacement and variable normal load	Yang et al., 1998 [55]; Petrov and Ewins,2003 [56]; Cigeroglu et al., 2007[33]
C	2D tangential relative displacement and constant normal load	Sanliturk and Ewins 1996 [57], Menq 1998[58]
D	2D tangential displacement and variable normal load	Yang 1998 [59]

A comprehensive study of these all models with the solved examples is given in [22]. In the above mentioned models, type A (shown in Fig. 1.4a) includes the simplest contact element called coulomb friction (jenkin element) used by Griffin [10] to model blade-to-ground damper. However, modeling the damper-blade inter-

action with this contact model are not possible due to application of constant normal load. In addition to this, the models given in category C (shown in Fig. 1.5a) also



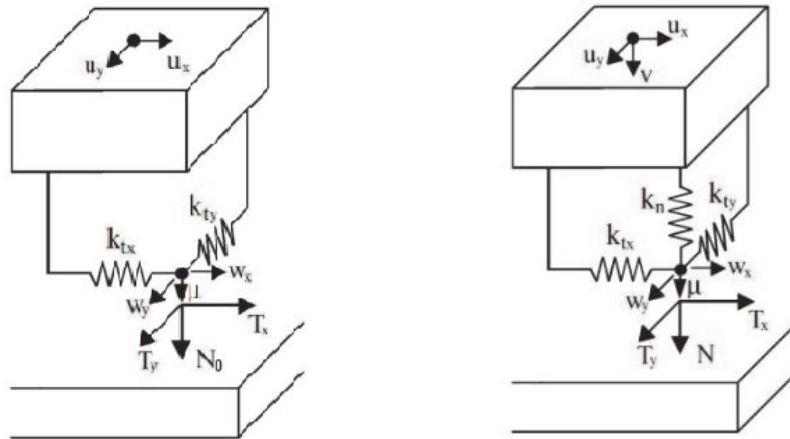
(a) 1D tangential relative displacement with constant normal load. Resulting hysteresis loops for fully stick and slip conditions are also shown.



(b) 1D tangential relative displacement with variable normal load. Resulting hysteresis loops showing the stick, slip and lift-off conditions of the contact

Fig. 1.4 contact model enlisted as type A and B with their resulting hysteresis loops

consider a constant normal load thus not suitable for the study of under-platform dampers and blade interaction. Because the under-platform dampers undergo a variable normal load which sometimes results in partial lift-off or separation between the contact surfaces. On the other hand, contact elements given in B and D (shown in Fig. 1.4b and 1.5b) are commonly used in the study of under-platform dampers [21, 23, 28, 42, 60, 61] for allowing a partial separation of the contact. Sometimes, the contact points along the contact surfaces undergo 2D relative tangential displacement and considering only 1D linear displacement while modeling these contacts can result in under-estimation of the contact damping. In that case, it is necessary to



(a) 2D tangential relative displacement with constant normal load. (b) 2D tangential relative displacement with variable normal load.

Fig. 1.5 contact model enlisted as type C and D

consider a model which allows to include the effect of friction damping along the 2D trajectory of the contact planes. To include the 2D contact kinematics in the model, two 1D contact elements given in B are utilized to combine two contact interfaces of the bodies by assuming that two perpendicular slip directions of the corresponding contacts are independent to each other. So this simplification facilitates to consider 2D tangential coupling of the contacts with help of 1D contact element [28, 40]. Although the contact element given in type D is most advanced model which includes the friction effect in in 2D trajectory of the contact planes with variable normal load but due to high computational cost this model is usually avoided by industries as affirmed by the author himself [61]. In this work in **Chap. 5**, a 2D contact model as shown in Fig. 1.5 is used.

### Reduction Techniques

In the numerical modeling, generally the finite element model of the mechanical structures are very precisely and fine meshed to accurately predict or estimate the required parameters while performing any structural analysis. But in case of nonlinear dynamic analysis, the non-linearities are generally localized in specific areas e.g. contact areas in case of contact friction. In that case, performing the complete nonlinear analysis with such a fine mesh is totally inadequate and expensive

in terms of time consumption. Therefore, one of the most important aspect of numerical simulation of the nonlinear systems is to reduce the overall size of the finite element numerical model through a suitable model order reduction technique in which all the DOFs, other than nonlinear, are deduced.

A number of different reduction methods are available in the literature [62, 63] but all of them normally based on the component mode synthesis (CMS) or classical modal analysis. The Hurty/Craig-Bampton Reduction method, also known as CB-CMS, is a commonly used technique to reduce the size of a large finite element model by acquiring the fundamental frequency modes of the structure [64, 65]. In this thesis work also this technique has been used for the reduction of the numerical model of the dummy and real blade as given in **Chap. 4**.

Although a valid reduction method successfully reduces the numerical model by an order of magnitude for all the linear DOFs of the systems but remaining nonlinear DOFs (those involve the contact) are required to be solved in full form. Therefore, the equations corresponding to the nonlinear DOFs are still required a maximum computational efforts. Nevertheless, the new model reduction techniques those also allow to reduce the nonlinear equations of locally nonlinear system are need of the time [66, 67] and do not fall in the scope of this thesis.

### 1.2.2 Experimental Investigation of UPDs

The ultimate objective of all the experimental test rigs are to measure the response amplitude of the blade and contact parameters of the damper contact interfaces. Previously, several test rigs [10, 13, 35, 61, 68–74] have been developed by the researchers to study the damping effect of under platform dampers. One of the old experimental apparatus [10] consisting a single blade/single damper was developed to measure the damper performance in terms of vibration stress reduction. The experimental results obtained on this test rig were used to assess the capability of a new contact model in [75]. Among the other test rig designs, one of the most common architect is to place a single damper between two blades [13, 35, 69–71]. In these test rigs the excitation force is applied through an electromagnetic shaker. A modified architect of the rig was proposed in [61, 72] in which a single blade was used with dampers. Each damper was in contact with the blade on one side and on

the other side of the damper with a more rigid structure called dummy blade. In all these experimental setups the centrifugal load acting on the damper was simulated by dead weights attached to the damper through wires and pulleys arrangement or solid strips.

Another way to classify these test rigs is with respect to their working (stationary or rotating). Dampers are loaded in a more realistic way if tests are performed using rotating disks. Examples of the rotating test rigs can be found in [76, 68]. The test rig given in [76] was developed to understand the under platform dampers behavior placed between two blades in vacuum conditions. This test rig focuses on structural effects brought by the coupling of two blades due to thin-walled dampers only. A full blisk rotating test rig is given in [68] where a cottage-roof dampers have been tested. However, for some reasons, in this test rig [68], the dampers got stuck to one side of the platform thus resulting in unsteady response during testing. To overcome this uncertainty and complexity of the rotating rig, a more complex test rig static full blisk rig was developed by Berruti in [77] in which 24 blades assembly was excited with a rotating excitation force to investigate the damper behavior at different nodal diameters of the disk. The contact-less traveling excitation force is produced by the electromagnets placed under each blade of the blisk. In this test rig, the phase shift in the traveling excitation wave provides a facility to excite the blisk with the desired engine order and the dampers were loaded with dead weights as well. In [68] and [71] the excitation force was applied by employing a permanent magnet and electromagnet respectively, thus also introducing a contact-less excitation source alike [77]. Similarly, in [61, 72, 73] the excitation force was applied by the air jet to avoid any direct interaction of the excitation source with the blade.

All the previously cited experimental setups mainly study the overall effect of the damper on the blade in terms of vibration amplitude reduction and resonant frequency shift. Nevertheless, this black-box like approach of FRFs measurement is worthwhile to evaluate the capability of the damper to reduce resonant displacements but it does not allow a better understanding of the behavior of the damper. These test rigs are not capable of analyzing the dynamics of the damper in depth, nor its kinematics in terms of damper/under-platform relative displacement. A first attempt to improve the understanding of the damper kinematic behavior was done in [78] where the relative displacement and rotation of the damper was measured by placing a couple

of laser beams on the underside of the damper. Later in [79], another investigation was performed to measure the damper rotation in addition to the standard frequency response function measurements. Yet the contact forces were not measured in these investigations. On the other side, a number of test rigs [80–84] were developed to measure the contact parameters, namely friction coefficient and tangential contact stiffness, in controlled laboratory conditions. Although the normal and tangential contact stiffnesses of a complex geometry can be estimated by simulating the contact as in [85, 86] an experimental measurement of these parameters is the most reliable option. There are few other numerical and experimental based procedures available in the literature to estimate the normal and tangential contact stiffness as described in Sec. 1.2.2.

The need for determination of the contact parameters in the working conditions close to reality led to the first Damper Test Rig developed at AERMEC laboratory<sup>1</sup>. A different type of test rig which does not include any real blade was developed to study the UPDs kinematics. This rig, called "Damper Only Rig", was built in 2008 [1] and was a first step towards a deep investigation of dampers behavior. Since then, the test rig has been used to investigate the behavior of several dampers in terms of kinematics and force transmission characteristics [26, 87]. In this test rig two contact surfaces, simulating the under platforms of the right and left blades, were moved with a given displacement profile through two piezo actuators. The relative motion between the damper and the under-platform like contact surface was measured with a differential laser vibrometer. Moreover, a pair of strain gages load cells were used to measure the contact forces on one contact surface of the damper. The contact forces on the other contact surface was deduced by calculation.

A numerical model of the damper/test-rig system was first presented in [20], together with the first version of the contact parameters estimation procedure, subsequently improved in [25]. In this test rig, the dynamic effect of an actual blade on the damper was not present. Due to this limitation of the "Damper Only Rig", a new test rig has been developed and commissioned as a part of this thesis work which includes a real blade with two platform dampers, a similar architect used by [61, 72]. Unlike [61, 72], the first Damper Only Rig [1] and the novel test rig called Damper+Blade Rig (first presented in [88] and thoroughly described in **Chap.**

<sup>1</sup><http://www.aermec-dimec.polito.it/>



2) share the same ultimate goal: measuring the hysteresis cycle produced by the damper between the platforms. However, their structure and working principles are different. In the first rig [1] the trajectory and amplitude of the input motion can be finely controlled by means of two piezo actuators connected to a dummy platform (no blades are present). However the frequency range the rig can explore is limited (lower than 160 Hz). Whereas, in the novel test rig the motion is achieved by exciting a blade at resonance with an electromagnetic shaker. Due the presence of a real blade, the effect of the blade dynamics on the performance of the dampers can be investigated. As the relative motion between the damper and blade depends upon the dynamics and mode shape of the blade vibration, the variety of platform kinematics the user can investigate is limited in this novel test rig. However, the rig is excited in the frequency range actually encountered by the blades mounted on a real working engine. Furthermore, in this second rig it is possible to directly measure the effect of the damper hysteresis cycle on the blade amplitude of vibration.

### **Damper performance Curves**

In the study of under-platform dampers, standard Frequency Response Functions (FRFs) of the blade are measured to evaluate their damping capabilities. Example of such FRFs, with and without the dampers, are shown in Fig. 1.6. The curve denoted as "Free" is the response of the blade without any dampers.

For the given FRFs, it can be seen that under-platform dampers exhibit significant reduction in response amplitude of the blade and also result in shift in frequency. For a given excitation force, increase in the normal static load on the dampers results in increase in the blade resonance frequency and response amplitude until the damper reaches to a stick condition.

From these FRFs it is possible to develop amplitude and frequency damper performance curves which represent the amplitude or frequency shift with the ratio of the damper static load to blade excitation force level. The damper performance curves, namely 'amplitude peak' and 'frequency shift', are produced from these FRFs of the blade [89–92]. More specifically, the amplitude performance curve plots the maximum amplitude response (displacement, velocity or acceleration) of the blade against the ratio between the applied static load on the dampers to excitation force  $F_C/F_E$ . Whereas, the frequency performance curve presents the shift

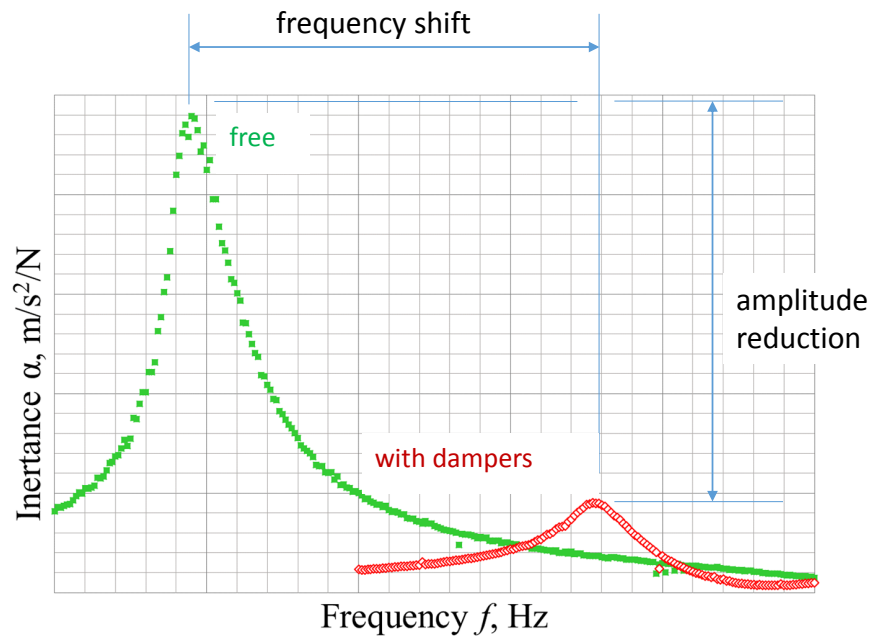


Fig. 1.6 Frequency response of the blade without dampers (free) and with dampers at the same blade excitation level

of the resonance frequency with respect to the same force ratio  $F_C/F_E$ . Amplitude performance curve are also sometimes called damper optimization curve. The idea of damper performance curves was first introduced by Cameron in [93]. This a graphical representation of the experimental data assist the designer to identify a design point for under-platform dampers independent from the excitation or viscous damping.

These performance curves are used to define an optimal static load to excitation force ratio ( $F_C/F_E$ ) at which the amplitude response of the blade is minimum. If this ratio is too high the damper will tend towards *fully stick condition* and there will be zero or negligible relative displacement between the damper and blade as also mentioned in [72, 94, 95]. Therefore, at *fully stick condition* no contact damping is available to dissipate the energy. In that case, any reduction in response amplitude or shift in frequency of the blade is mainly caused by increase in contact stiffness through applied static load on the dampers. Example of the amplitude and frequency shift damper performance curves are shown in Fig. 1.7 and 1.8, however, the recently developed curves from the measurements on real damper-blade system, during this research activity, can be find in **Chap. 6** Sec. 6.4.1.

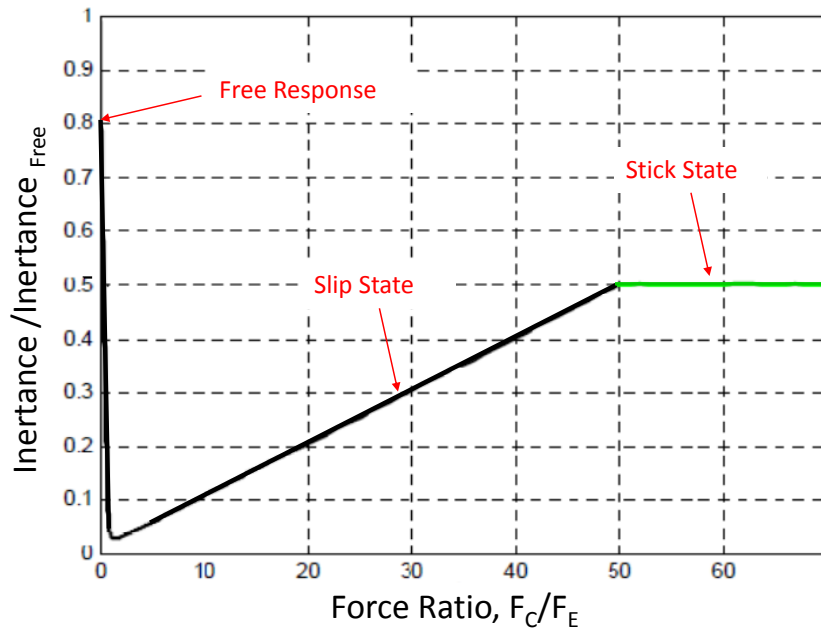


Fig. 1.7 Normalized inertance peak as a function of the force ratio  $F_C/F_E$

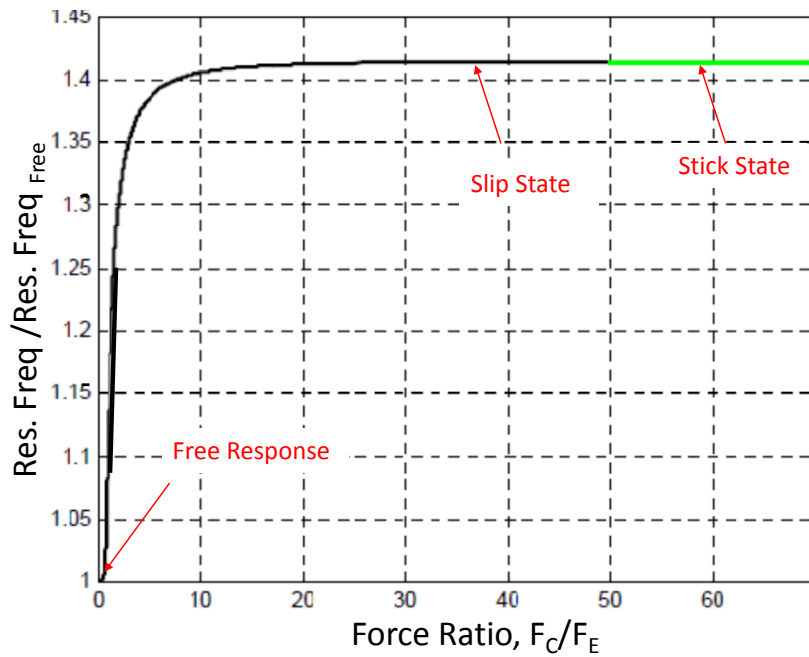


Fig. 1.8 Normalized resonance frequency as a function of the force ratio  $F_C/F_E$

### Contact Parameters

Experiments clearly show that the contact parameters strongly affect the damping potential of the under-platform dampers [42, 68, 96]. In the numerical model

validation of the damper-blade system, usually the FRFs and damper performance curves are the only available experimental information. Generally, a constant value of the friction coefficient is assumed and then fine-tuned to match the experimental frequency response functions. The numerical model validation of the damper-blade system requires contact parameters to be used in the contact model to validate the numerical results with experimentally measured FRFs using data matching technique. These contact parameters include normal and tangential contact stiffness and friction coefficient. Due to indeterminate nature of the contact problem, more than one set of contact parameters can give us the same results as also explained in [97]. Therefore, the FRFs and damper performance curves are not sufficient to obtain an in-depth behavior of the damper contact and it is not possible to estimate contact parameters from the measured FRFs/damper performance curve only and the contact parameters require much closer attention if the damper model is to be safely validated and then used during the design stage. Nevertheless, selecting accurate contact parameters for the corresponding contact model are vital to solve the system of nonlinear equations. A significant part of this research activity is dedicated to accurately measure and estimate the contact parameters for under-platform dampers. In the field of friction contact the characteristics of the contact are described by the well-known hysteresis loop. The hysteresis loop presents the tangential contact force as a function of the oscillating in-plane relative displacement or velocity between the two contact surfaces [98, 99]. These characteristics determine the stiffness and damping capabilities of a contact. A general representation of hysteresis loop is given in Fig. 1.9 in which the different states and characteristics of the contact interface are described. A numerical method has been put forward in **Chap. 6** to estimate the equivalent damping and stiffness of the contact from the measured hysteresis loop.

### 1.3 Objectives and Dissertation Layout

The overall objective of this research is to deeply investigate the damper-blade contact behavior and highlight the effect of contact parameters on the frequency response of the blade. Nevertheless, a number of sub-objectives are set during this research activity to successfully achieve this ultimate goal:

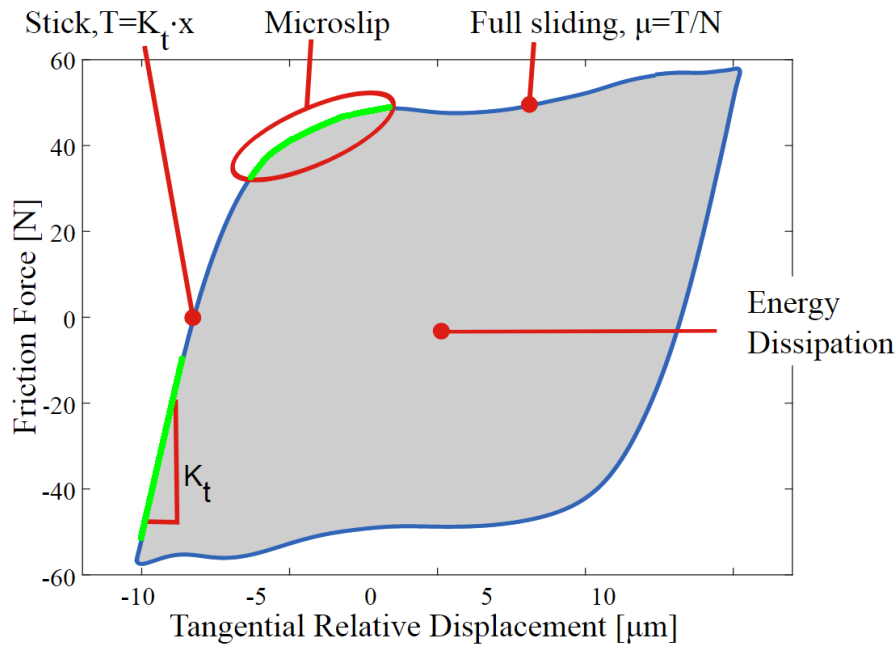


Fig. 1.9 Hysteresis loops of the tangential contact force (friction force) as function of relative displacement

- to develop and commission a new test rig that should possess the capability to measure the contact forces and relative displacement between the damper and blade contact interfaces.
- to investigate the working of semi-circular damper to understand the nonlinear dynamic response of the damper-blade system. To study this damper, a dummy blade with well defined modal properties and suitable damper contact interfaces, was developed. In this investigation, the measured contact parameters of this semi-cylindrical damper are compared with previously measured contact parameters of the same damper on a different test rig. Moreover, the experimental results are simulated with a damper-blade numerical model for a true validation.
- to introduce a novel approach to associate the macro dynamic/global behavior of the damper-blade coupled system, i.e variation in frequency response of the blade, with the local/contact behavior of their contact interface. This newly proposed idea provides a different and more realistic prospect of studying the under-platform dampers. Furthermore, as a supplementary task, a numerical method has been presented to accurately estimate the equivalent

contact stiffness and damping from the measured contact forces and relative displacement.

- to study the numerical model of the blade where measured contact forces are applied as external forces on the blade contact interface thus allowing to bypass hard computation of the nonlinear contact forces.

The above mentioned objectives and in-depth details of this research are presented in this dissertation with the following layout:

### **Chapter 2. Novel test rig design for under-platform dampers**

This chapter includes a detailed description of newly designed test rig (as briefly explained in Sec. 1.2.2). This includes some preliminary numerical simulations and calculation for the different test rig parts. Moreover, working principle of the different test rig mechanisms and some important aspects to obtain the valid experimental data are also explained.

### **Chapter 3. Design of the Dummy Blade**

In this chapter, a design of dummy blade has been explained which was purposely developed to test the semi-cylindrical damper.

### **Chapter 4. Model Identification and model order reduction blades**

In this chapter, the supplementary procedures required to obtain the dynamically correct linear numerical model of the blades (without dampers) has been explained. This FE numerical model represents the actual blade assembled on the rig. Moreover, the procedure used to do the model order reduction (Sec. 1.2.1) of the two blades (used in this thesis) has been explained.

### **Chapter 5. Investigation of dummy Blade dynamics in the presence of dampers**

In this chapter, a semi-cylindrical damper is tested on this novel test rig and measured contact parameters (Sec. 1.2.2) of the damper are compared with the previously

obtained results taken on an old test rig. Additionally, the kinematics and blade platform motion are reconstructed using ‘instantaneous center of mass’ approach to understand the transition of the contact during testing and its effect on the damper performance.

### **Chapter 6. Contact force measurements and contact parameters estimation**

In this chapter, a real blade with two cylindrical dampers has been studied. In the first part of this chapter, the effect static contact force component on the response of the blade has been investigated. Moreover, a numerical method has been explained to estimate the equivalent contact parameters, i.e. damping and stiffness, from the measured hysteresis loops as discussed in Sec. 1.2.2. In the final part, for the very first time an attempt has been made to associate the local behavior of the damper contact with the macro-dynamic/global behavior of the damper-blade system with the help of damper-performance curves (Sec. 1.2.2).

### **Chapter 7. Effect of contact force harmonic variation on the blade response**

In this chapter, the effect of dynamic component of the contact forces on the forced response calculation of the blade (Sec. 1.2.1) has been presented. In this study, the measured contact forces are applied as external forces on the numerical model of the blade, in addition to the standard shaker excitation force.

### **Chapter 8. Conclusions**

In this final chapter of the thesis, the overall conclusions are drawn by summing up the main findings and outcomes of this thesis. Furthermore, the suggestions and recommendations are included to indicate the potential future perspective of this research activity.

# Chapter 2

## Novel test rig design for under-platform dampers

*“Optimism is the faith that leads to achievement. Nothing can be done without hope and confidence.”*

- Helen Keller

### 2.1 Introduction

In this chapter the overall architect and design of a novel test rig which was purposely developed to investigate the under-plaform dampers, is presented. Different features and measurement capabilities of the rig are discussed and their working limitations in terms of measuring accuracy are explained. The presented design of this newly developed experimental setup has already been published in [88].

#### 2.1.1 Background and motivation

As mentioned earlier in Sec. 1.2.2 of the introductory chapter, the contact parameters are of prime importance in the study of under-platform dampers. Therefore, a controlled experimental test bench is required to accurately measure the inner mechanics of the damper contact interfaces. The motivation to develop a novel experimental



setup, that measures the damper contact forces as well as relative displacement, has been taken from the test rig presented in [1].

The test rig given in [1] consists a single damper placed between two dummy platforms as shown in Fig. 2.1. In that test rig, a closed loop controlled relative displacement was given to the left platform with the help of piezo-electric actuators and the contact forces of the damper are measured with two load cells ( $LC1$  and  $LC2$  as shown in Fig. 2.1 ) on the other dummy platform. In addition to the piezo-electric actuator limited working frequency range, the force measurement mechanism was also less stiff to allow the exploration of the frequency range higher than 150Hz. Above this frequency range, it was not possible to accurately control the given displacement. Moreover, in that test rig the force measurement assembly starts vibrating substantially at higher frequencies thus making it impossible to accurately measure the contact forces. Nevertheless, that test rig was first of its kind and has been extensively used to investigate the inner mechanics of the different damper in [24, 27, 100–102]. Consequently, to include an actual blade contact with the damper and overcome the above mentioned limitations of the old rig, a novel test was essential to develop.

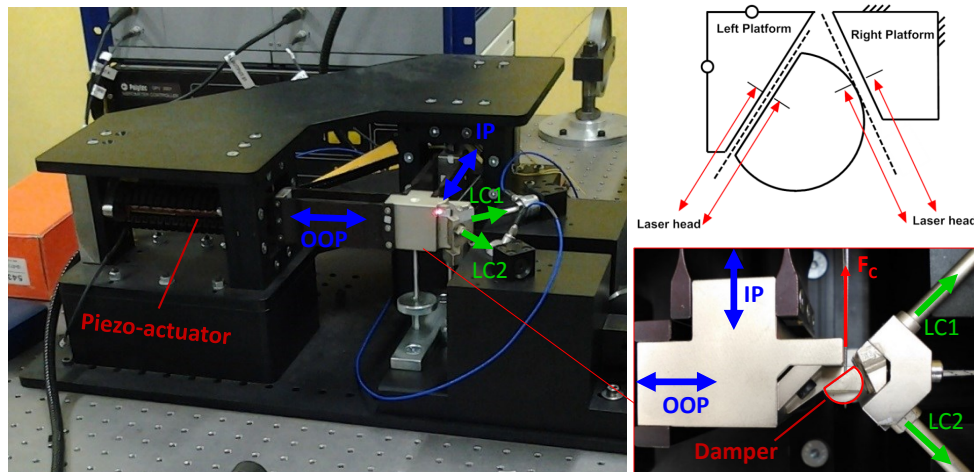


Fig. 2.1 Damper-Only test rig with semi-cylindrical damper installed on the rig. Left platform is connected with the piezo electric actuator while the right platform connected with the sub-assembly of two load cells measuring contact forces [1]

### 2.1.2 Basic test rig design criteria

While starting with the design, following main aspect were considered carefully to fulfill certain requirement.

1. A single blade assembly with two under platform dampers must be tested. Each damper is in contact with the blade platform on one side and with a ground platform on the other side.
2. Contact pads are required to be replaceable part to provide economical benefit to the substitution of the complete ground platform. Moreover, the platforms can be manufactured with different material and contact angles to investigate several dampers behavior with different geometries according to their respective blade.
3. The test rig should have a capability to test different turbine blades with minor adjustment of the apparatus, provided the maximum blade size not exceeded.
4. The test rig should allow to measure the damper contact forces on the ground platforms.
5. To clamp the blade a regulated and measurable clamping force is required. This clamping force should simulates the effect of the real centrifugal load experienced by the blade while turbine runs.
6. The test rig should allow to measure relative displacement between the damper-blade contact surfaces.

## 2.2 Design of the test rig

This newly designed test rig is a static test rig in which the blade and other parts are not rotating. However, different design mechanisms and strategies are adapted as much as possible to replicated the actual working conditions experienced by the damper and blade. The test rig is composed of following main features:

- blade clamp mechanism

- contact Force Measurement system
- application of the static load on the dampers to simulate centrifugal force effect
- excitation of the blade

### 2.2.1 Clamping of the blade on the test rig

The design of test rig was started with the clamp design whose purpose is to rigidly clamp the blade with a giving clamping force. To better understand the overall architect of the rig, a detailed drawing of the test rig is presented in Fig. 2.2. The rig is consist of three sub-assemblies, namely a central block and two lateral blocks. These three sub-assemblies are fixed on the main table through a base plate (2) with several vertical bolts. The central block has two symmetric parts called (1A) and (1B). A wedge block clamp mechanism is housed by these two symmetric blocks as shown in section C of the Fig. 2.2. A more clear and separate view of the clamp is shown in Fig. 2.3. It can be seen that a vertical pushing force denoted by  $F_P$  is applied at the bottom of the blade root. This force  $F_P$  simulates the actual centrifugal force experienced by the blade during working of the turbine and clamps the blade firmly on the test rig. In actual working conditions instead of pushing, the blades undergo pulling force which may result in increase in the blade frequency due to additional stiffening. This effect can be achieved on a rotating test rig as mentioned in Chap. 1 Sec. 1.2.2. in our case the architect of the test rig is stationary and a pushing force clamp mechanism was considered to simulate more realistic conditions compared to any ordinary blade clamps which normally fix the blade by closing the jaws from the sides.

#### Clamp wedge blocks

Two wedge blocks namely the lower wedge (3) and the upper wedge (4) are placed on each other inside the central blocks housing (1A) and (1B). The objective of these wedges is to convert and transmit an applied force  $F_B$  perpendicular to the blade longitudinal axis along the side of the lower wedge (3) into a pushing force  $F_P$  along longitudinal axis of the blade. The applied force  $F_B$  is acquired by fastening the main Bolt (5) with help of a wrench. Due to the given slope of 1:10 between the

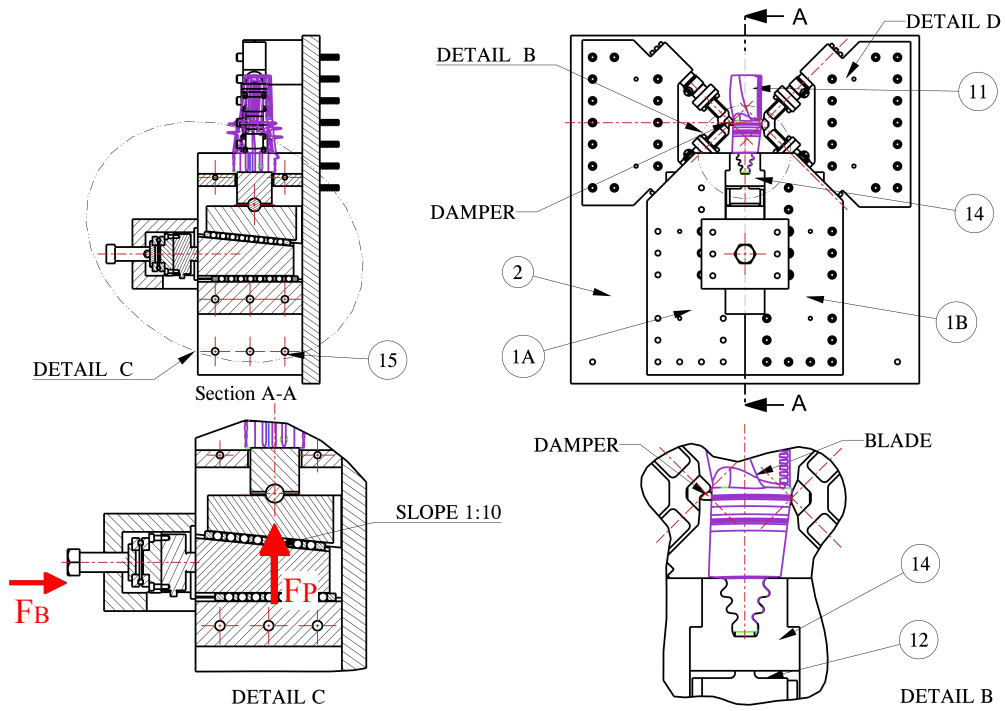


Fig. 2.2 A top and section views of the test rig to present its details

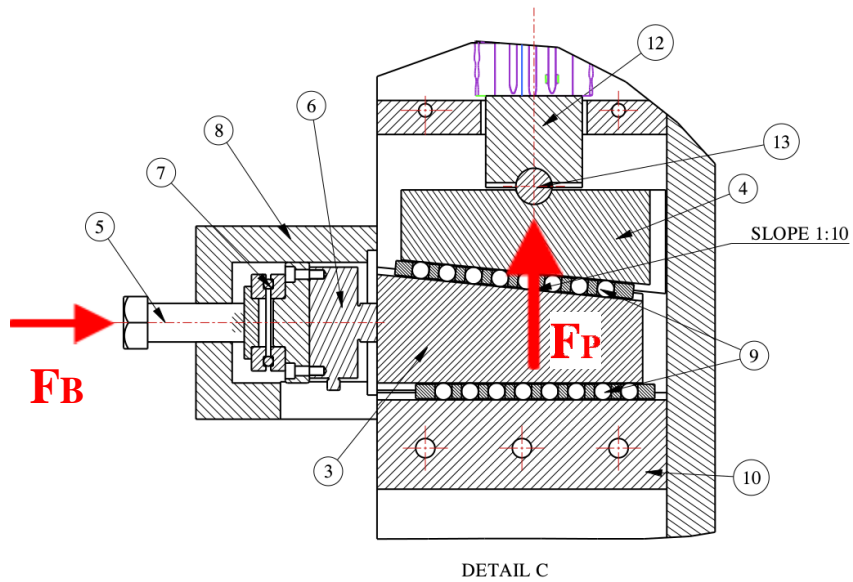


Fig. 2.3 An enlarged section-view of the clamp mechanism showing arrangement of the wedge blocks and inner parts of the assembly

two wedges the nominal force amplification factor  $A_n$  between the bolt force  $F_B$  and pushing force  $F_P$  is 10. Between the lower wedge block (3) and main bolt (5) a strain gage based load cell (6) is placed to measure the manually applied bolt force  $F_B$ . Furthermore, a thrust ball bearing (7) is placed between the main bolt and clamp load cell (6) to allow a relative rotation between these two components. A square casing (8) of steel is used to house this complete sub-assembly consist of the main bolt, thrust ball bearing and strain gage based clamp load cell. The casing is fixed on the top of the central block with six screws.

### Blade Clamp efficiency

To minimize the frictional losses, two rails of linear flat roller bearings (9) are placed between the sliding surfaces of the clamp. An adequate surface treatment of corresponding wedge surfaces is performed according to manufacturer guidelines as given in [103] to avoid any penetration of the bearing rollers. First flat bearing rail is inserted between the lower wedge (3) and the bottom fixed block (10). Whereas, a second bearing rail is placed between the inclined surfaces of lower and upper wedge to convert the sliding motion of the lower wedge into rolling motion. Certainly, a complete elimination of all the losses caused by the friction in the clamp mechanism are inevitable and a minute loss in clamping force is resulted from the rolling friction. Therefore, the actual applied pushing force at the blade root  $F_P$  and amplification factor  $A_{act}$  varies slightly from the theoretical values. These actual values of the force  $F_P$  and amplification factor  $A_{act}$  can be calculated with the following formulas

$$F_{P,act} = \frac{\cos\alpha - 2\mu \sin\alpha - \mu^2 \cos\alpha}{\sin\alpha + 2\mu \cos\alpha - \mu^2 \sin\alpha} F_B, \quad (2.1)$$

$$A_{act} = \frac{F_{P,act}}{F_{B,act}}, \quad (2.2)$$

whereas  $\alpha$  and  $\mu$  are the slope of the wedge blocks and rolling friction coefficient of the linear flat roller bearings respectively. The complete derivation of these equations can be found in Appendix A Sec. A.2.

Using above given equations, the efficiency of the clamp  $\eta_c = A_{act}/A_n$  is defined by a ratio between the actual and nominal amplification factor. Considering the range

of friction coefficient of the linear flat roller bearings between  $\mu = 0.001 \div 0.0015$ , as reported in the manufacturer manual [103], the overall efficiency  $\eta_c$  of the clamp ranges between  $\eta_c \approx 0.97 \div 0.98$ . The pushing force  $F_P$  is exerted on the blade (11) with the help of a pushing block (12). A cylindrical pin named as self-aligning pin (13) is placed between the upper wedge block and pushing block. This pin allows a small rotation between these two parts to apply a uniform pressure at the blade root even if small misalignment between the blade and upper wedge is occurred. To abstain the immense contact pressure resulted from the large clamping force, this self-aligning pin and its counterparts were designed by considering their contact surfaces as conforming contact surfaces. Contact pressure distribution as a function of the diameter of conforming surfaces, was determined from the graphs and tables given in [104]. The turbine blade is placed in the blade adapter (14) which has machined groove exactly similar to the turbine bucket's groove to match the geometry of the blade root as shown in Fig.2.4 The blade adapter abstain clamping force against its shoulders on the central block. Thus the pushing force  $F_P$  is restrained by contact with the slot machined in the blade adapter according to the geometry of the blade root. This blade adapter is a replaceable part of the clamp. Therefore, several blades can be clamped and tested on the rig by simply replacing the old adapter with a new blade adapter corresponding to the given blade root geometry. To finally fix the

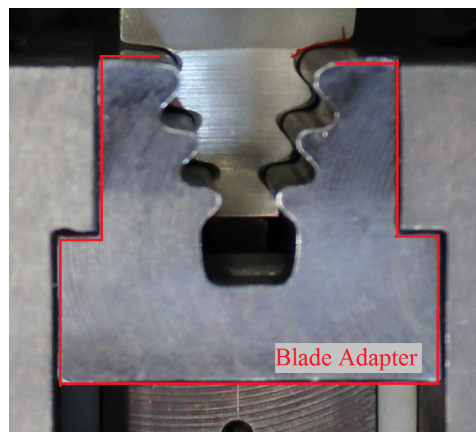


Fig. 2.4 Design of the blade adapter with a fir-tree dove tail groove to fix a blade on the rig

sub-assemblies of central block with each other, eight long stud bolts were inserted through holes (15) across them. In addition to the vertical bolts, these stud bolts further increase the stiffness of structure.

## 2.2.2 Contact Force Measurement system

An important feature of the rig is to measure the dynamic and static forces acting on the damper contacts. For each damper on the corresponding side of the blade, an individual contact force measurement system has been designed as shown in Fig. 2.7 and Fig.2.8. Whereas, in these figures  $N$  and  $T$  are the normal and tangential force components of the contact force, respectively. Each damper is placed between the two contact platforms which are formed by the contact force measuring block and blade on both sides as shown in Fig. 2.5. Each force measuring system includes four main parts, an L-shaped structure called L-separator (17) with two limbs (16A and 16B), two load cells ( $LC_{ij}$ ) and a very rigid lateral block (18) which is fixed on the main table. These load cells  $LC_{ij}$ , are fixed at the end of two limbs of the L-Separator with the help of two connecting blocks (19A and 19B) and measure the respective force components acting along the limb  $R_{ij}$ . Subscript 'E' and 'O' refers to the even and odd side of the blade respectively, where even and odd were named corresponding to the serial number of the load cells. The two limbs are orthogonal to each other and each limb of L-sep contains two thin parallel strips as shown in Fig.2.7. The axes of the two limbs of a L-sep intersect each other at local point that corresponds to nominal contact between the damper and replaceable pad. A complete design criteria and working of this L-separator is explained in section 2.2.3. The Load cells are assembled precisely along the axes of the limbs and their coaxiality was ensured by the centering rings. These load cells are fixed to the lateral block (18) with help of screws from the back side of the block. Two aligning-pin holes (20A and 20B) on the lateral block (18) define a proper location of the force measurement system with respect to the nominal damper position and ensure its precise assembly. The importance of these locating holes is described in Sec. 2.2.6.

## 2.2.3 Design of the L-Separator

The main objective of the L-Separator is to divide the damper contact force into two orthogonal components acting along its limb axes. Each load cell placed at the end of corresponding L-Sep limb, experiences only the axial force component with the proposed shape and geometry. The component of the force along transverse direction

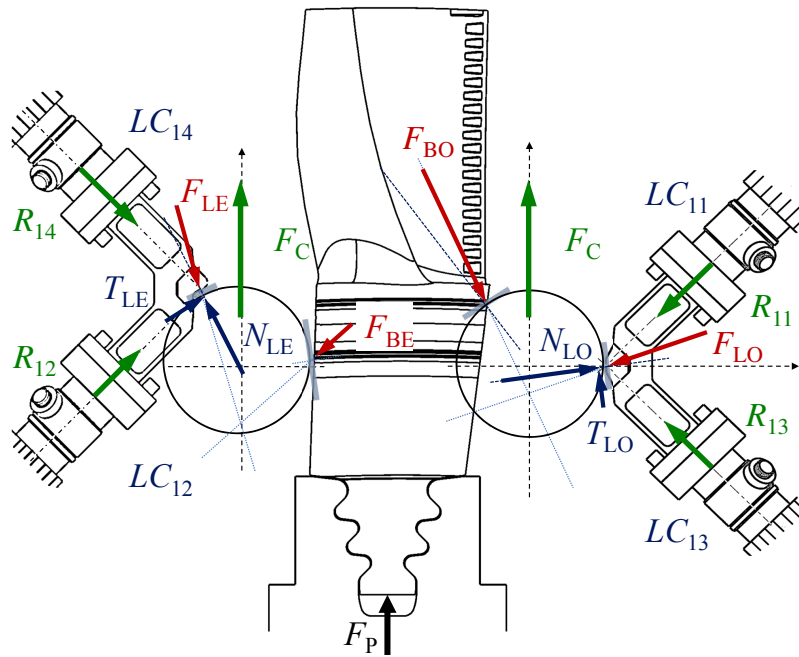


Fig. 2.5 Assembly of two dampers on a single blade at their nominal positions and contact forces representation at damper static equilibrium condition.

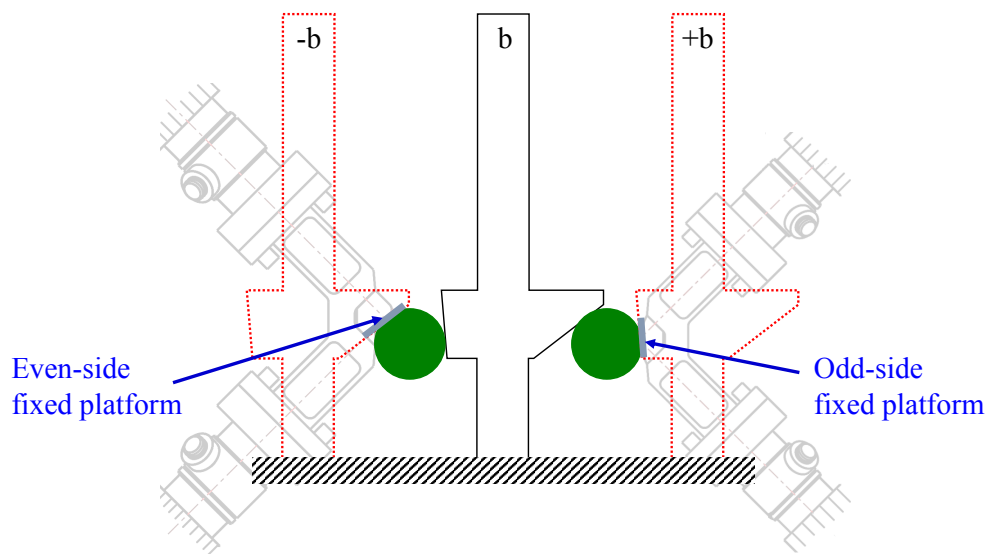


Fig. 2.6 Architect of the test rig to replicate the configuration of damper-blade contact setup of an actual turbine

of the limb is neglected by the load cells and the effect of the cross-talk between two load cells has been prevented. This objective was acquired by designing each arm of



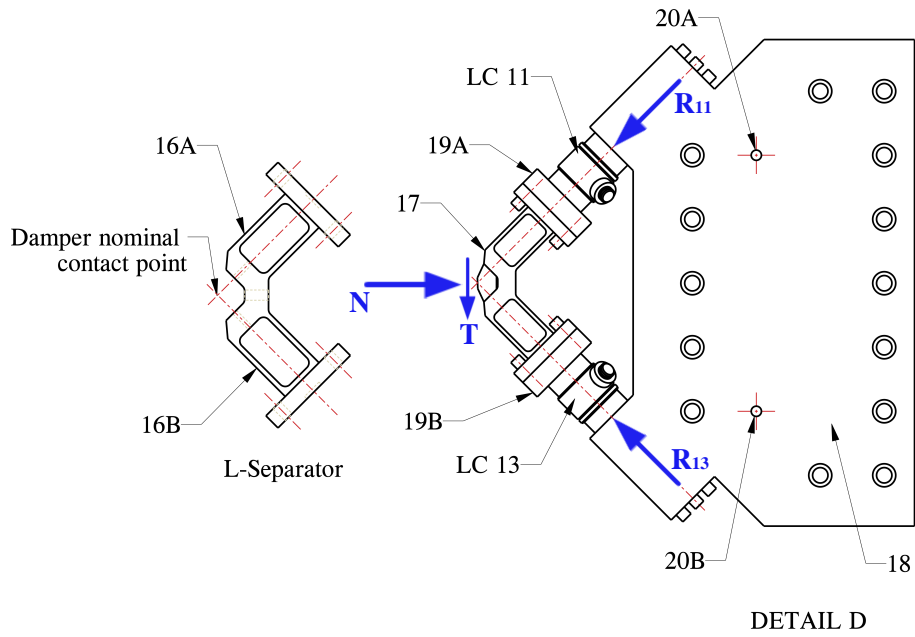


Fig. 2.7 A complete sub-assembly of odd side contact forces measuring system and nominal contact point on L-separator

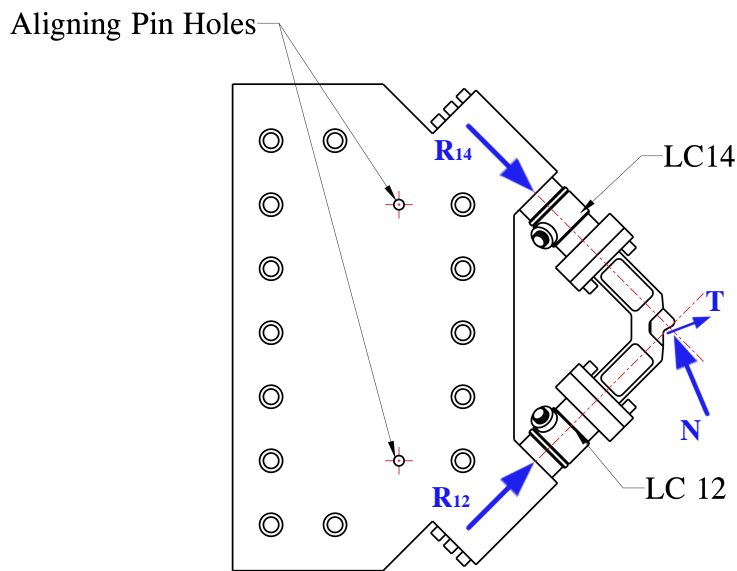


Fig. 2.8 Even side contact forces measuring system

the L-Separator with a substantially high longitudinal and transverse stiffness ratio  $k_l/k_t$ . In fact, as shown in Fig. 2.9, if a force is applied on one limb of the L-Sep along its axial direction, the ratio of reaction forces experienced by the load cells will be the same as the stiffnesses,

$$\frac{R_{Y1}}{R_{Y2}} = \frac{k_l}{k_t}. \quad (2.3)$$

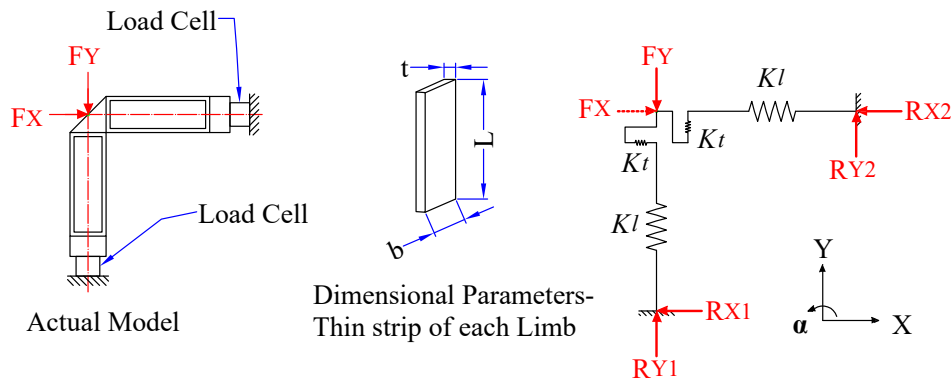


Fig. 2.9 Basic model and dimensional details of the L-Separator

### 2.2.4 Modeling of the L-separator

In the preliminary design, the L-separator has been modeled by the simple beams and lumped mass elements. In this regard, a matrix structural model of this L-separator using beam elements with fixed supports has been considered to estimate the effectiveness of L-separator in terms of decoupling the two components of the force. A term called *degree of separation* is defined as a ratio between the reaction force experienced by the load cell and applied normal force along the axis of respective limb of the L-separator,  $R/F$ . The goal of the initial design was set to compute the *degree of separation* offered by the L-separator. A graph as shown in Fig. 2.10 is plotted between the *degree of separation* and L-separator geometrical parameters. In this graph the variation in *degree of separation* w.r.t the L-separator aspect ratio  $L/b$  with different strip thicknesses  $t$  is presented, whereas  $b$  and  $L$  are

the breadth and length of the limb strip respectively. It can be seen that at the design point  $L/b = 1$  and  $t = 1.5$  mm, L-separator is capable to separate up to 99.4 % of the applied force. These results were further confirmed from the full finite element analysis of the L-separator as show in Fig. 2.11. In the full FE analysis of the L-separator, effect of the load cell stiffnesses were also included. Moreover, this uncertainty is considered to correct the measured load cell signals and actual contact forces are estimated during post processing of the experimental data .

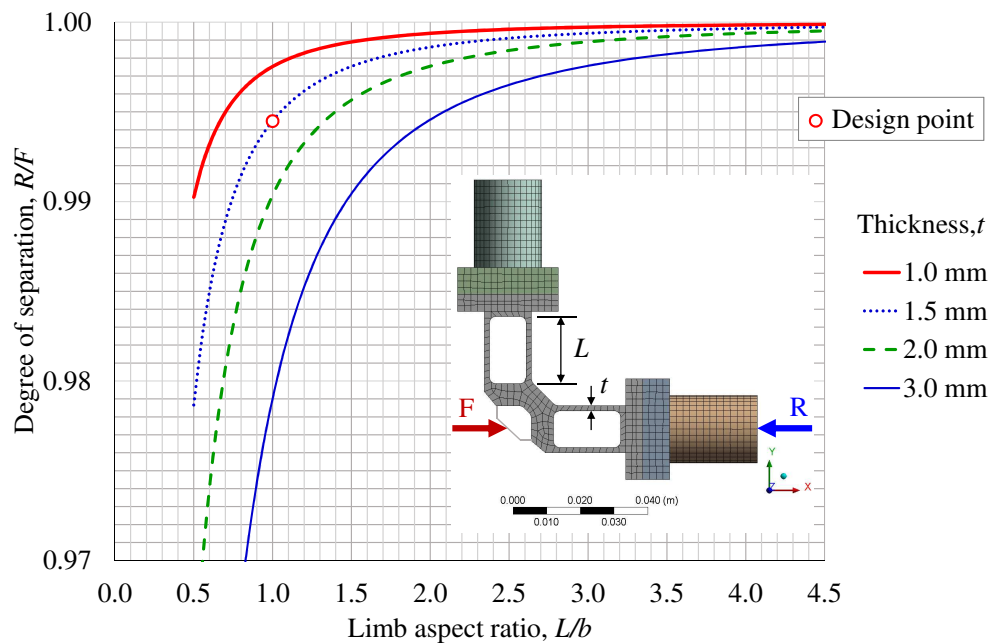


Fig. 2.10 defining the design point for L-Separator by plotting degree of separation of the forces with respect to its dimensional parameters.

### 2.2.5 Calculation of contact forces

The feature that more distinguishes the test rig used in this research from other experimental setups is the direct measurement of the contact forces when the damper is dynamically coupled with the blade. Contact forces  $N$  and  $T$  between the dampers and blade are computed through a static force equilibrium of the damper while neglecting its inertia. In Fig. 2.12 and 2.13, the static force equilibrium of both side dampers i.e. "odd" and "even" side respectively, is presented. Load cells  $LC_{12}$  and  $LC_{14}$  defines the even side of the test rig whereas Load cells  $LC_{11}$  and  $LC_{13}$  defines

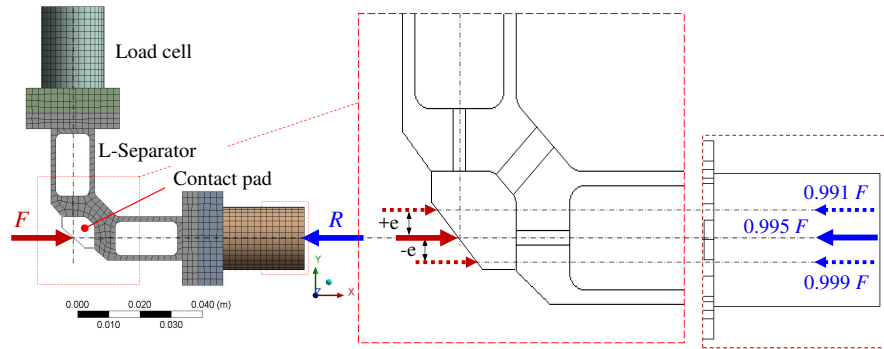
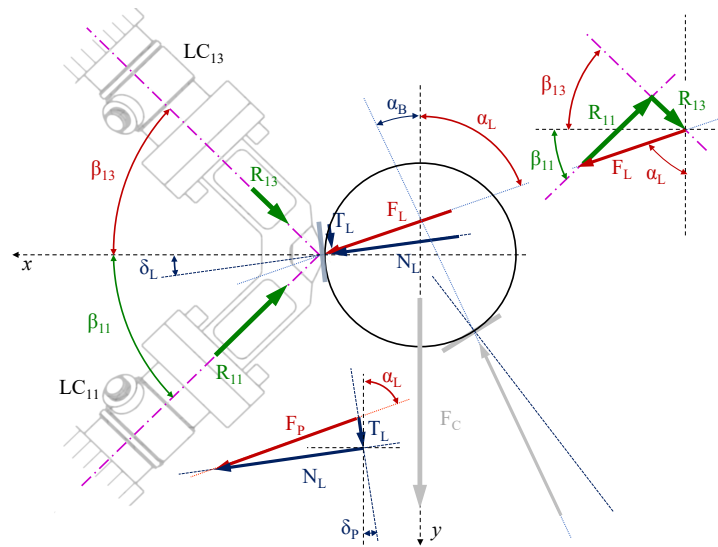
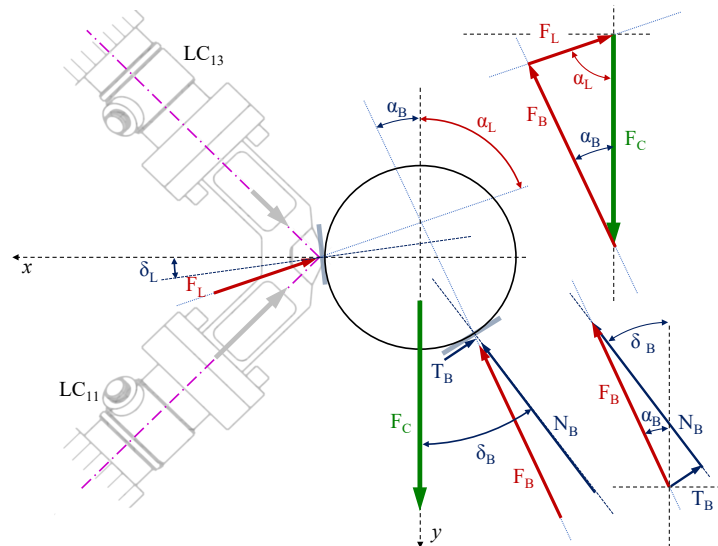


Fig. 2.11 FE model of L-Separator with load cell assembly. Eccentricity  $e$  depicts the misalignment error of contact forces due to limitation in manufacturing accuracy.

odd side. In these figures, the assembly of the L-separator along with load cells on one side of the damper contact is shown. Whereas, the contact of the damper on blade side is only shown by a solid line and the dampers are re-scaled and enlarged to show the actual contact of the damper with platforms and the forces acting along these contacts. It can be noticed that in this architect of the test rig, the platform corresponds to both fixed support/L-separator actually replicate the contact of the consecutive blade of the bladed-disk as shown in Fig. 2.6. In this Fig. 2.6, the central blade " $b$ " represents the actual blade assembled on the rig while " $-b$ " and " $-b$ " are the virtual blades replaced with corresponding platform of the fixed support. The both load cells of corresponding side of the blade directly measure the normal  $N_L$  and tangential  $T_L$  force components acting along the contact of the damper and L-separators. From these measured forces, the normal and tangential force component along the damper and blade contact  $N_B$  and  $T_B$ , are computed. The final formulation of these contact force components, obtained by applying the damper static force equilibrium, is summarized in Table 2.1; the symbols and abbreviations are the same as given in the Figs. 2.12 and 2.13. Moreover, the complete derivation of all the force components, according to the above mentioned procedure, is given in Appendix A Sect. A.3;



(a) Forces on the L-Separator; odd load cells LC11/LC13

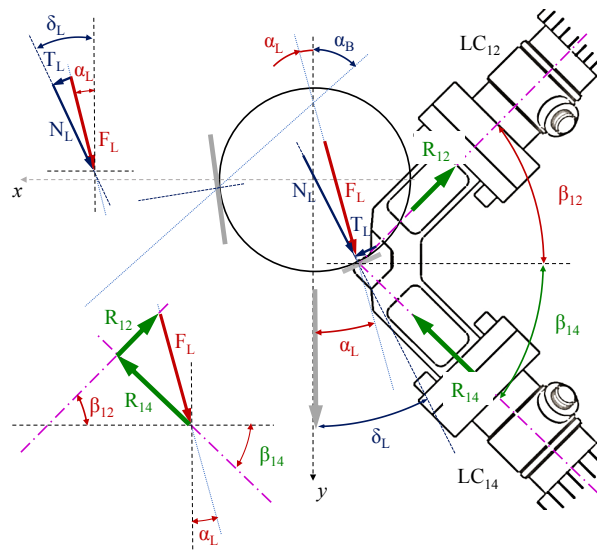


(b) Forces on the damper, odd load cells LC11/LC13

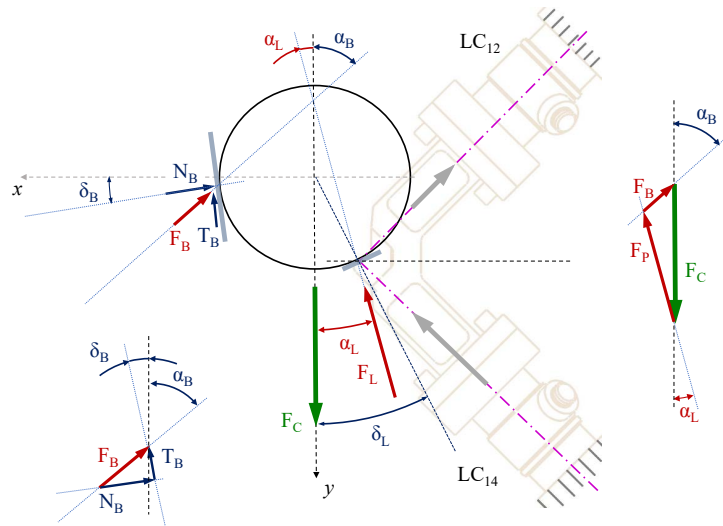
Fig. 2.12 Details of contact forces on the load cells LC11/LC13 odd side. Positive forces and angles are shown

## 2.2.6 Contact force measurement accuracy

The quality of a measuring systems in terms of providing the accurate results is its most essential characteristic. However, there are always few internal uncertainties of a measuring system which are unavoidable e.g. mechanical error or electronic



(a) Forces on the L-Separator; even load cells LC12/LC14



(b) Forces on the damper, even load cells LC12/LC14

Fig. 2.13 Details of contact forces on the load cells LC12/LC14 even side. Positive forces and angles are shown

signal losses etc. In the case of contact force measurement system, the accuracy of contact forces determined from the measured load cells signals, depends upon several factors. The principal sources of uncertainties are as follows:

Table 2.1 derived contact force components on the blade and L-Separator contacts for both even and odd side.

Odd side	Even side
<u>On the L-Separator</u>	
$F_L = \sqrt{R_{11}^2 + R_{13}^2}$	$F_L = \sqrt{R_{12}^2 + R_{14}^2}$
$\sin \alpha_L = \frac{R_{11} \cos \beta_{11} + R_{13} \cos \beta_{13}}{F_L}$	$\sin \alpha_L = \frac{R_{12} \cos \beta_{12} - R_{14} \cos \beta_{14}}{F_L}$
$\cos \alpha_L = \frac{R_{11} \sin \beta_{11} - R_{13} \sin \beta_{13}}{F_L}$	$\cos \alpha_L = \frac{R_{12} \sin \beta_{12} + R_{14} \sin \beta_{14}}{F_L}$
$N_L = F_L \cdot \cos(\pi/2 - \alpha_L - \delta_{Le})$	$N_L = F_L \cdot \cos(\delta_L - \alpha_L)$
$T_L = F_L \cdot \sin(\pi/2 - \alpha_L - \delta_L)$	$T_L = F_L \cdot \sin(\delta_L - \alpha_L)$
<u>On the Blade</u>	
$F_B = \sqrt{F_C^2 + F_L^2 - 2F_C F_L \cos \alpha_L}$	$F_B = \sqrt{F_C^2 + F_L^2 - 2F_C F_L \cos \alpha_L}$
$\sin \alpha_B = \sin \alpha_L \frac{F_L}{F_B}$	$\sin \alpha_B = \sin \alpha_L \frac{F_L}{F_B}$
$\cos \alpha_B = \frac{F_C - F_L \cos \alpha_L}{F_B}$	$\cos \alpha_B = \frac{F_C - F_L \cos \alpha_L}{F_B}$
$N_B = F_B \cdot \cos(\delta_B - \alpha_B)$	$N_B = F_B \cdot \cos(\pi/2 - \alpha_B - \delta_B)$
$T_B = F_B \cdot \sin(\delta_B - \alpha_B)$	$T_B = F_B \cdot \sin(\pi/2 - \alpha_B - \delta_B)$

1. the uncertainty introduced by the data acquisition system and its counter parts, which include load cells, wiring, charge amplifiers and acquisition cards,
2. the overall manufacturing uncertainties due to geometrical and dimensional tolerances of the mechanical components and
3. the error involved in the computation of contact forces. This error results from the uncertainty in the measured relative angles between the static force applied on the dampers to simulate centrifugal force and normal of the contact surfaces.

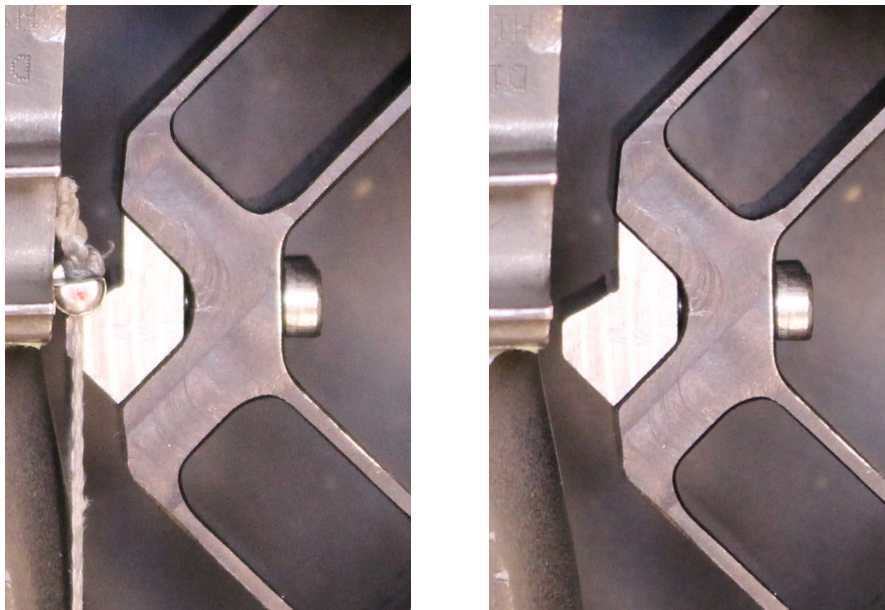
All force measuring load cells have a sensitivity of  $-9.6 \text{ pC/N}$ . This sensitivity together with the resolution of the charge amplifier  $\pm 0.1 \text{ pC}$  provides a threshold of the measurable force of  $\pm 10.4 \text{ mN}$ . The error introduced by the charge amplifier is  $< \pm 1\%$  of the full scale as provided by the manufacturer in the user manual [105]. In the all experimental activities carried during this research, a full scale of  $200 \text{ N}$  was used. Data acquisition system attached to the test rig is consist of 8 channel analog inputs card (simultaneous sampling at  $1.25 \text{ MS/s/ch}$ , 16-bit resolution). The accuracy of the card, in the voltage range  $\pm 10\text{V}$ , is  $3 \text{ mV}$  thus giving an accuracy  $\pm 0.06\text{N}$  on the measured forces corresponding to  $< \pm 0.04\%$  of the full scale. Consequently, an approximated overall uncertainty resulted from the electronics instrumentation is  $< \pm 1.05\%$ .

The nominal position of the dampers assembled on the test rig is another important factor of this force measurement system that can introduce a potential error in the measurements. As each damper is in contact with two platform i.e. on one side with with the blade platform and on the other side with the L-Separator platform. Therefore, the relative position of these both contacts is very important and must be ensured at the correct location during test rig assembly. To minimize this uncertainty, the central block of the blade clamp and two lateral blocks of the force measurement system were placed on the base plate with location pins. But due the mechanical tolerances involved in the manufacturing of different test rig parts, a small mis-location in the actual contact point on the L-Separator with respect to the nominal contact point is inevitable. Whereas, the actual nominal contact point exit at the point of intersection of two load cell axis of the corresponding L-separator. An eccentricity  $e$  was introduced to define this mis-location as shown in Fig. 2.11. A maximum value of  $e = \pm 1.5 \text{ mm}$  was estimated from the overall mechanical tolerances chain. Furthermore, the numerical analysis of the fully finite element model of the force measurement system were performed to estimate this error. In this regard, the reaction force on the load cell was calculated for the case when applied force was applied at the nominal point of the contact and at the point of maximum eccentricity  $e$ . It has been found that this mis-location results in a discrepancy of  $\pm 0.4\%$  in the load cell reaction corresponding to its nominal value. In this force measurement system, the forces directly measured by the load cells are corresponding to the contact that exist between the damper and L-separator. Whereas, the normal and tangential force components correspond to the other contact i.e. between the damper-blade, were



computed by considering the static force-equilibrium of the damper as explained in Sec. 2.2.5.

It can be observed from all the equations given in Table 2.1 that accuracy of force computation highly rely on the all the angles of the different contact surfaces with respect to applied static force on the damper with the help of wires. A small deflection in angle of the applied static force on dampers with respect to contact surfaces, results in a significant variation in measured reaction forces by the load cells. Therefore, it is very important to know the actual angles of all contact surfaces with respect to applied force static force. The actual contact angles of the dampers can be obtained only while all parts of the test rig are assembled at their final positions. For this reason, a high-resolution images were taken exactly from the top of the test rig, after full assembly of all parts before starting an experiment, with and without the dampers placed at their nominal positions. The location of the camera on the top of the blade exactly in the middle of the corresponding image is important to avoid the parallax uncertainty in these measurements. A parallax error is the perceived shift in an object's position as it is viewed from the different angles. When we have to take reading from an instrument (analog) or do some measurements then different viewing position will give different readings leading to an error. Basically, it is the displacement of an object from two different lines of sight and many optics systems have software built in to compensate for such things. Example of such images is shown in Fig.2.14. Post processing of these images was carried out in *NI Vision Builder 2014* and an accuracy of  $\pm 1^\circ$  on the measured angles in this technique was approximated. Moreover, the error in the corresponding calculated force components depends on the considered damper-blade geometry. The sensitivity of the contact forces, for a real turbine blade and damper used in this research activity, is summarized in the Table 2.2. The force sensitivity, namely force per unit angle, has been estimated by the variation in contact force  $N$  and  $T$  due to varying the measured angles  $\delta_{L,B}$  and  $\beta_{In}$  ( $n = 1, \dots, 4$ ) up to ( $1^\circ$ ). It can be observed that the error on tangential force of the even side  $T_L$  corresponding to the contact of L-Sep is significantly higher than others. The higher error on this particular contact is because of the contact geometry of the real blade and corresponding damper. This higher error on a particular contact mainly depends upon the geometry and angles of the contact interface. Moreover, in **Chap.7** it will be explained in details that this error can obstruct to match the numerically computed blade response with experimentally



(a) High resolution image of the finally as-sembled blade on the rig without any damper. (b) High resolution image of the finally as-sembled blade on the rig with cylindrical damper

Fig. 2.14 Images taken on the rig to measure directly the contact and other geometrical angles by post processing with "NI image builder" software.

measured FRFs and therefore, a modified test rig configuration will be proposed to overcome this problem.

### Drift Compensation

Among the other uncertainties, the contact force measurement involves an additional error subjected to the experiment duration called *drift error*. This error is due to the discharge in the capacitance of load cell amplifiers with time. To minimize and compensate this error, the following procedure was adapted for all the contact forces measurements through out this thesis:

1. each load cell reference was reset to zero before placing the dampers at their nominal positions and loading.
2. Dampers were loaded at the required static force and start time of the experiment was recorded.

Table 2.2 Sensitivity of contact forces to the specific damper/blade geometry

Sensitivity, in N/°	Odd side, $i = 1, j = 3$				Even side, $i = 2, j = 4$			
	$N_L$	$T_L$	$N_B$	$T_B$	$N_L$	$T_L$	$N_B$	$T_B$
$\frac{\partial}{\partial \delta_L}$	-0.6	1.1	0.0	0.0	-0.3	1.6	0.0	0.0
$\frac{\partial}{\partial \delta_B}$	0.0	0.0	-0.7	1.4	0.0	0.0	0.8	1.1
$\frac{\partial}{\partial \beta_{1i}}$	0.0	-0.1	-0.1	0.0	0.0	0.0	0.0	0.0
$\frac{\partial}{\partial \beta_{1j}}$	0.6	1.0	-0.8	-1.0	-0.3	-1.6	1.3	1.9
Accuracy, in N/°	1.2	2.2	1.6	2.4	0.6	3.2	2.1	3.0

3. Static and dynamic components of the contact forces were recorded during the experiment.
4. At the end of the experiment, dampers were unloaded and removed from the test rig. End time of the experiment as well as contact forces were recorded again. If a non-zero force value was present it was due to the time drift.
5. These non-zero values were then used for drift compensation on the measured contact forces by assuming a linear progression of the drift with time.

It was found through this drift compensation procedure that the loss in signal was not higher than 2-3 mN/s. Thus, the error on forces is negligible for a typical measurement remaining for a 5 minutes. However, still this drift compensation procedure was performed to obtain most possible correct results for all the measured contact forces during this thesis.

### 2.3 Electronic Instrumentation connected to the rig

As explained in the Sec. 2.2 that a number of electronic instruments are connected on this test bench to measure the damper-blade dynamics and kinematics. A list of those all measuring instruments and their data sheets are given in the Appendix A Sect. A.1 to underline the information about their sensitivity and measuring range.

## 2.4 Final assembly and overall characteristics of the test rig

After going through all above mentioned design procedures and calculations, all manufactured parts of the rig were assembled on an optical table carefully. The top view of the finally assembled test rig is shown in Fig. 2.15. The overall characteristics of the test rig are summarized in the Appendix A Sec. A.5.

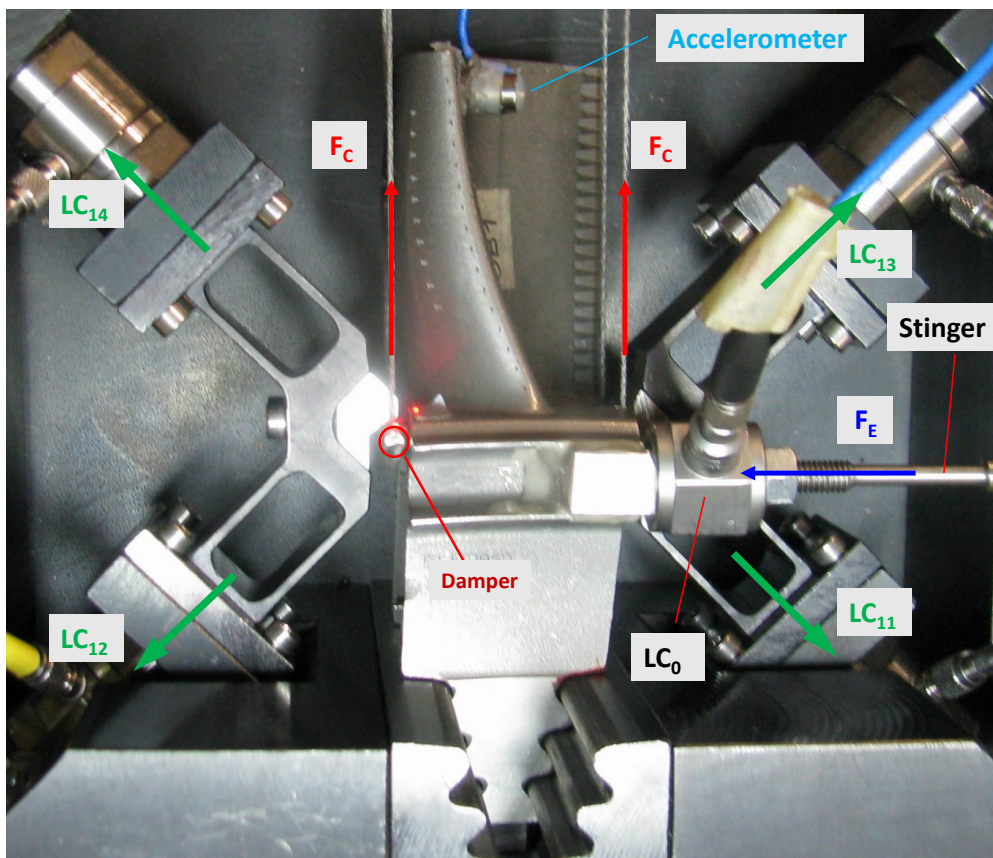


Fig. 2.15 Top view of finally assembled test rig with a real turbine blade and dampers

## 2.5 Experimental setup

In this test rig two different experimental frameworks/layouts, to measure the blade dynamics and damper contact parameters, are configured with two data acquisition

systems (DAS-I) and (DAS-II) as shown in Fig. 2.17 and 2.18 respectively. In the first configuration, blade amplitude response as a function of blade excitation frequency is measured and this data acquisition system (DAS-I) works in frequency domain. In this layout, the blade is excited at required amplitude with a stepped-sine excitation force signal for a given range of excitation frequency. A closed loop feedback controlled system in DAS-I ensures to control the excitation force level with the help of load cell ( $LC_0$ ) (see Fig. 2.17) within the defined tolerances. The response amplitude of the blade is measured with an accelerometer placed on its trailing side. The recorded excitation force from the load cell ( $LC_0$ ) and response (i.e. acceleration) from the accelerometer is received by the data acquisition system (DAS-I) and used to form the frequency response function of the blade.

As data acquisition system (DAS-I) works in the frequency domain, it is not possible to measure the contact forces acting on the dampers for a given instant of time accurately with this configuration. Therefore, a second layout of the data acquisition system (DAS-II) was configured as shown in Fig. 2.18. In this second framework, the blade is excited by excitation force of a single frequency at a given amplitude. Excitation force level is controlled with the help of load cell ( $LC_0$ ). With this data acquisition system (DAS-II) it is possible to measure the damper-blade relative displacement using differential laser and damper contact forces with four load cells  $LC_{11}$ ,  $LC_{12}$ ,  $LC_{13}$  and  $LC_{14}$ . On this particular blade it was possible to measure only even side damper-blade relative displacement due to complex blade geometry as shown in Fig. 2.16. A detailed diagram presenting both configuration and data acquisition systems is given in 2.19 to demonstrate the difference between both DAS and emphasize on the additionally measured quantities with the help of this novel test rig.

### 2.5.1 Blade Excitation

In both above mentioned two configurations, the blade was excited by attaching an electromagnetic shaker with the stinger on the blade, close its root, as shown in 2.15. A load cell ( $LC_0$ ) is placed at the end of the stinger to apply a controlled excitation force  $F_E$ .

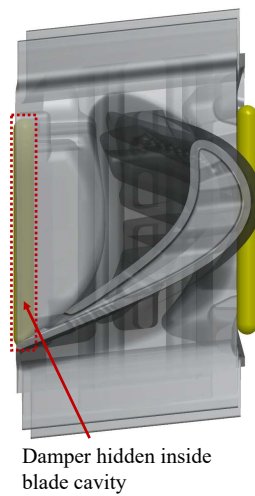


Fig. 2.16 The front view of the blade with two dampers in their nominal position. The damper on the left is hidden inside a cavity

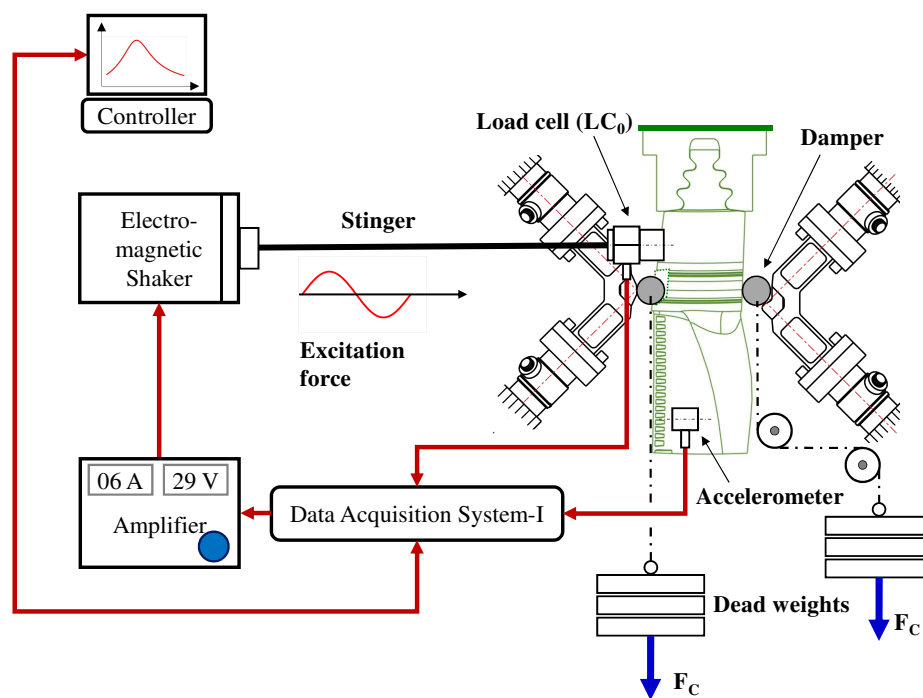


Fig. 2.17 configuration-I with data acquisition-I(DAS-I) to measure the amplitude response of the blade as a function of excitation frequency with and without dampers.

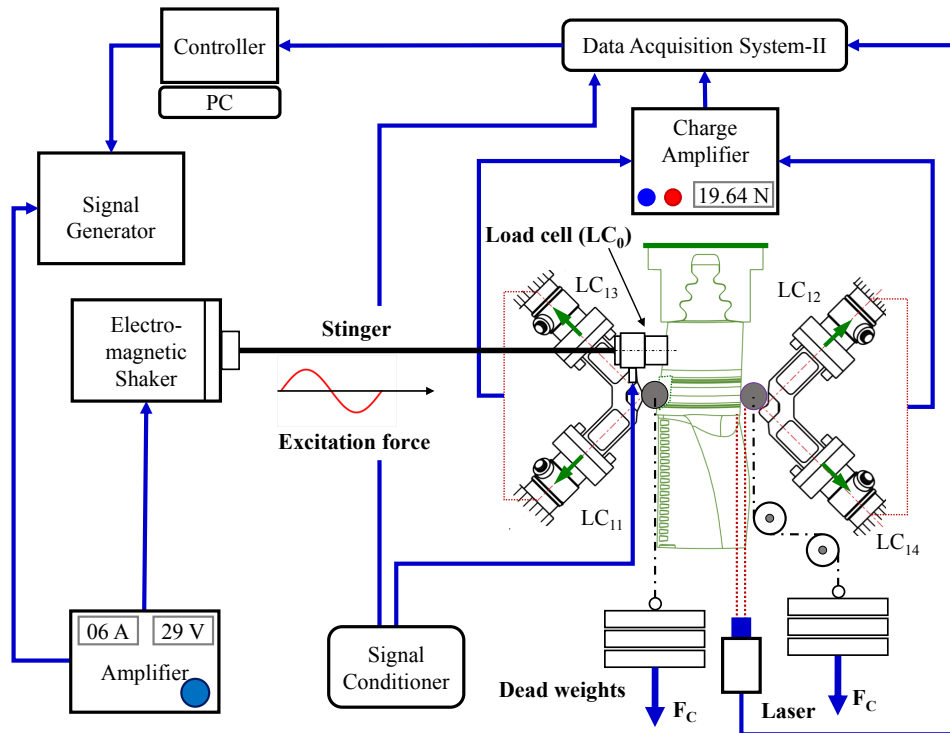


Fig. 2.18 configuration-II with data acquisition-II (DAS-II) to measure the static and dynamic contact force components of the dampers and relative displacement of the contact interfaces.

## 2.6 Conclusion

The novel test rig described in this chapter has been used throughout during this research work to investigate the inner mechanics of the dampers. In addition to the standard measurement of blade frequency response function, the capabilities of the rig e.g. measuring damper contact forces, relative displacement and controlled clamping force etc. facilitate to understand the contact more deeply and help to improve the numerical modeling of the contact interface. Minor changes in the setup of the rig enable it to investigate various dampers and blades on a single test bench. Moreover, several parameters that effect the accuracy of the contact force measuring system were highlighted and solutions have been discussed to minimize the corresponding uncertainties.

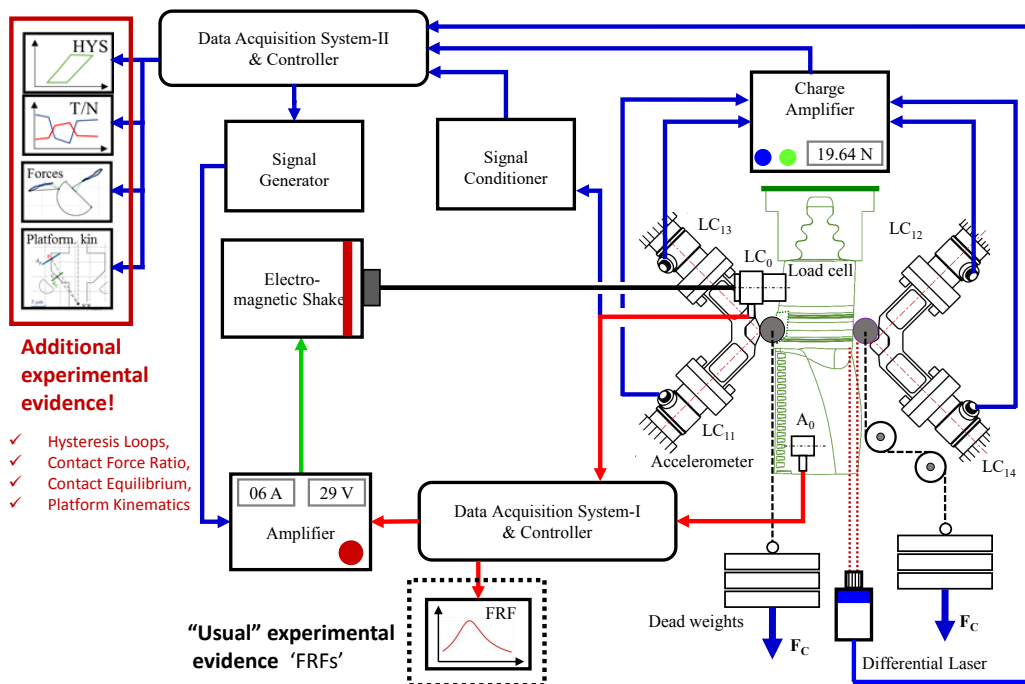


Fig. 2.19 A combined layout of both data acquisition systems to highlight the additional experimental evidences available on this novel test rig, along with the commonly measured FRFs



# Chapter 3

## Design of the Dummy Blade

*“A complex system that works is invariably found to have evolved from a simple system that works”*

- John Gaule

### 3.1 Introduction

In this chapter the designing procedure of a dummy blade has been explained. A dummy blade was designed to broaden the experimental investigation of the dampers contact kinematic which were not possible on a real blade due to its complex geometry and contact angles. In the real turbine blade, one damper was hidden inside the blade cavity as shown in Fig. 2.16 which makes it impossible to measure the relative displacement between the damper and blade contact interface with the help of differential laser vibrometer on that particular side. To add more, the relative displacement between the damper and blade platform on accessible side of the real blade was very limited due to its very high structural stiffness.

Consequently, it was decided to develop a dummy blade, with less stiff material than real blade, that allows to investigate conveniently the contacts of both dampers on newly developed test rig. Moreover, this dummy blade was designed with replaceable blade-platforms which ensure the testing of a number of dampers with different contact angles and geometry by simply changing these blade-platforms.

### 3.1.1 Problem Specification

Several design characteristics of the dummy blade were decided prior to its manufacturing. In order to get a simple and symmetric damper-blade contact geometry, following aspects were considered:

1. Fundamental resonance frequency of the dummy blade was considered as prime specification of its design. As the blade is clamped at its root, its dynamic response resembles to a cantilever beam. Therefore, the first frequency of the blade corresponds to its first bending mode. Furthermore, it was decided to have a dummy blade whose first resonance frequency ranges between the 400 to 450 Hz which is close to the actual frequency experienced by the turbine blade of this size.
2. A blade with fir-tree root is required to design so that it can be clamped on the test rig in the available blade adapter.
3. A standard threaded hole must be provided near the root of the blade to connect the stinger of an electromagnetic shaker to excite it with the required force amplitude and frequency range.
4. In order to test a number of dampers on the same dummy blade with different contact angles, the blade is required to have removable contact pads to form blade platforms on both sides with two dampers.
5. Moreover, the blade must be as simple as possible so that it does not render any complications during test set-up and it should allow to place the differential laser near the damper contact interfaces to measure the relative displacements of respective contact surfaces.

### 3.1.2 Modeling of the blade

Initial the designing of the blade was done in a CAD based software and blade was considered as a straight cantilever beam fixed at one end with fir-tree root. Parametric modeling technique was adapted and modal analysis of the blade were performed to obtain its required first resonance frequency by varying blade dimensional parameters.

It was only possible to alter the two geometrical parameters, length  $L$  (only the variable portion as shown in Fig. 3.1) and thickness  $t$  of the blade because the fixed length and breadth of the blade are defined by the contact force measurement system and blade adapter of the test rig, respectively. As both dampers have a particular position on the test rig with respect to blade and contact force measurement system, therefore length of the blade above the dampers position has been parameterized without modifying the lower portion of the blade. A complete drawing with all the technical details of the dummy blade is given in Appendix C

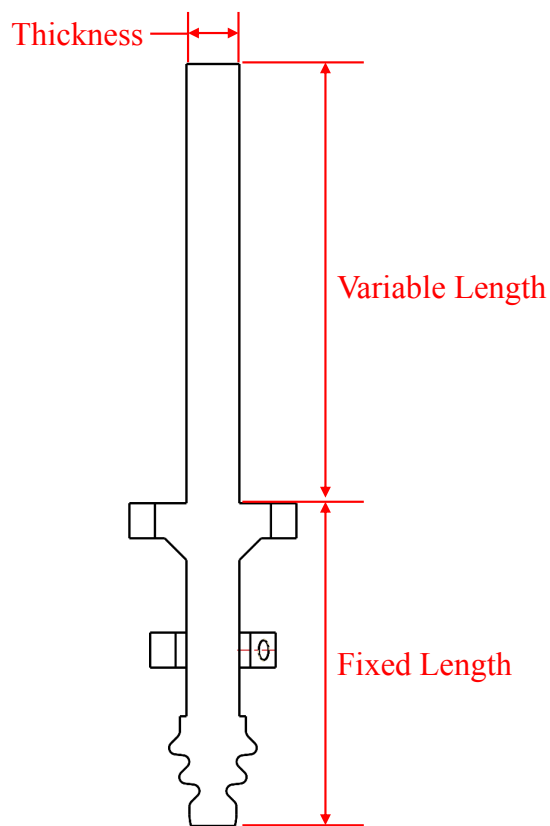


Fig. 3.1 Final sketch of the dummy blade

### 3.1.3 FE Modal Analysis of the blade

After modeling the blade, modal analysis were performed in a finite element analysis software to estimate its fundamental natural frequency. The blade is considered as a cantilever beam clamped at its root. In this first modal analysis, all the nodes

that belongs to the blade root areas facing upward were fully constrained as shown in Fig. 3.2. All these root nodes are constrained because of the fact that when a pushing clamping force on the blade root is applied, from its bottom as explained in **Chap.2** Sec. 2.2.1, only these selected areas come in contact with the blade adapter during assembly of the blade. However, in the final modal analysis (explained in the next chapter) after the blade is developed, the blade numerical model is finally tuned/corrected with the actual blade model by constraining only few randomly selected nodes along these areas.

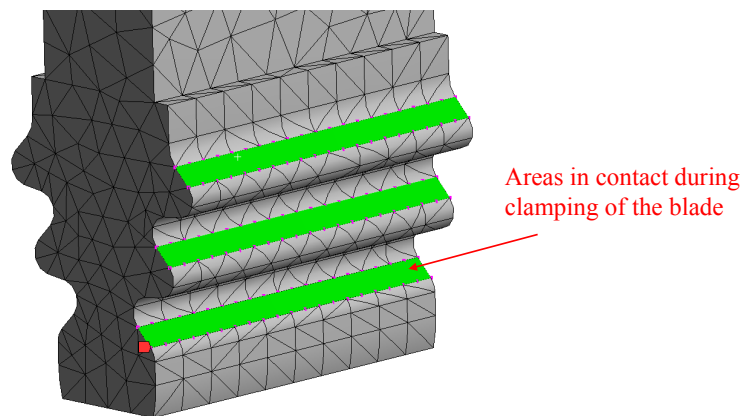


Fig. 3.2 Initial design of the blade with variable and fixed geometry parameters

As it was decided to fabricate the blade with the steel material (less stiffer than the super alloy used for actual turbine blade), the following material properties are assigned to the numerical model during its modal analysis:

- Density,  $\rho$  = 7850 Kg/m<sup>3</sup>
- Poisson's Ratio,  $\nu$  = 0.3
- Young's Modulus,  $E$  = 210 GPA

After going through other tentative steps like element type selection, meshing etc.. in the software, the modal analysis are performed for different lengths and thicknesses of the blade. The length and thickness of the blade are varied in software, with the

help of parametric design optimization tool, to obtain a desired first natural frequency of the blade. The resulted fundamental frequencies of the blade at different blade variable lengths are shown in Fig. 3.3.

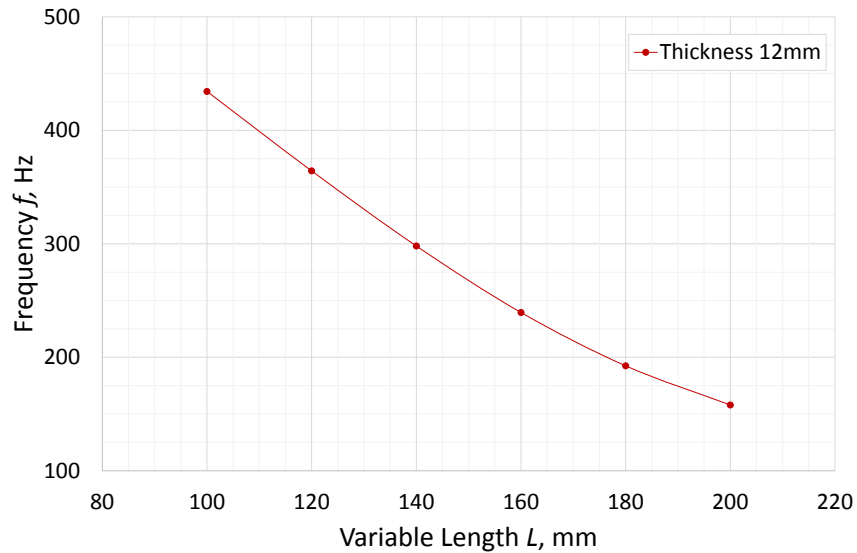


Fig. 3.3 Variation in blade fundamental frequencies w.r.t its variable length at thickness  $t=12\text{mm}$

It can be observed from these results that the first natural frequency of  $\omega_n = 436$  Hz was obtained at the length of the blade  $L=100\text{mm}$ , with a blade thickness  $t=12\text{mm}$  that is within the required frequency range as mentioned in Sec. 3.1.1. Therefore, this length and thickness of the blade are selected for its final design. First 6 natural frequencies of the blade with the selected design parameters are given in Fig. 3.4 with the corresponding mode shapes.

The focus of this thesis is only to explore the behavior of the dampers at the fundamental frequency of blade. Therefore an important thing while designing the dummy blade was to ensure that the first two frequencies and their respective modes of the blade are well separated and decoupled from each other. If we closely observe the first two modes of the blade as shown in Fig.3.5, it can be seen that first mode that corresponds to the frequency 436 Hz is pure bending mode along the thickness of the blade i.e. along Z-axis according to the given coordinate system in the figure.







Sr. No.	Frequency [Hz]	Mode Shape	Sr. No.	Frequency [Hz]	Mode Shape
1	434.3		4	3484.6	
2	892.3		5	4522.3	
3	2340.0		6	6353.5	

Fig. 3.4 First 6 natural frequencies and their corresponding mode shapes of the dummy blade

Whereas the 2<sup>nd</sup> mode of the blade is also second bending mode along its width i.e. along X-axis, at 892 Hz frequency. These modal analysis confirmed that first two modes of the blade are pure bending modes and are well separated from the frequency point of view.

### 3.1.4 Design of removable blade-platform

Two removable blade-platform/pads were also designed as shown in the Fig. 3.7 to fix them on the blade at damper nominal positions with the help of screws. These pads were designed to provide the facility to test several dampers with different contact geometries and contact angles by simply substituting with new contact pads

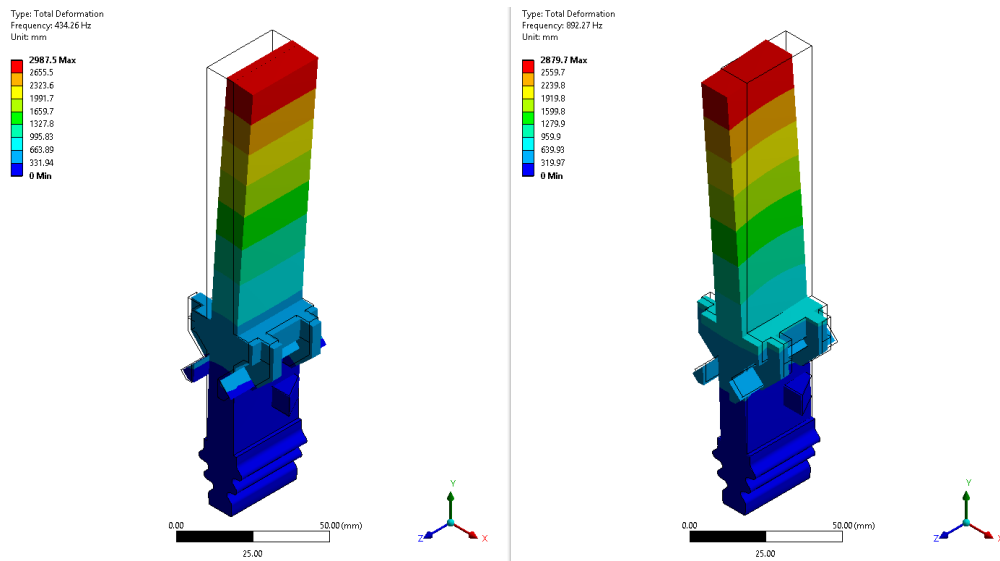


Fig. 3.5 Dummy blade FEM modal analysis, first two mode shapes

without changing the whole blade. To localize the contact on the damper surface and increase the nominal contact pressure, two smooth protrusions were provided on the pads as shown in Fig. 3.6 which ensure a localized contact of the damper along these extruded surfaces. Moreover, to place the differential laser closest to the damper-blade contact along tangential directions, blade and ground platforms are designed with a very small extruded portion above the blade width as shown in Fig. 3.7.

### 3.1.5 Assembly of the dummy blade on the Test Rig

After designing the blade with above mentioned methodology, the blade was manufactured and assembled on the test rig as shown in Fig. 3.7. After clamping the blade on the rig, next step of the blade assembly was to connect the shaker and stinger on the blade. A front view of the rig with final assembly of the shaker-stinger on the blade is shown in Fig. 3.8. In this view, it can be noticed that the shaker along with its stinger is connected to the blade at an inclination of  $30^\circ$  with horizontal. This inclined assembly of the shaker was decided to avoid the interaction of the lower portion of the shaker with the floor of main table. Therefore, an inclined hole was drilled on the blade to connect the stinger. In case of this inclined shaker configuration first two bending modes are easily excited. However, both bending

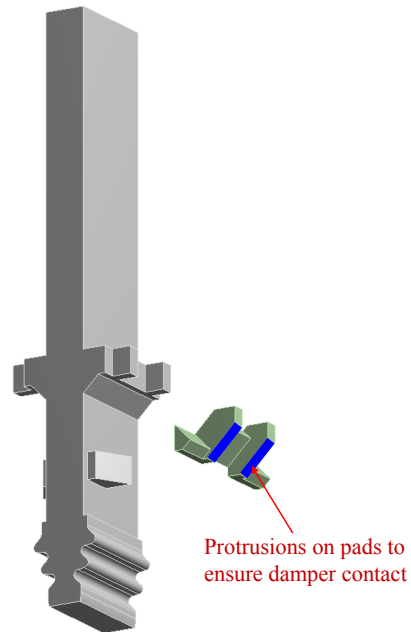


Fig. 3.6 Dummy blade with its removable contact pad

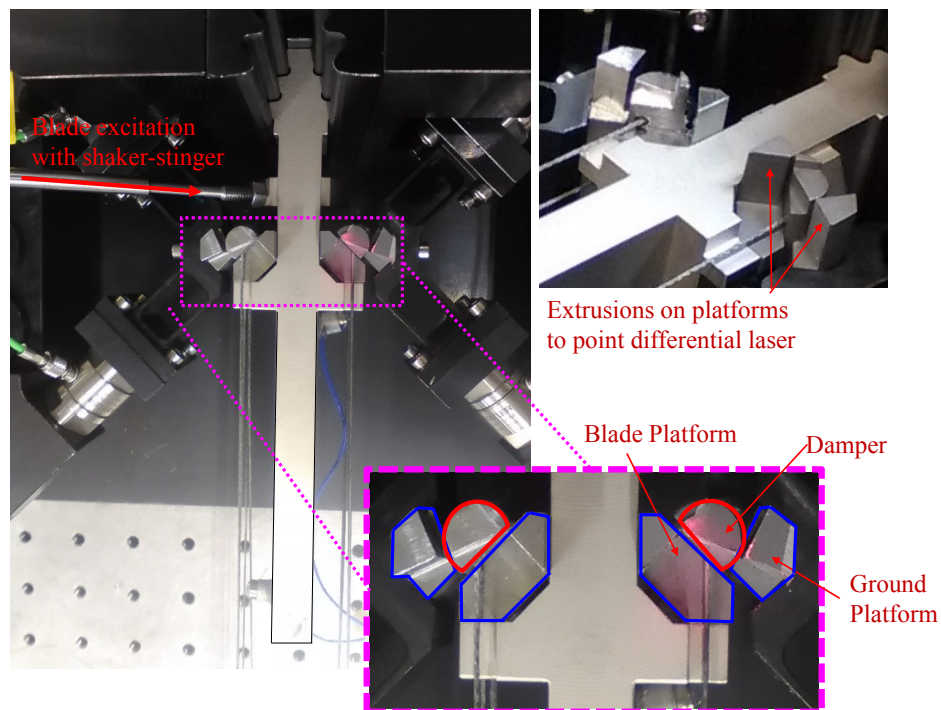


Fig. 3.7 Dummy blade and damper assembly on the rig with platforms and shaker



modes of the dummy blade are well-separated (434Hz and 892hz, see Fig. 3.4) thus the effect of the out of plane forces due to inclined shaker configuration is negligible on the fundamental frequency of blade (investigated here). Further details about the dummy blade specification and stinger connection point can be find on the detailed technical drawing given in Appendix C.

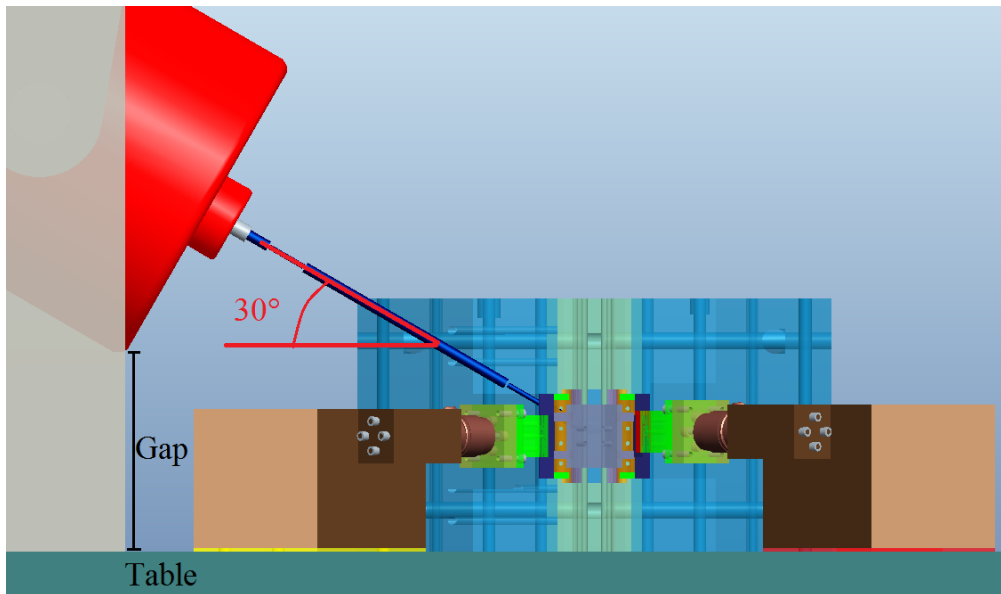


Fig. 3.8 Assembly the shaker with stinger on the blade at an inclination of 30deg with the horizontal to avoid touching the table

## 3.2 Conclusions

A complete procedure to develop the dummy blade with simple and symmetric geometry has been explained. A parametric modal analysis are performed by varying the length and thickens of the blade to get the desired first frequency of the blade. The fundamental frequency of the blade was ensured to be within the range of 400 ÷ 450 Hz, which is the actual frequency encounter by the blade this size. Moreover, it was verified that the first two natural frequencies and their respective mode shapes of the blade are well separated.

# Chapter 4

## Model Identification and model order reduction of blades

*“Good judgment comes from experience. Experience comes from bad judgment.”*

- unknown

### 4.1 Introduction

In this chapter the model identification and model order reduction procedure of the two blades i.e. real turbine blade and dummy blade, has been discussed. These two blades are used throughout this study. When we assemble a blade on the test rig and attach the shaker-stinger assembly with the blade to excite the structure, the dynamics of the blade are affected by these externally introduced interactions from the test rig. Therefore, while modeling the damper-blade system, it is necessary to include the effect of these unavoidable uncertainties in the numerical model of the blade. At the end of this identification and correction, an approximated linear numerical models of the blade is obtained whose dynamic responses is considered to be identical with the actually assembled blade on the test rig. Moreover, as explained in **Chap.1** Sec.1.2.1, model order reduction is commonly performed in this field to reduce the size of full FE model of the blade. In this chapter the procedure and

details of the reduced order modeling technique, applied for both blades, is also described.

This chapter is divided in two main parts, which explain the model identification/correction and model order reduction procedure, for the dummy and real blade respectively.

## 4.2 Dummy blade model

As shown in the Fig. 3.6, the dummy blade was designed with a fir-tree root attachment to match with the available blade adapter to clamp on the test rig. Although the presence of the fir-tree root attachment provides a facility to test real blade root and allows to investigate the relative importance of the damping contribution of the root and under-platform dampers. However, it complicate the experimental set up also and additional efforts are required to separate the damping contribution of the under-platform dampers and that of the fir-tree root itself. In this study the focus is only on the under-platform dampers. Therefore, in this case it is appropriate to apply such a high clamping force on the root of the blade that any damping of the root and its attachment disappear to an acceptable level. In other words, the blade without the dampers should act like a cantilever beam fixed at its one end. The damping contribution of the blade root can be identified and separated by evaluating the variation in blade FRFs (without any damper). In this regard, the variation in the amplitude and frequency of blade for different clamping forces is shown in Fig.4.1 and 4.2. It can be noticed that the variation in FRFs for a clamping force higher than 30KN is negligible. For a clamping force higher than 40KN the blade FRFs seems converging to one curve. At this clamping force, the blade dynamic response is almost consistent. Therefore, it is reasonable to consider that the damping contribution due the blade clamp are almost negligible. So consequently, a clamp force of 50KN was decided and applied on this dummy blade for all the experimental activities during this study. The next step is to match the dynamic response of the numerical model in terms of frequency with the dynamic response of the experimental model without the presence of the dampers. The measured FRFs of the blade without any dampers for a clamp force 50KN has been shown in 4.3. It can be seen in this figure that the value of the first resonance frequency of the blade is about 415.2  $Hz$  which

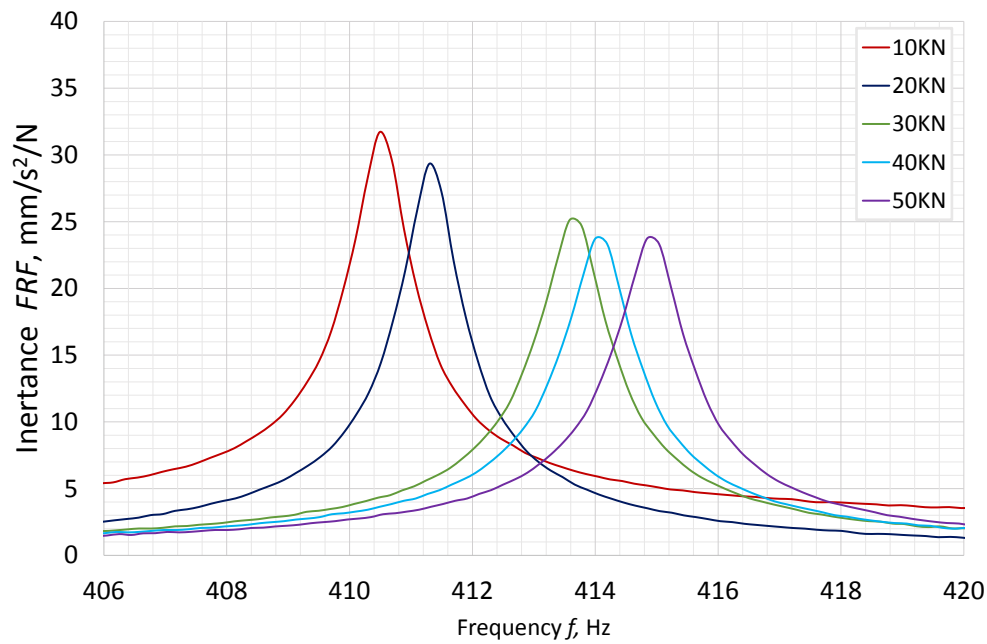
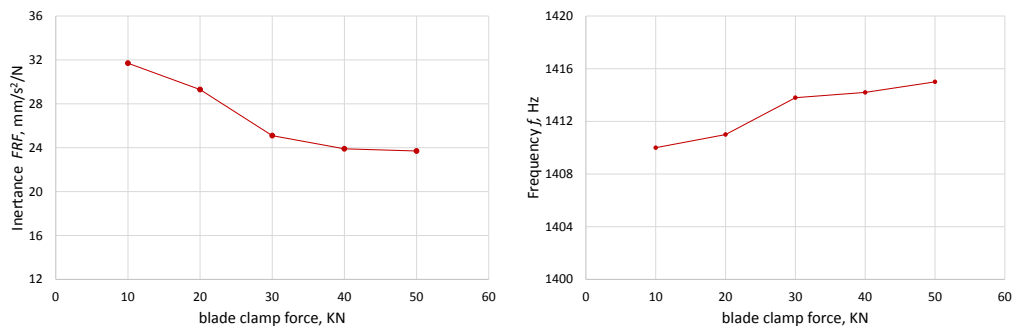


Fig. 4.1 Measured FRFs with impact hammer test on the dummy blade for different levels of the blade clamping force



(a) Variation in the response amplitude at different blade clamping force. (b) Variation in the shift in first resonance frequency at different blade clamping force

Fig. 4.2 Effect of the different clamping force on the response amplitude and shift in frequency of the dummy blade

is different from the numerically computed fundamental frequency (434 Hz) through modal analysis as given in **Chap. 3** Fig. 3.4.

This small difference in the actual and numerical frequencies can be adjusted in several ways e.g. by constraining only few selective root nodes or areas, varying

slightly the material properties, applying some customized boundary conditions at the blade root etc..[106–108]. In case of dummy blade, the commonly used technique of constraining few random root nodes as shown in Fig.4.4, is used to rectify the difference in numerical and experimentally measured blade frequencies. However, this procedure is not precisely the model identification but can be called model tuning/ model correction. These few selective nodes are fully constrained to simulate the clamping of the blade as fixed support in the numerical model. In this method, the nodes are selected by hit and trial method to match the numerically computed dynamic response of the blade with the experimentally measured FRFs. Although this model tuning method is widely used in this field but still it does not produce the real contact conditions at the root of the blade. The numerical result of first three natural frequencies of the blade before ( $f_{num,1}$ ) and after ( $f_{num,2}$ ) this correction procedure are summarized and compared with the experimentally measured frequencies in Table. 4.1. It can be seen that the updated first natural frequency ( $f_{num,2}$ ) of the blade is 411.5 Hz which correctly matches the experimentally measured frequency. However, with this procedure, the difference between the numerical and experimental frequencies for the second frequency increases little bit .

Table 4.1 Comparison between the numerically computed and experimentally measured frequencies of the dummy blade without any damper

	$f_{num,1}$ [Hz]	$f_{measured}$ [Hz]	$f_{num,2}$ [Hz]
1	434.2	414.1	411.5
2	892.2	882.0	839.1
3	2340.0	2239.2	2244.1

These results can be further improved by selecting a different set of constraint nodes on the blade root. However, this node selection process is time consuming and a further improvement for higher natural frequencies is redundant, as in our case, if the fundamental frequency of the blade is investigated only.

Nevertheless, this approach may be convenient of some cases, but has several drawbacks:

- It does not reproduce real contact conditions: since the zero displacement hypothesis is very strong, only a subset of nodes must be constrained if the simulated and measured resonance frequencies have to match.
- The level of the approximation is substantially large, it is sometimes impossible to match higher measured resonance frequencies with this method, thus producing a sub-optimal free model as input to the subsequent nonlinear calculations. Therefore, it is better to use any alternative method particularly if the scope of investigation includes higher frequencies and mode shapes.

Consequently, in case of the real blade, as explained in Sec. 4.3, an alternative method has been introduced to model this clamp effect on the blade.

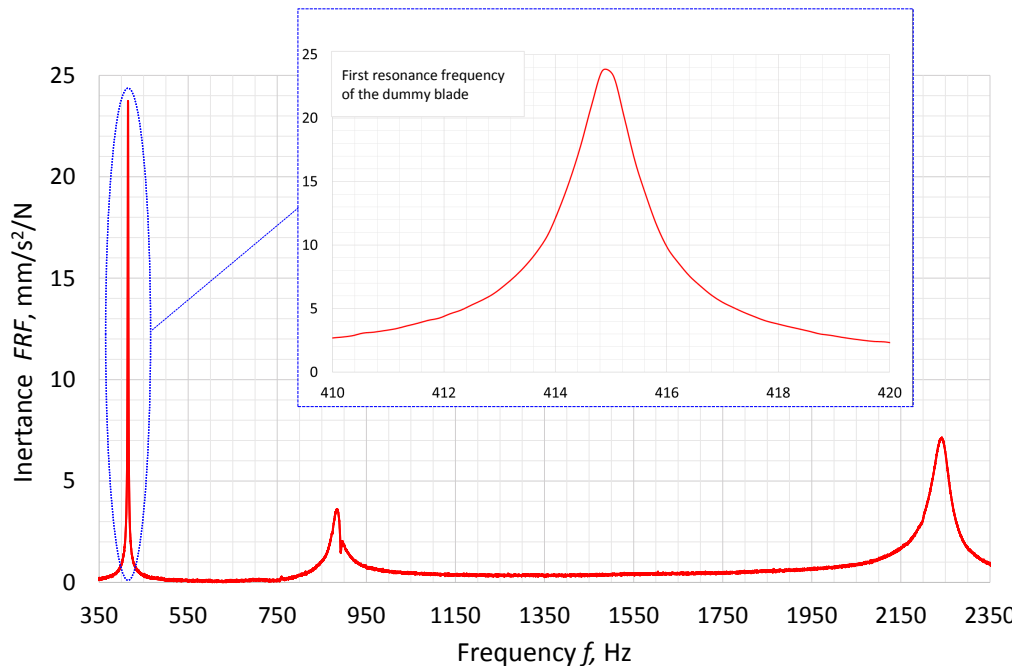


Fig. 4.3 Measured FRFs of the dummy blade at clamp force 50KN

### 4.2.1 Dummy blade model order reduction

The next step is to reduce the size of full finite element model of the blade (reducing the size of mass and stiffness matrices of the blade without losing the accuracy) by a valid model order reduction technique as explained in **Chap. 1** Sec. 1.2.1.

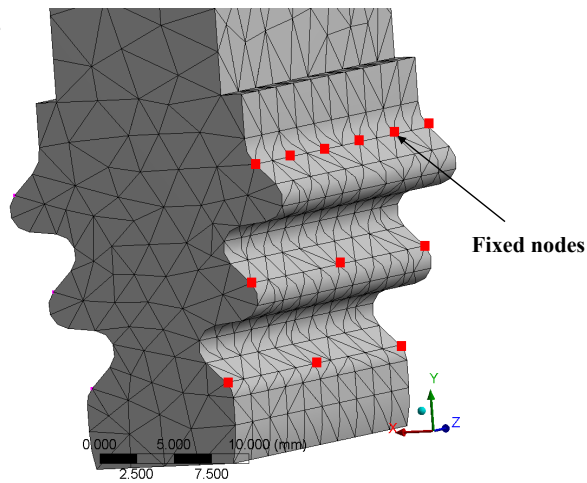


Fig. 4.4 Selected root nodes to match the numerical and experimental dynamic response of the blade without dampers

The Hurty/Craig-Bampton Reduction method also called Hurty/Craig-Bampton Component Mode Synthesis method (CB-CMS), is a commonly used technique to reduce the size of a large finite element model by acquiring the fundamental frequency modes of the structure. Further details about this method can be found in [64, 65].

In this method, only a subset of physical DOFs of the full model, corresponding to chosen nodes, are retained as master DOFs while the remaining DOFs are reduced in a set of orthogonal modes (slave DOFs). In this reduced order modeling technique, the following nodes of the dummy blade (as highlighted in full FE blade model in Fig. 4.4) are selected as master nodes:

- contact nodes correspond to blade platform (left and right side of the blade)
- blade excitation node
- blade response measurement node

In Fig. 4.5, master nodes corresponding to the left platform are not visible due to given orientation of the blade. Further details about the full dummy blade model and its corresponding master nodes are given in **Appendix C** Sec. C.1.

After the reduced order modeling, the fundamental natural frequency of the blade is computed again, which matches accurately with the frequency of the full model, to verify the successful model order reduction.

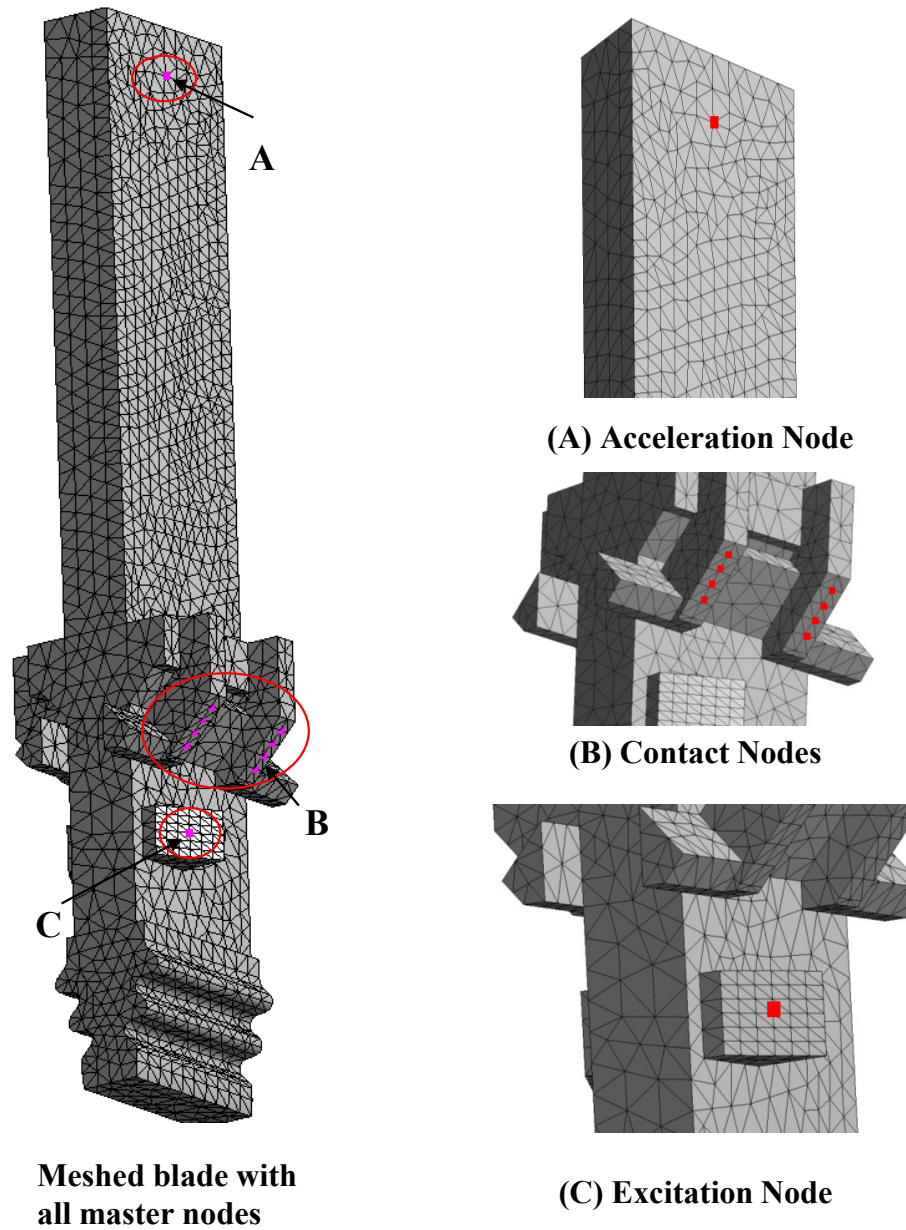


Fig. 4.5 Finite element meshed model of the dummy blade with the selected excitation, contact and response nodes as master nodes



### 4.3 Real blade model

In case of real blade almost the same procedure, as described above for dummy blade, was followed. This time the blade was clamped with much higher clamping force 150KN i.e. the actually experienced by this blade during working of the turbine. At such a high clamping force, the damping contribution from the blade root are almost negligible compared to the damping of the under-platform damper. However, the effect of the test rig clamp, on the small variation in blade frequency, is still present and required to be considered in the blade numerical model. Following material properties of the real blade are used in this model:

- Material = single crystal (SX) turbine airfoil alloy
- density = 8497.7 kg/m<sup>3</sup>
- Young's Modulus = 131.69 GPa
- Poisson's Ratio = 0.37907

This time, instead of fixing few nodes of the blade to correct its natural frequency (as explained for dummy blade in Sec. 4.2), a model identification technique was introduced in which a 3D spring elements were connected Fig.4.6 to the all d.o.f of the nodes corresponds to the blade roots in contact with the blade adapter as shown in Fig. 4.7. When the blade is actually clamped on the rig, the areas indicated below in Fig.4.7 on both side of the blade root only comes in contact. Therefore, all the nodes corresponding to these blade areas are incorporated with these spring elements. These springs are parameterized to match the numerically computed resonance frequency of the blade with the actually measured frequency of the blade clamped on the test rig without any dampers. The 3D spring element can be connected to each selected blade root node which can be further connected either to a corresponding node on the surrounding structure (if the disk is modeled) or simply to the ground (if, as in this case, the bulkiness and stiffness of the blade clamping adapter allows for this simplification.)

The use of a 3D spring element (which can be easily upgraded to an actual contact element capable of slip if deemed necessary) allows modeling the effect of

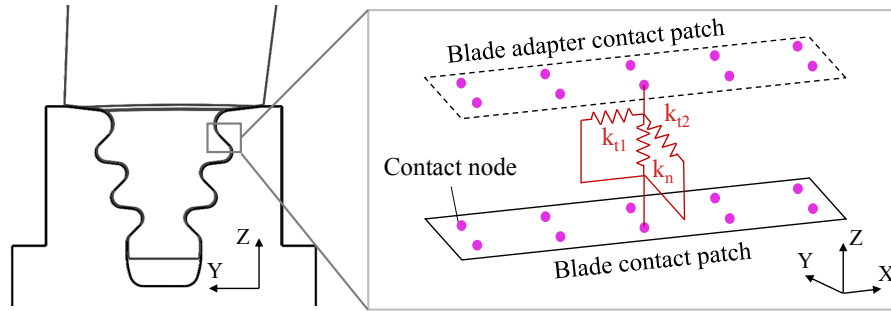


Fig. 4.6 3D spring compliance introduced in the blade numerical model to include the effect of the compliance of the clamp adapter

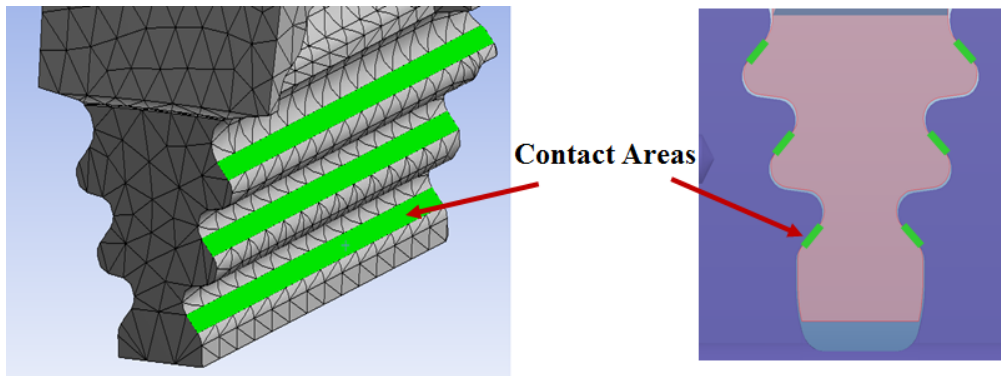


Fig. 4.7 Blade root areas in contact with blade adapter at final clamp position

compliance of the contact interface/blade-clamp in all directions at the blade root. In this method, the 3D spring element needs three calibration parameters:  $k_n$ ,  $k_{t1}$  and  $k_{t2}$  as shown in Fig. 4.6. The values of the springs are determined by imposing that the first three measured frequencies of the clamped blade (i.e. free - no damper) match the simulated natural frequencies:

$$\begin{cases} f_{1,MEAS} = f_{1,SIM}(k_n, k_{t1}, k_{t2}) \\ f_{2,MEAS} = f_{2,SIM}(k_n, k_{t1}, k_{t2}) \\ f_{3,MEAS} = f_{3,SIM}(k_n, k_{t1}, k_{t2}) \end{cases} \quad (4.1)$$

Whereas,  $f_{n,MEAS}$  and  $f_{n,SIM}$  corresponds to the 'Measured' and 'Simulated' frequencies of the blade, respectively. Subscript  $n$  refers the number of the frequency under consideration. The random values of these spring stiffnesses are selected initially and a global stiffness matrix of the blade has been built by including these

additional stiffness values at corresponding DOFs of the respective nodes. Then the blade natural frequencies are computed by simply solving the eigenvalue problem. The values of these three contact stiffnesses which were identified to exactly match the numerical and experimentally measured FRFs peaks are given in Table. 4.2. It can be noticed that the maximum value of the spring is along the Y-axis ( $k_{t2}$ ) as the blade was excited along the same direction in its first bending mode. Similarly, the lowest value of the stiffness corresponds to  $k_{t1}$  along the X-axis (along damper axis) which is the second bending mode of the blade and blade does not move at along that side in its first mode.

Table 4.2 Comparison between the numerically computed and experimentally measured frequencies of the real blade without any damper

<b>Spring stiffness [N/mm]</b>	
$k_n$	46.8
$k_{t1}$	5.24
$k_{t2}$	72.00

Moreover, the experimental measured frequency response of the clamped blade without any damper was also used to identify the structural damping level (i.e. matrix  $C$ ) by matching the numerical and experimental frequency response of the blade, see result in Fig. 4.9. For this reasons, the value of damping ratio for the blade 7<sup>th</sup> mode  $\zeta = 0.32$  was fine-tuned (first 6 modes are the rigid body modes) .

### 4.3.1 Real blade model order reduction

Similar to the dummy blade reduce order modeling (Sec. 4.2.1), the full FE model of the real blade as shown in Fig. 4.8 was also reduced with the same model order reduction technique (CB-CMS). Further details about the full blade model can be find in **Appendix C**. In Fig. 4.8, the master nodes i.e. excitation, response, contact and root nodes, are highlighted. Contrary to the dummy blade case, it can be observed that this time the root nodes of the blades are also considered as master nodes. Previously, in case of dummy blade few selected root nodes were fully constrained and a zero

displacement was given to all the d.o.f of the corresponding nodes. However, this time these nodes are incorporated with the 3D spring element and a valid values of the parameterized spring stiffness are given in all three direction of each root node as explained in Sec. 4.3 in details. After the model order reduction, the blade fundamental frequency is computed again and compared with the full blade model frequency. Both frequencies were found identical with a negligible difference in values. The final result, comparing first three numerical and experimental frequencies, are given in Table. 4.3. It can be noticed that there is no experimental value available for the 3<sup>rd</sup> frequency of this blade. It is because of the fact that it was not possible to excite the blade after 4000 *Hz* with the available electromagnetic shaker . Whereas, the 3<sup>rd</sup> frequency of this real blade is very high (close to 5600 *Hz*). Similar to the dummy blade, we only worked on the fundamental frequency of the blade throughout this thesis which already matches quite accurately as given in Table. 4.3.

Table 4.3 Comparison between the numerically computed and experimentally measured frequencies of the real blade without any damper

	$f_{\text{measured}}$ [Hz]	$f_{\text{numerical}}$ [Hz]
1	1358	1360.1
2	3240.8	3239.4
3	N.A	5610.6

## 4.4 Conclusion

Before modeling the nonlinear damper contacts, it is necessary to have an accurate linear numerical model of the blades which already includes all the unavoidable uncertainties coming from the test environment. A commonly used method of fully constraining the few selective blade root nodes has been applied to match the experimental and numerically computed blade FRFs. However, this method does not reproduce the real clamp and blad root contact conditions and zero displacement hypothesis is very conservative. Therefore, with this method the level of approximation

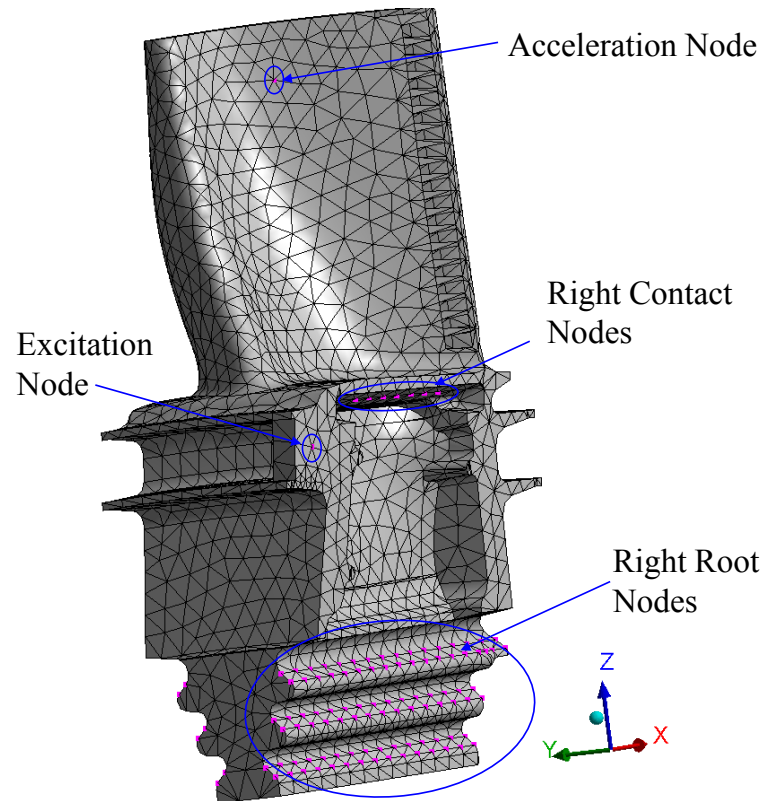


Fig. 4.8 Finite element meshed model of the real blade with the selected excitation, contact and response nodes as master nodes

is substantially large and sometimes it becomes hard to match the higher frequencies. To better deal with this problem, an alternate method has been explained and applied on a real blade in which 3D spring elements were connected to the nodes of the blade root on one end and with the ground on other end. This method simulate the more real conditions which are faced by the blade root due to blade-clamp compliance. Furthermore, Hurty/Craig-Bampton reduced order modeling technique is used to reduced the full finite element model size of the both blades and the results of the reduced blade models were found consistent with the full blade models.

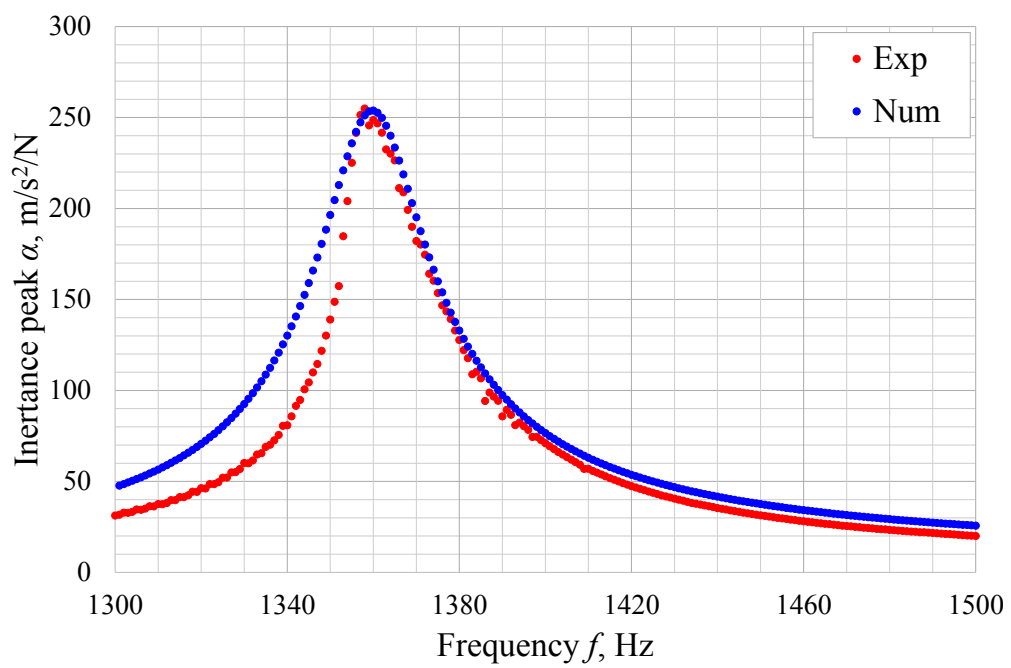


Fig. 4.9 Comparison between the experimental and numerical FRFs at fundamental frequency of the real blade without dampers

# Chapter 5

## Investigation of dummy Blade dynamics in presence of dampers

*"...when you have eliminated the impossible, whatever remains, however improbable, must be the truth."*

- Sir Arthur Conan Doyle

### 5.1 Introduction

The overall objective of this chapter is to investigate the behavior of semi-cylindrical dampers. In this investigation, the results of the measured contact parameters are compared with the previously measured contact parameters of the same damper on a different test rig. Moreover, the blade platform-to-platform kinematics are reconstructed by using the instantaneous center method to understand the damper contact transition during testing. In the end, an adequate macro-slip contact model was introduced between the damper-blade interactions to simulate the behavior of the damper.

In this chapter, the dummy blade (detailed design and FE numerical model of the blade is described in **Chap. 3** and **Chap. 4**, respectively) was tested with two semi-cylindrical dampers which form the flat-on flat and flat-on cylindrical contact

with blade and ground platform respectively as shown in Fig.5.1. A number of results and findings discussed in this chapter have been published in [107].

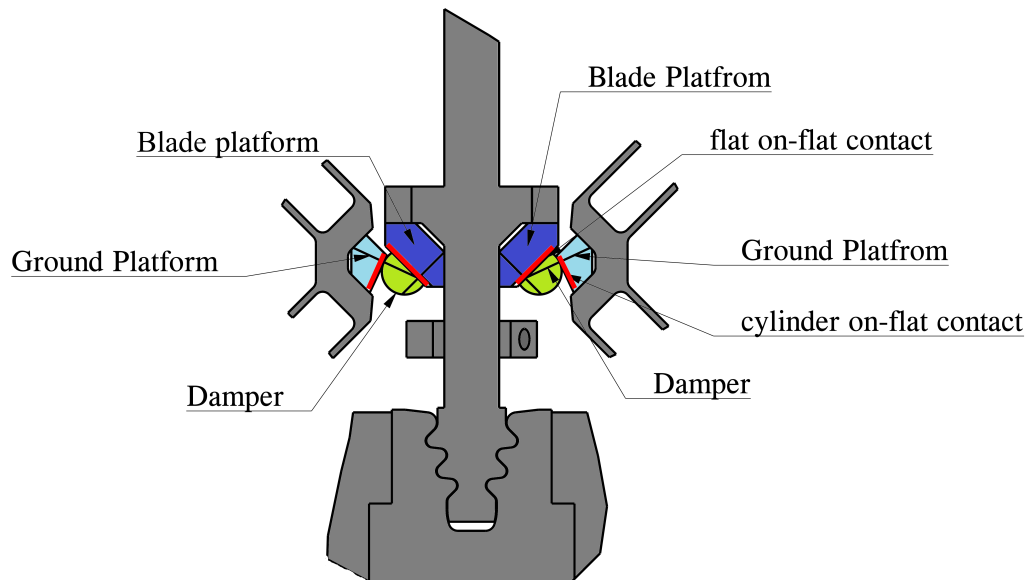


Fig. 5.1 Assembly of the dummy blade with two semi-cylindrical dampers on the test rig. Each damper forms the flat on-flat and cylinder on-flat contact interfaces with the blade and ground platform respectively

## 5.2 Experimental Procedure and Measurements

### 5.2.1 Testing Conditions

After clamping the blade according to the procedure mentioned in Sec. 4.2 Chap. 4 , dampers were placed on the test rig at their nominal positions with respect to blade as shown in the closed top view of the rig in Fig. 5.1. Actual assembly of the blade on the test rig with dampers shown in Fig. 5.2 . As shown in Fig. 5.1a , the static load on the dampers is applied with the help of dead weights and wires passing through a drilled holes in each damper. The blade was excited with an electromagnetic shaker connected near the blade root as explained in Chap. 3. A number of tests were carried out at different static load applied on the dampers at various blade excitation levels. An accelerometer was attached at the tip of the blade to measure the response of the blade for each testing condition (Fig. 5.1a).



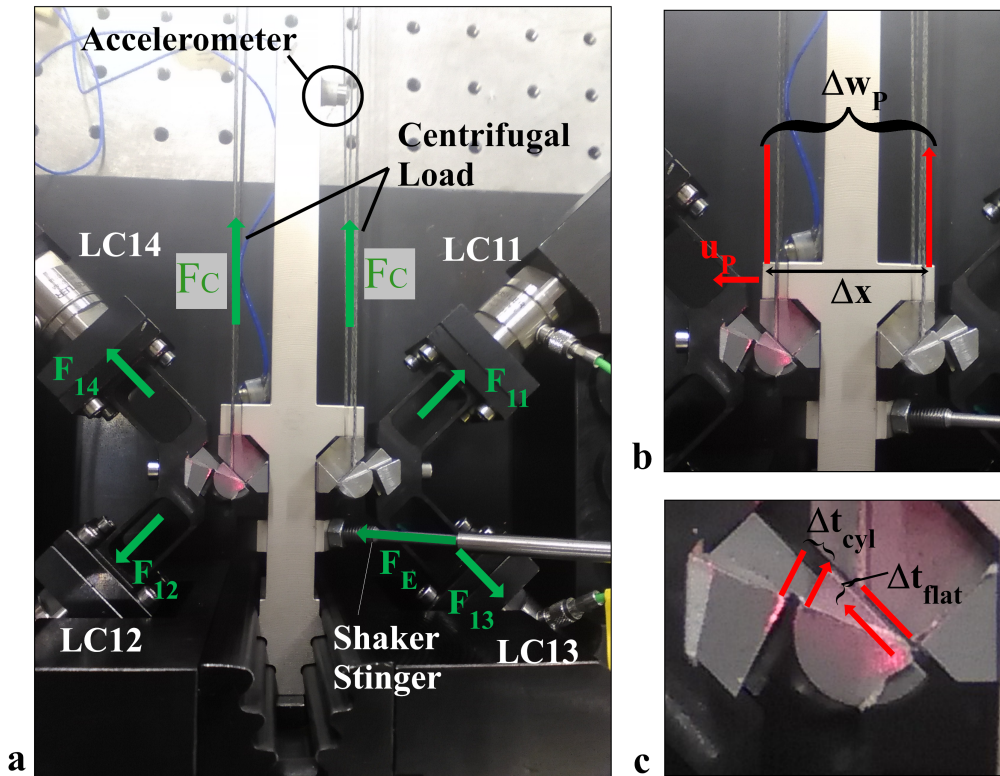


Fig. 5.2 Overall set-up of the test rig (a) applied static damper force  $F_C$ , applied blade excitation force  $F_E$  and measured contact damper contact forces (b) pointing laser beams to record the blade platform in-plane motion (c) to measure the contact relative displacement along tangential direction at the flat on-flat and cylinder on-flat contact interfaces

### 5.2.2 Measured Quantities

Standard frequency response functions (FRFs) of the blade have been measured for different damper static load levels and blade excitation forces. Example of these FRFs can be seen in Fig. 5.4. In these FRFs, measured acceleration amplitude of the blade normalized to excitation force level (i.e. also called inertance) is plotted as a function of excitation frequency. It is already well established that the amplitude, shape and position of the frequency response reveals the existence of the nonlinearities introduced by the contact friction [22, 79]. However, this information provided by the FRFs alone is insufficient to understand the inner kinematic behavior of the dampers. In this chapter, in addition to the standard FRFs, following additional quantities are measured:

### Measured Force Components

As the given test rig is capable to measure the damper contact forces and relative displacement, so it is possible to link a selected point on the FRF with the corresponding damper kinematics. Therefore, in addition to the standard FRFs, damper contact forces are also measured for a given point on FRF. As explained in **Chap. 2** Sec. 2.2.5 and also shown here in Fig.5.2a, the two load cells of the each side of the blade measure complete in-plane contact force components acting along the damper cylindrical side. These load cells are attached with the charged amplifier and allow to measure the dynamic as well as the static component of the contact forces.

### Measured Kinematic Quantities

During this investigation, the relative displacement between the damper and corresponding platform (ground and blade) along the tangential direction of the contact is also measured with the help of differential laser as depicted in Fig. 5.2c. To obtain the hysteresis loop formed at each contact, the measured signals of the relative displacement are plotted with corresponding tangential contact force component. In addition to the hysteresis loops, the following measurements are performed to reconstruct the in-plane kinematics of the blade under-platform:

- using differential laser, the rotation of blade platform  $\beta = \Delta w_P / \Delta x$  is measured by means of a laser differential measurement as shown in the Fig. 5.2b,
- In order to measured the horizontal displacement  $u_P$  of blade platform, a single point laser was placed along one side of the blade as given in Fig. 5.2b.

### 5.2.3 Derived Quantities

Measured contact forces on the dampers and contact relative displacement are post processed to obtain the meaningful results in terms of hysteresis and force equilibrium diagrams. The tangential and normal force components of each damper contact are computed by assuming damper static equilibrium as show in Fig. 5.3.

### Derived Force Components

The contact forces measured by the load cells are transformed from local coordinates into normal and tangential coordinates of the damper contact [97]. The local coordinates formed by the axis of L-Separator limbs are transformed into normal  $N_{cyl}$  and tangential force components  $T_{cyl}$  along the cylindrical damper surface as shown in the Fig. 5.3.

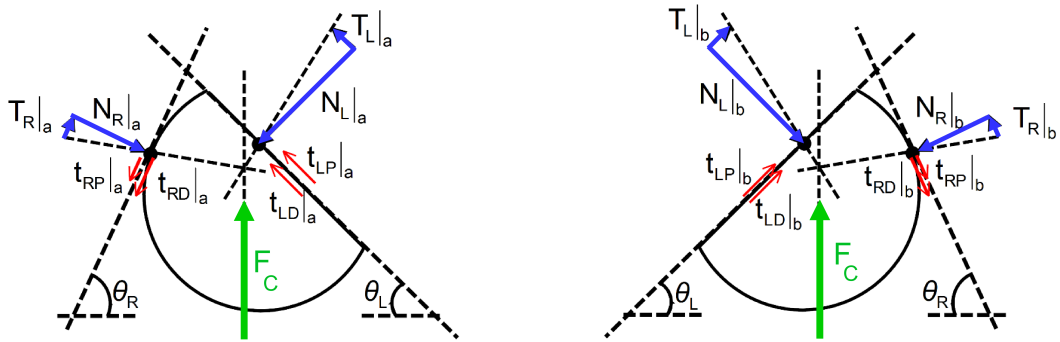


Fig. 5.3 Static equilibrium of the forces on both blade side semi-cylindrical dampers.  $T_{cyl}$  or  $T_{flat}$  and  $N_{cyl}$  or  $N_{flat}$  are the tangential and normal contact forces of the cylindrical/flat damper contact respectively

To compute the contact forces  $N_{flat}$  and  $T_{flat}$  acting on the second damper contact i.e. flat on flat contact, the damper static equilibrium has been applied by neglecting the inertia of the damper (as explained in details in **Chap. 2** Sec.2.2.5 for a different damper-blade combination). The assumption of neglecting damper inertia is valid because the magnitude of damper inertial force is very small i.e. less than 0.1N at the selected working frequency. Therefore, for such a small damper inertial forces, it can be assumed that contact forces and externally applied damper static force ( $F_C$ ) passes through a single point as explained in the [20, 97] and shown in Fig. 5.3. An example of this computation is shown in the results shown in Fig. 5.8

### Derived Kinematic Quantities

Few kinematic quantities are derived by assuming the blade and its platform as a rigid body structure. Due to this assumption, the displacement of the blade platform can be modeled as "instantaneous center of rotation" (ICR). For any rigid body, its planar displacement can be considered as a combination of planar translation and planar rotation. If a rigid body move for a given planar displacement, there is always a point inside the body whose position does not change. In other words, there is always a single point inside a rigid body called "instantaneous center of rotation" (ICR) which does not move and the displacement of all the other points on the body can be observed as a rotation around this point. The dummy blade (see Fig. 5.2) under investigation was purposely designed to be symmetric as explained in the **Chap. 3**. Moreover, a symmetric loading conditions were also applied on the blade by applying an equal static load on both dampers with the help of wires and pulleys. Due to this loading and geometrical symmetry of the blade, it can be assumed that its ICR will exist on the longitudinal axis of the blade. As shown in the Fig.5.10, the planar displacement of the point P, here denote by  $d_P$ , can be computed from the measured horizontal displacement vector of point P and rotation of the blade  $\beta$  as described in Sec. 5.2.2. After getting information of the displacement of the point P ( $d_P$ ), it is now easily possible to get the correct position of ICR vertically along the blade axis. When the actual vertical position of the ICR is known, now its preliminary to determine the displacement of all the points corresponds to the blade platform (i.e. contact point C in Fig.5.10c).

The details of all the measured and derived/reconstructed quantities are given in Table. 5.1. The two "sides" of the blade and the corresponding dampers are here termed "a" and "b", as shown in Fig. 5.3.

## 5.3 Results and Discussion

A first experimental evidence is obtained in the form of frequency response function of the blade to estimate the overall damping effect of the damper presence. It can be observed in the Fig. 5.4a that first resonance frequency which corresponds to first bending mode of the blade occurs at 410Hz without dampers, denoted in the figure

Table 5.1 List of all observed and derived quantities with refer to 5.3

<b>Observed Quantities</b>	
<b>Forces</b>	Right Contact forces $N_R a$ , $T_R a$ and $N_R b$ , $T_R b$
	Blade acceleration amplitude $\alpha$ at the tip in "u" direction
	Relative platform vertical displacement $\Delta w_p = w_p a - w_p b$
<b>Kinematic</b>	Horizontal platform displacement $u_p a/b$
	Tangential relative disp. along flat on-cyl. contact $(t_{RD}-t_{RP}) a/b$
	Tangential relative disp. along flat on-flat. contact $(t_{LD}-t_{LP}) a/b$
<b>Derived Quantities</b>	
<b>Forces</b>	Left Contact forces $N_L a$ , $T_L a$ and $N_L b$ , $T_L b$
	Tangential/normal force ratio $(T_L/N_L) a/b$ and $(T_R/N_R) a/b$
<b>Kinematic</b>	Blade platform rotation $\beta_p = \Delta w_p/\Delta x$

as 'FREE'. Whereas, in the next Fig. 5.4b , at fully stick condition (at excitation force  $F_E = 1$  N) the same resonance peak shifts to approx. 567.5 Hz and also the blade amplitude response normalized by excitation force reduces by one order of magnitude. With refer to the general behavior of dampers, this peak tends to move left towards lower frequency values and also the response amplitude of the blade (normalized with excitation force) also decreases with increase in excitation force level  $F_E$ . For example as shown in Fig. 5.4 b at an excitation force level of ( $F_E = 50$  N), the the first frequency of the blade is down to 530 Hz. This effect of reduction in amplitude response and frequency , is produced by the sliding of under platform dampers which begin to slip against platform contact surfaces and

- dissipates energy due to the relative displacement between two contacting surfaces and therefore reduces the amplitude response of the FRF peak;
- decrease the stiffness introduced by the contact in full stick conditions thus results in decrease in blade frequency.

### 5.3.1 Understanding the puzzling FRFs with measured hysteresis loops

As explained in the above section and shown in Fig. 5.4 that the under-platform damper influences the blade response amplitude substantially. However, this information obtained from the frequency response function is not enough to answer all the questions faced by engineers and experimenters working in the field of turbine blade dynamics. First question is resulted from a very common experimental situation experienced by the engineers on daily basis i.e. sometimes, the frequency response functions produces very strange results which does not describe any particular trend. These inconsistent results are hard to understand and justify. For example, in Fig. 5.4 and Fig. 5.6 a-b it can be observed that the blade amplitude response and resonance peak decreases with increase in excitation force  $F_E$  1 N to 50 N, as expected. However, if we further increase the excitation force level e.g  $F_E \geq 80$  N and 100N, the blade response amplitude and resonance frequency start increasing again. This unexpected behavior was observed repeatedly on various static load values applied on the dampers. It is not possible to explain this kind of behavior with only frequency response functions thus an insight of the damper contact behavior is required to fully understand this phenomenon.

Thereby measuring the contact forces and damper relative displacement, it is now possible to associate a frequency response function of the blade with corresponding behavior of the damper at a given load conditions. The measured hysteresis loops correspond to the cylindrical contact side of the damper at two excitation force levels  $F_E$  (50 N and 100 N respectively) are presented in Fig. 5.5. From the measured hysteresis at  $F_E = 50$  N, it can be observed that the cylindrical contact interface of the damper is in micro-slip regime/at onset of gross slip. Moreover, the numerical results of this hysteresis loop are simulated easily according to the numerical code explained in Sect. 5.2.3 and also shown in this Fig. 5.5. If the hysteresis loop correspond to  $F_E = 100$  N is observed, it can be noticed that the damper is slipping at respective interface and thus dissipating the energy. However, it can also be noticed that for a portion of cycle the damper seems to be "fixed/glued" to the contact surface of the platform. More specifically, there is a significant variation in tangential contact force value but no relative displacement between the damper and platform is present

in that part of the cycle. This partly sticking of the damper introduces an additional stiffness to the system that results in an increase of the blade resonance frequency.

Another unusual and tricky experimental situation faced by the experimenters in this field is the intermittent repeatability of FRFs results for same testing conditions. The FRFs results presented in Fig. 5.4 and 5.6 are acquired by exciting the blade from  $F_E = 1$  N to  $F_E = 100$  N in ascending order. If another experiment is performed on the same load conditions without unloading the dampers but this time exciting the blade in descending order (from higher  $F_E = 100$  N to lower  $F_E = 1$  N), the acquired FRFs results in micro-slip region (i.e. at  $F_E \leq 20$  N) will be noticeably different from the former set. An example of the above given argument is presented in Fig. 5.7 and Fig. 5.8. The results obtained from the numerous experimental campaigns are reported in Fig. 5.7a. These results are collected from several tests to ensure that they are not randomly distributed. Nevertheless, it can be observed that they are quite repeatable provided that initial conditions for each experiment remain unchanged. However, the steady state solution in the micro-slip regime is dissimilar and depends upon the initial conditions, i.e. static force component of contact forces. Yang and Menq[72] pointed out that, for the same input motion, *"different initial states and initial values of the friction forces at the beginning of simulation may result in different friction force trajectories when their steady states are reached"*. More recently it has been pointed out by the authors in [60] that it is not possible to calculate a unique solution to compute the normal preload acting on the damper from static balance equations of dampers at partially stuck conditions of the contact. In fact the under-determinacy on under platform dampers in [26] has been addressed and demonstrated numerically by the authors. Thanks to the test rig that above mentioned numerical observations are validated by experimental counterpart.

Furthermore, it can be noticed from the Fig. 5.8c that the normal static contact force component increases by 50 % if the contact state of the damper undergoes in the gross slip regime (i.e. if the blade is excited with  $F_E = 100$  N). A small value of the static contact force component results in different steady state hysteresis cycles (Fig. 5.7b) and the damper. At this state of the contact in which the static normal contact force component are quite low uncertain and inconsistent steady state hysteresis cycles are produced as shown in the Fig. 5.7b. It can be observed that the hysteresis loop (purple line) is smaller than newly measured hysteresis loop (grey dashed line)

and the damper remains in the micro-slip regime in both cases at the same load conditions. However, the value of the normal static force component is higher in the second case but the damper remains stucked/glued to the contact partly for portion of the hysteresis cycle likewise what happens in the case of  $F_E = 100$  N (see Fig. 5.4 and 5.5). In these two measurements i.e. FRFs and hysteresis loops, the contact behavior of the damper is perfectly compatible with the frequency response of the blade i.e. the contact measurements indicated that the blade frequency peak (resulted from additional stiffening of the contact) and amplitude response increases when the damper contact forces increases.

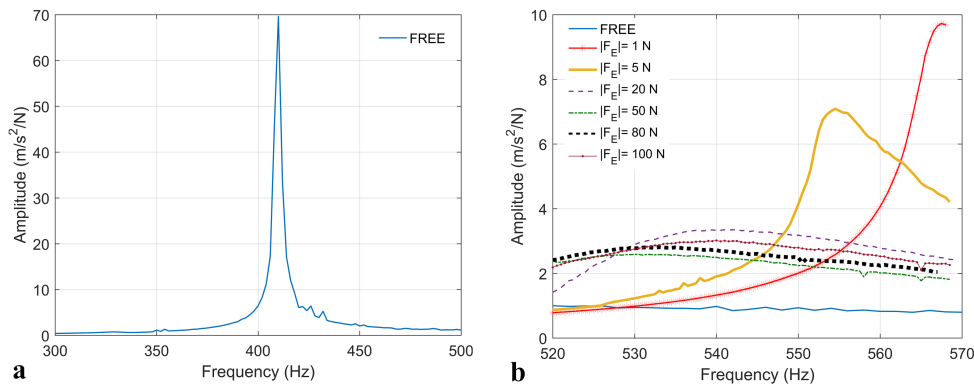


Fig. 5.4 Frequency response function at damper static load level of  $F_C$  46N (a) free blade without any dampers and (b) blade with dampers. Investigation of several excitation force levels  $F_E$

Apart from unveiling a theoretical description of inconsistent FRFs measured at same loading and testing conditions, the cause identification of this discrepancy itself is a worthwhile information to take care of while performing modal testing or contact parameters identification of frictionally damped structures.

### 5.3.2 Experimental results comparison of two independent test rigs

Another challenge faced by the engineers while designing a contact damper- blade system is to model its predictive and trustworthy numerical simulations. It has been



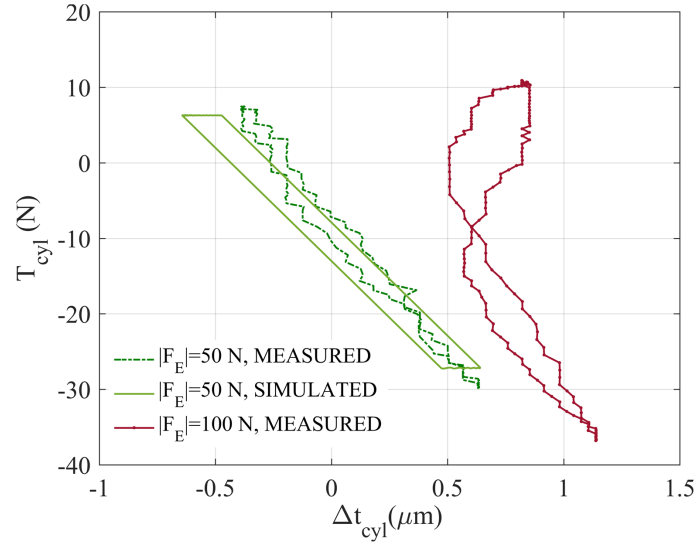


Fig. 5.5 Comparison of the measured and simulated hysteresis cycles along the damper cylindrical contact, with refer to the working conditions shown in 5.4

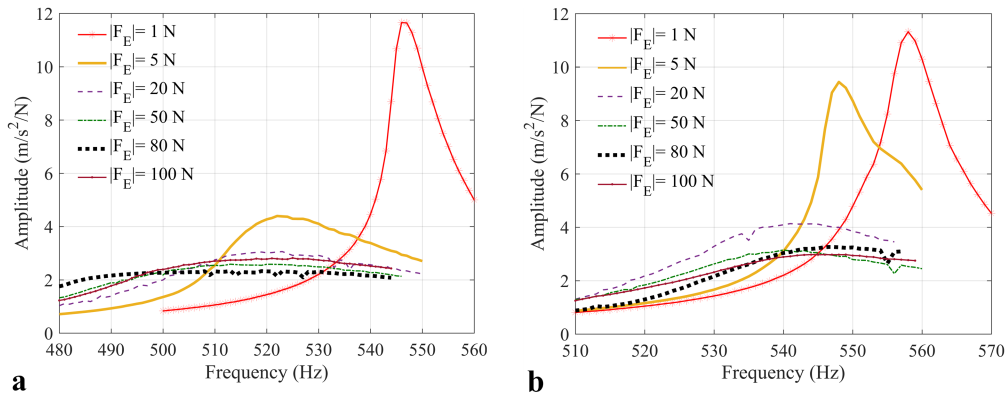


Fig. 5.6 Frequency response functions (FRFs) of the damped-blade system: (a) applied static load on the dampers  $F_C = 26$  N and (b) applied static load on the dampers  $F_C = 66$  N

widely observed from recently obtained results that the available numerical tools (e.g. multi-Harmonic Balance Method, Lagrange multiplier, Analytical-Jacobian Computation etc) are quite adequate provided that the friction contact parameters are accurately estimated.

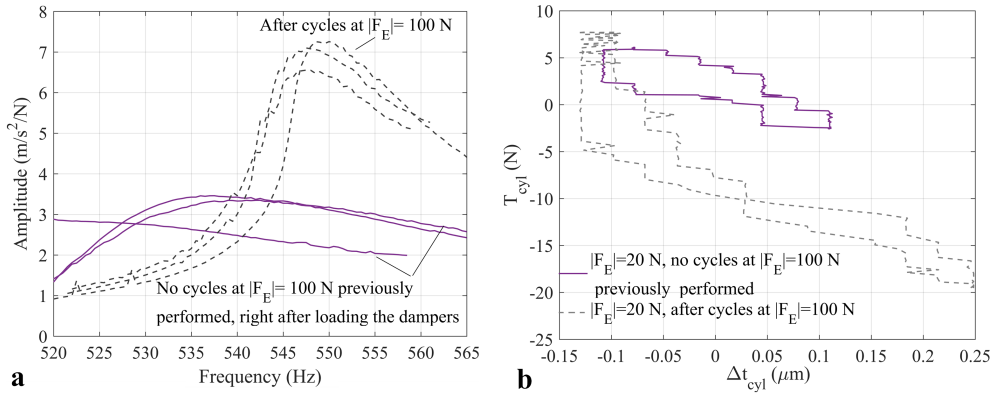


Fig. 5.7 (a) Comparison of frequency response function and (b) hysteresis loops at the damper cylindrical contact with different initial conditions. In the comparison the dampers were loaded with  $F_C = 46\text{N}$ , and the blade was excited with a force  $F_E = 20\text{N}$ .

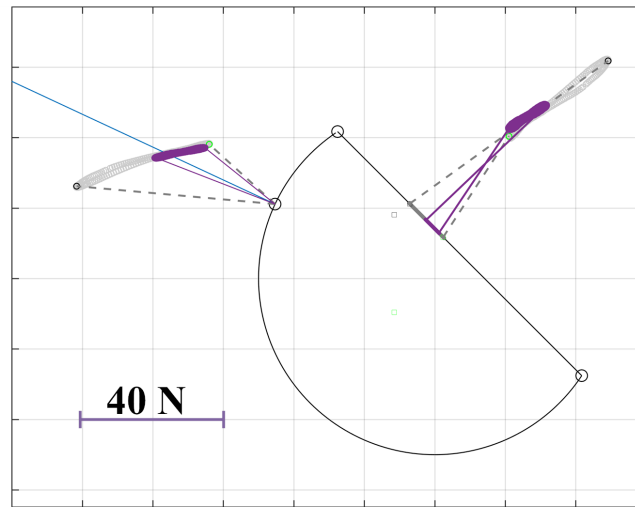


Fig. 5.8 Damper force equilibrium, the corresponding FRFs and hysteresis loops at given load conditions are shown in Fig. 5.7; force scale shown in the figure.

For this reason, a novel technique, based on experimental evidences, to estimate the contact parameter was developed by Gola in [20], further updated in [109], where no blade was present and a single damper was placed between two dummy platforms.

The same technique is applied on the experimental data presented in this chapter to estimate the damper contact parameters. The obtained results are compared with those presented previously in [25] and [109], measured on a different test rig [1], since in both cases the tests were performed on the same dampers with same damper static load conditions  $F_C = 46\text{N}$ . However, the only difference between two experimental setups is the damper configuration with and without the blade on new and old test rig, respectively. In former case the damper was tested between two platforms without the presence of any blade whereas, in this new test rig dampers are placed on a blade as already explained in 5.2.1.

To compare the results of two test rig, a case of  $F_E = 100\text{ N}$  (similar to the one in Fig. 5.4b) has been considered. This particular case has been selected to ensure the cylindrical contact to reach gross slip. Specific points on the hysteresis diagram (e.g. Fig. 5.9b) and T/N diagram (e.g. Fig. 5.9a) are marked with the same corresponding numbers for a better cross-comparison between the damper state on the hysteresis loop with respect to change in T/N ratio. Details of this result comparison is given in Table: By analyzing these diagrams, following observations on the damper cylindrical contact are concluded and compared with former results:

- from markers 1 to 2 the cylindrical contact is sliding since the  $T_{cyl}/N_{cyl}$  is constant and equal to a maximum, in that case  $\mu_{cyl} = 0.6$ , exactly the same value measured on the damper-only test rig; [25]
- from markers 2-3 and 5-1 a sharp increase of tangential force without any associated movement is recorded;
- from markers 2-5 the state is stick, the measured tangential stiffness  $k_{tcyl} = 35\text{ N}/\mu\text{m} \pm 9\text{ N}/\mu\text{m}$ , perfectly compatible with the  $30\text{ N}/\mu\text{m} \pm 7\text{ N}/\mu\text{m}$  measured on the old test rig as presented in [109].

In these experiments it was not possible to estimate the coefficient of friction along flat-on-flat contact as also given in 5.2 N.A (not available), because this interface of the damper contact does not reaches to the gross slip condition as shown in the Fig. 5.9 a by the sinusoidal signal of  $T_{flat}/N_{flat}$  ratio. Moreover, the value of tangential stiffness  $k_{tflat}$  of this flat-on-flat contact was estimated in the range 20-70  $\text{N}/\mu\text{m}$ , quite compatible with those recorded previously on th other test rig in

Table 5.2 Comparison between the damper contact parameters measured at two different test rigs

Test Rig	$\mu_{cyl}$	$\mathbf{K}_{t,cyl}$	$\mu_{flat}$	$\mathbf{K}_{t,flat}$
Old Test Rig-Piezo Damper Only	0.6 ÷ 0.7	30 ± 7	0.45 ÷ 0.55	25 ± 5
Novel Test Rig-Blade Resonant	0.6	35 ± 9	> 0.40	N.A

[109]. The amplitude of  $\Delta t_{flat}$  is lower than  $0.1 \mu\text{m}$  in all investigated cases, a value which is too low to allow a reliable determination of  $k_{t,flat}$ . Such a small relative displacement amplitude which does not allow gross slip between the interfaces, as shown in Fig. 5.9a, are actually because of the limitation of this experimental setup.

In this new test rig, the relative displacement between the damper and platform surfaces depends upon the kinematic, mode shape and stiffness the blade structure. Therefore, it was not possible to achieve any considerable relative displacement even if a high excitation force is applied, as also demonstrated in Sec. 5.3.3. Whereas, in the case of [109], a controlled relative displacement was given as an input to the damper-platform with the help of piezo-actuators, which makes it possible to easily achieve the gross slips on both damper interfaces. Therefore, the generalized slip conditions are not possible to verify on this novel test rig.

### 5.3.3 Blade platform motion reconstruction

Another important objective of this investigation was to understand the blade platform (as shown in Fig. 5.1) kinematics. The in-plane blade platform input motion can be reconstructed with the procedure explained in Sec. 5.2.3. The results of this blade platform-to-platform kinematic are reported in Fig. 5.10. From these results following provisions can be established:

- the mode of the blade vibration can be identified by the position of the Instantaneous Center of Rotation (ICR), e.g. for a purely In-Phase motion (vertical displacement of the platform) the ICR lies inside the platform itself. Whereas, for a purely Out-of-Phase motion the ICR vertical position moves infinitely down towards the center of the hypothetical bladed disk;

- the investigated dummy blade in free form without dampers (just like a cantilever beam) displays an ICR in an intermediate position, more specifically it exist in the middle of the "neck" of the blade, consider that its root is not visible in Fig. 5.10;
- in-plane motion of the blade platform is effected in two ways by the presence of the under platform dampers (see Fig. 5.10b): on one hand the amplitude of motion dramatically decreases, whereas on the other it shifts the ICR upwards, thus modifying the direction of motion as well as the amplitude;
- it can be observed by comparing the Fig. 5.10b and c that the amplitude of the motion is effected significantly by excitation force level  $F_E$  however, it does not alter the position of the ICR (and thus the direction of motion also remains unchanged).

The procedure described in Sect. 5.2.3 has been applied to the case reported in Fig. 5.10c to reconstruct the in-plane motion of the points belonging to the contact patch (as indicated in the figure by point C). The resulting displacement  $d_C$  is almost orthogonal to the flat-on-flat contact, it is therefore not surprising that the flat-on-flat contact fails to reach the slip condition even at high forcing levels.

### 5.3.4 Numerical simulation of the damper performance

In the numerical simulation of the damper behavior, the model fully described and presented in [20] is used. This model represent the damper as rigid body between two platforms as shown in Fig. 5.11. Inputs to this numerical model are:

- the platform motion signal  $d_C$  reconstructed as in Sect. 5.2.3
- friction contact parameters estimated in [109] and confirmed by the measurements during this investigation in Sec. 5.3.2

The resulting force equilibrium diagram is reported in Fig. 5.12b. This compares well with the measured counterpart shown in Fig. 5.12a, thus confirming the soundness of the measurements and the interpretation of experimental results.

## 5.4 Conclusions

The capabilities of the novel test rig allow an insightful investigation into the damper behavior. Namely for each point on a FRF the corresponding hysteresis at the contacts, force equilibrium and platform kinematics can be produced. This set of diagrams is particularly helpful in explaining the unexpected phenomena (e.g. FRFs lack of repeatability) which often make experimental characterization of damper-blade systems difficult.

The test rig can be used to estimate friction contact parameters, which compare extremely well with the values found for the same damper on an independent test rig (damper-only test rig). These findings speak for the soundness of both test rigs and for the estimation procedure itself.

The platform input motion produced by the blade mode shape is quite different from the pure In-Phase motion which was used as a reference case on the damper-only test rig. It can therefore be concluded that the platform motion (linked to the blades mode shape) does not affect the values of friction contact parameters. It can, however, strongly influence the damper performance. Specifically in the case examined here the platform input motion, reconstructed through a purposely developed technique, is almost orthogonal to the flat-on-flat interface, which, as a result, fails to reach the gross slip condition. This hypothesis is confirmed by the results of a numerical model representing the damper between a set of platforms.

These results highlight the importance of considering the blade mode shape and kinematics to achieve a full understanding of the damper-blade system dynamics.

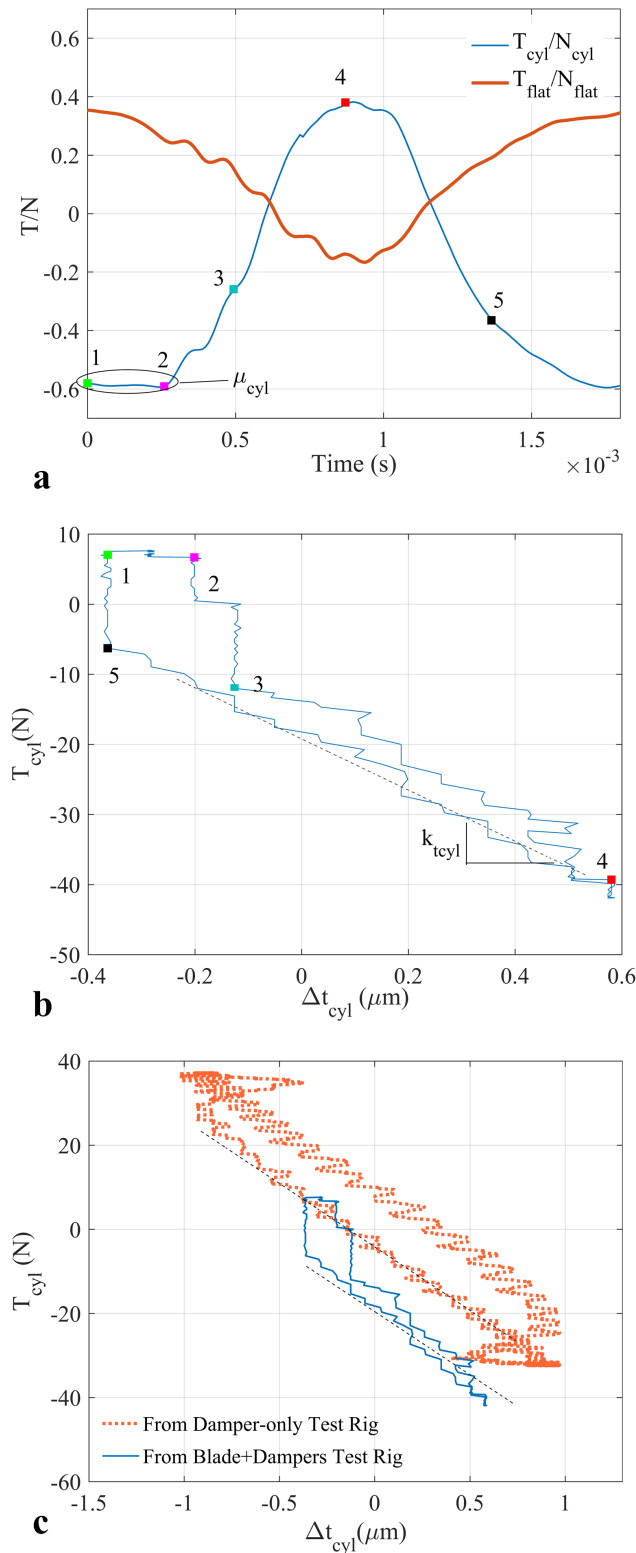


Fig. 5.9 (a) Force ratio between the tangential and normal force component and (b) hysteresis loop along the cylinder on-flat contact interface (excitation force level  $F_E = 100$  N; static load on dampers  $F_C = 46$  N). (c) Comparing the slopes of the hysteresis loops at the cylinder on-flat contact interface of the same damper measured on the two different and independent test rigs.

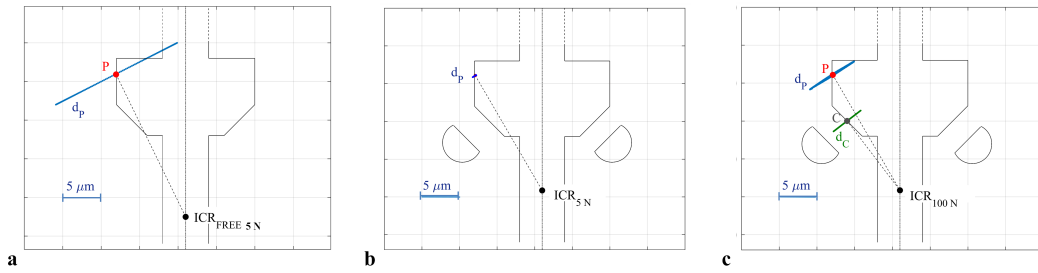


Fig. 5.10 Reconstruction of the in plane motion of the blade: (a) free blade with excitation force level  $F_E = 5$  N, (b) damper loaded with static load level  $F_C = 46$  N and blade excitation force level  $F_E = 5$  N and (c) damper loaded with static load level  $F_C = 46$  N and excitation force level  $F_E = 100$  N (c)

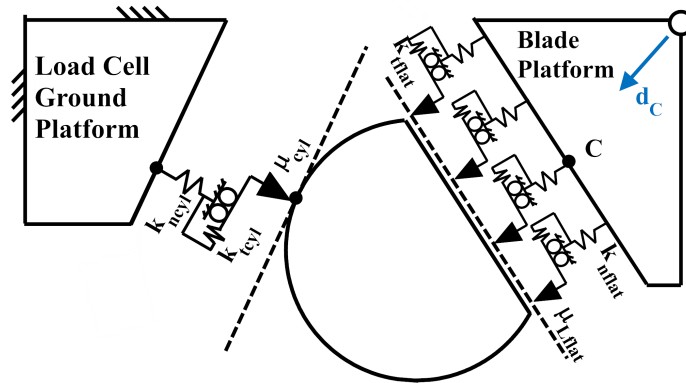


Fig. 5.11 Numerical model of the damper

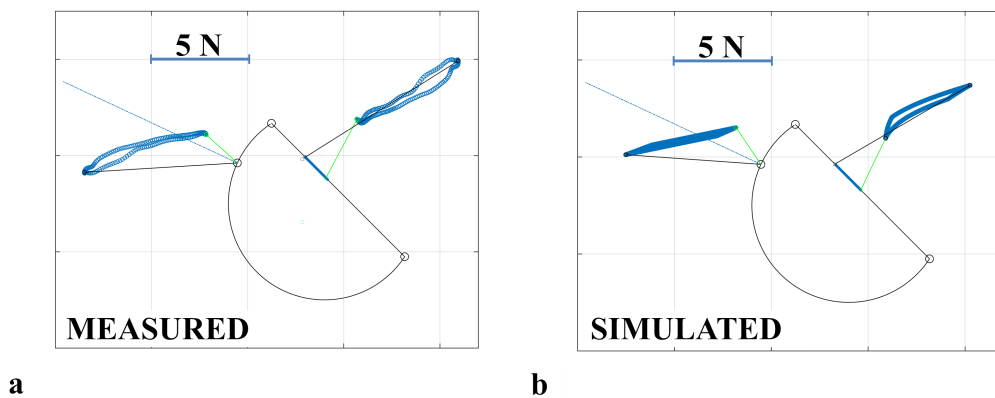


Fig. 5.12 Comparison of the measured and simulated damper force equilibrium (a) Measured and (b) simulated contact forces on the damper for  $F_C = 46$  N and  $F_E = 100$  N



# Chapter 6

## Contact force measurements and contact parameters estimation

*“The opposite of a correct statement is a false statement. But the opposite of a profound truth may well be another profound truth..”*

- Niels Bohr

### 6.1 Introduction

In this chapter, the effect of static and dynamic contact forces on the response of the blade has been investigated. Moreover, for the very first time an attempt has been made to associate the "local/contact" behavior of the dampers with the dynamic response of the damper-blade system, here so called the “macro-dynamic/global” behavior. Local/contact behavior of the dampers is defined by the equivalent contact stiffness and damping, estimated from the measured hysteresis loops. In this regard, a numerical method has been presented to estimate these equivalent contact parameters. The ultimate goal of this newly proposed idea of associating the contact and macro-dynamic behavior of the dampers-blade system is to provide a different and more realistic prospect of studying the under-platform dampers. A part of this chapter has been published in [88].

This chapter is divided into three main parts. In the first part, variation in the static contact forces at the same damper static loads has been investigated. After observing the significant different in the static contact forces, the investigation is further extended to observe their effects on the blade FRFs and contact hysteresis loops. In the second part of this chapter, a brief description of a numerical method to estimate the equivalent contact stiffness and damping, from the measured contact forces and damper relative displacement, has been described. Finally, in the last part of this chapter, a novel strategy has been presented to relate the contact parameters variation with the dynamic response of the blade.

All the tests were performed using a real turbine blade (numerical model of the blade is already discussed in **Chap. 4**), made of single crystal nickel based alloy, with two cylindrical dampers as given in Fig. 6.1. The mass of each damper is 4 g that makes the inertial forces on the damper negligible.

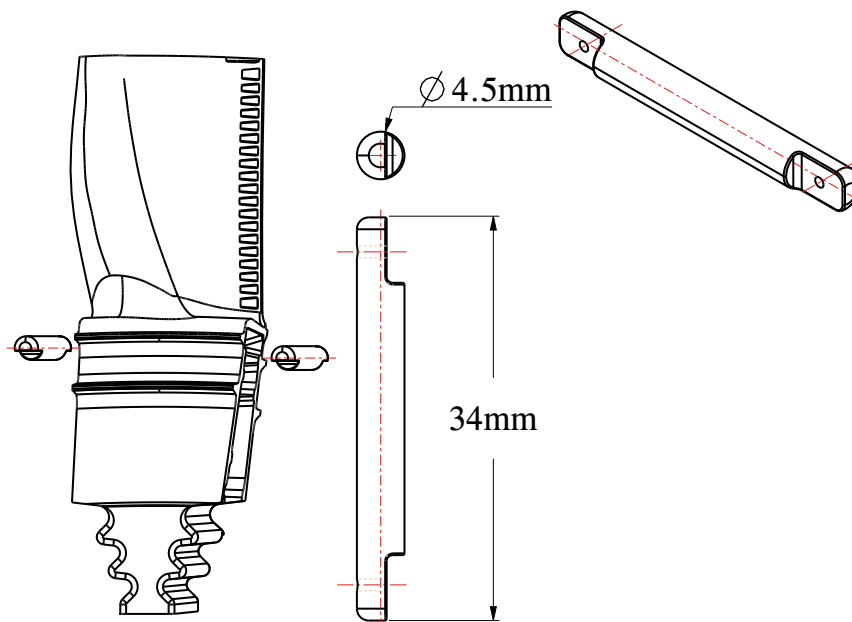


Fig. 6.1 Actual turbine blade with two cylindrical dampers. On the right side a damper front and top views are enlarged to show its dimensions

## 6.2 Damper Contact Forces

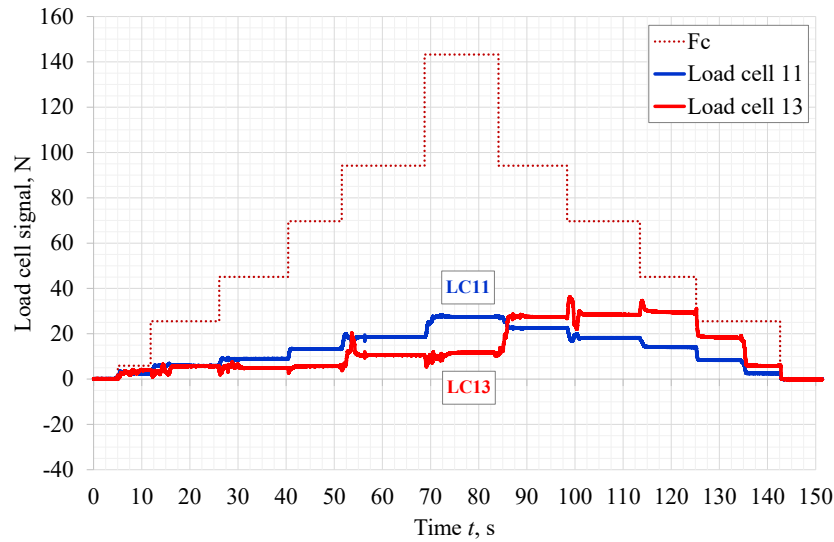
Static load on the dampers is applied with a particular sequence, named here loading and unloading sequence, to observe the variation in static contact forces at the same damper load levels. This applied static load simulates the effect of centrifugal force experienced by the dampers while the turbine runs as described in **Chap. 2**. In this first experiment no external excitation force was applied on the blade.

### Damper Static Loading Technique

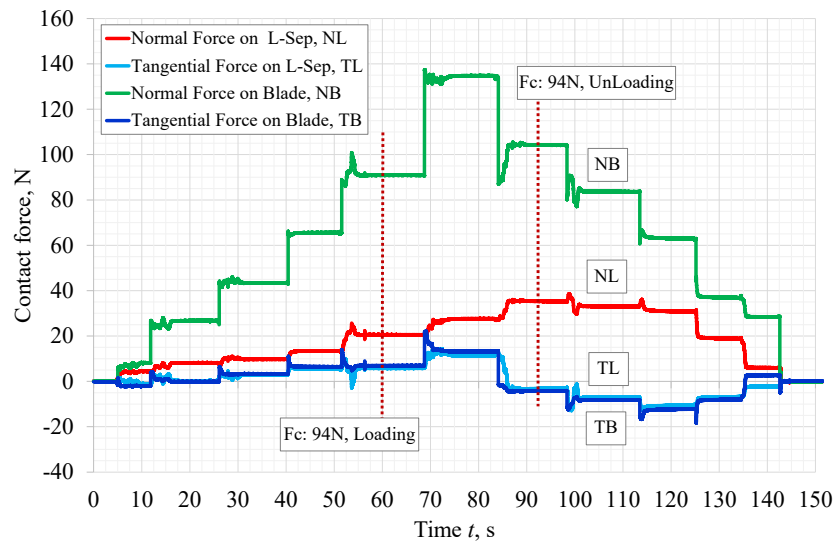
In the first sequence, the dampers were loaded monotonically up to a target value with equal steps, called loading sequence. At each loading step, the static contact forces on the dampers were measured with the help of corresponding load cells on odd and even side dampers as shown in Fig. 6.2a and 6.3a respectively. Whereas, in the next part of this experiment, applied static load on the dampers is removed step-wise after reaching target value (with the same step value as used previously), called unloading sequence.

Then the measured contact forces between the damper and ground platform on both dampers are used to compute the contact forces acting along damper and blade platform (see Fig. 6.2b and 6.3b) by applying the damper static force equilibrium as explained in **Chap. 2** Sec. 2.2.5.

It has been found that the contact forces measured by the load cells are not equal in both loading and unloading sequence at a same applied static load on the dampers (see Fig. 6.2a and 6.3a). Therefore, to investigate this discrepancy in the contact forces, the FRFs are measured for both loading and unloading condition while applying the same static load levels on both dampers. In these frequency response measurements, the blade was excited at an amplitude of 5N with a stepped-sine excitation force signal. The measured FRFs with the dampers at both loading sequence are shown together with the FRF of the blade without any damper (called FREE) in 6.4. It can be noticed that the both FRFs with dampers (for loading and unloading) have higher frequency shift with a lower response of the blade thus emphasizing the effect of under platform dampers. However, if we observe closely the two FRFs of blade with dampers (by comparing the loading FRF with unloading



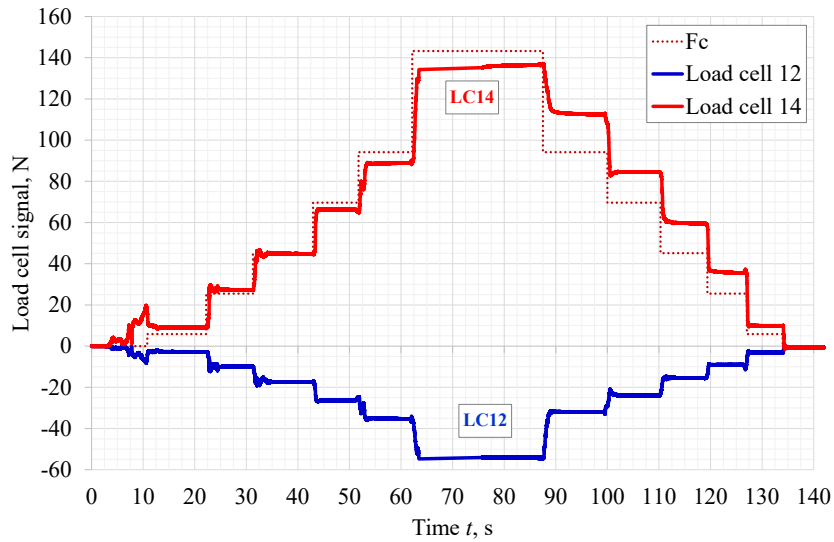
(a) Static forces measured by the load cells 11 and 13 during the loading and unloading sequence.



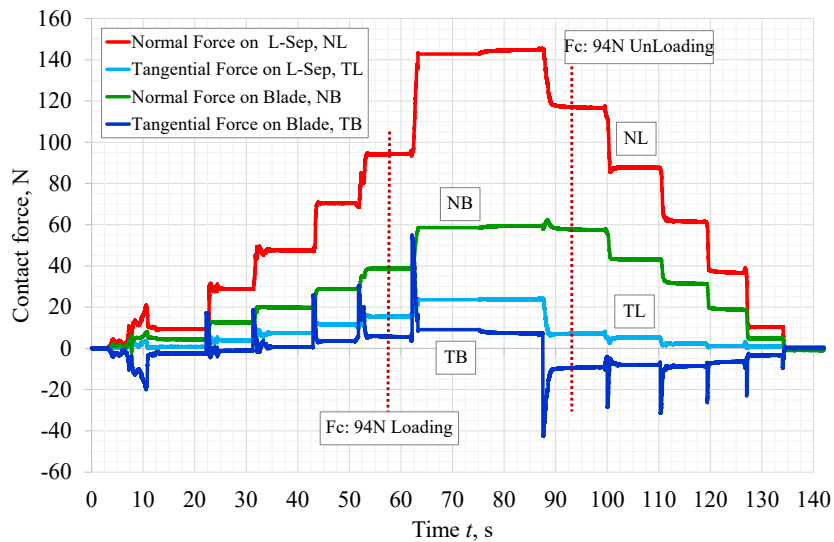
(b) Derived static contact forces on the L-Sep and on the Blade during the loading and unloading sequence.

Fig. 6.2 Static forces on the odd side

FRF), it can be seen that the FRF correspond to the unloading sequence has higher frequency and lower amplitude than the loading FRF. The same results were found by repeating this experiment several times at different damper static load values. This behavior was also observed numerically in [60] in which a damper-blade model was



(a) Static forces measured by the load cells 12 and 14 during the loading and unloading sequence.



(b) Derived static contact forces on the L-Sep and on the Blade during the loading and unloading sequence.

Fig. 6.3 Static forces on the even side

studied for the forced response calculation and it was stated that "... *non-uniqueness of normal pre-loads leads to non-uniqueness of the forced response of the system.*"

From these measured FRFs modal parameters were computed for loading and unloading conditions. A modal identification of a single degree of freedom system

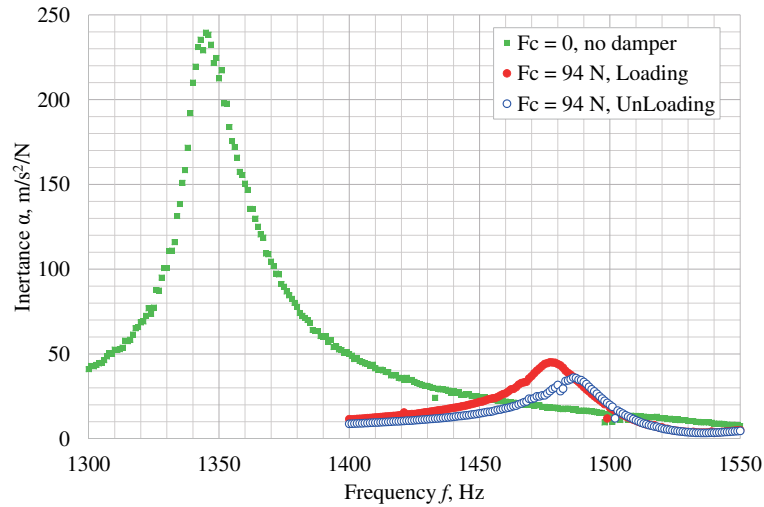


Fig. 6.4 Frequency response of the blade without dampers and with dampers loaded with 94 N.

was implemented by best fit procedure. In this identification three modal parameters namely the natural frequency  $\omega_n$ , equivalent stiffness  $k_{eq}$  and the viscous damping ratio  $\zeta$  were extracted from the response curves and introduced in the 1DOF system. Figure 6.5 shows the results of this curve fitting and values of the corresponding modal parameters. It can be noticed from these estimated parameters that the damping ratio of the blade with damper and without dampers are almost identical. However, the main effect of the dampers is to increase the structural stiffness of the blade by coupling it with the support of ground platforms. Therefore, any reduction in the response of the blade and increase in its frequency is largely due to the increase in its stiffness.

To better understand this variation in the frequency response of the blade, the damper dynamic and kinematic behavior was also investigated. Therefore, in addition to the damper contact forces, the relative displacement between the damper and blade contacts was also measured in a new experiment with the help of differential laser vibrometer as shown in Fig. 6.6. A same excitation force of amplitude 5N on the blade was applied, in this new experiment, closed to its first resonance for both loading and unloading conditions. The tangential contact force component and measure relative displacement give a well-know hysteresis loop of the contact. Both measured hysteresis loops of the loading and unloading conditions are shown in

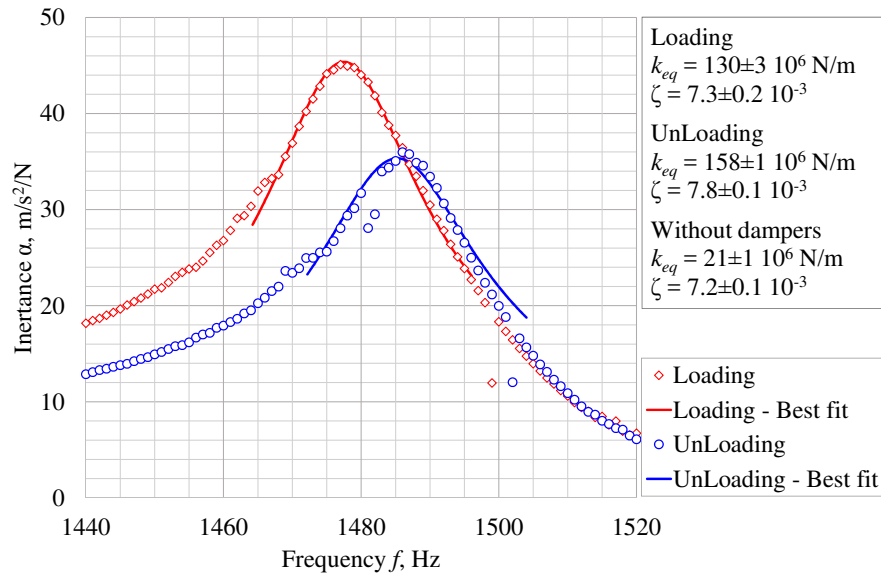


Fig. 6.5 results of the best fit performed in Loading and UnLoading condition with centrifugal force  $F_C = 94 \text{ N}$ . The objective function is a single degree of freedom model. Modal stiffness and damping are reported also for blade without dampers.

Fig. 6.7. The slope of the hysteresis loop represents the corresponding tangential stiffness of the contact as already explained in **Chap.1**. Moreover, this slope can also be computed numerically by linearizing the contact with an equivalent contact stiffness as explained in the Sec.6.3.

By graphically measuring the slope of both hysteresis loops (and also verified by numerical computation), it has been found that the value of the tangential contact stiffness during unloading sequence is  $k_T = 16.6 \text{ N}/\mu\text{m}$  always higher than loading sequence that was estimated as  $k_T = 13.7 \text{ N}/\mu\text{m}$ . This observation is consistent with the dynamic behavior of the blade shown by FRFs in Fig. 6.4 and also support the modal stiffness calculation given in Fig. 6.5.

### 6.3 Estimation of Contact Parameters

The friction contact can be replaced by a stiffness and a damper provided their effect on the whole system is equivalent, from a dynamic point of view, to that of the

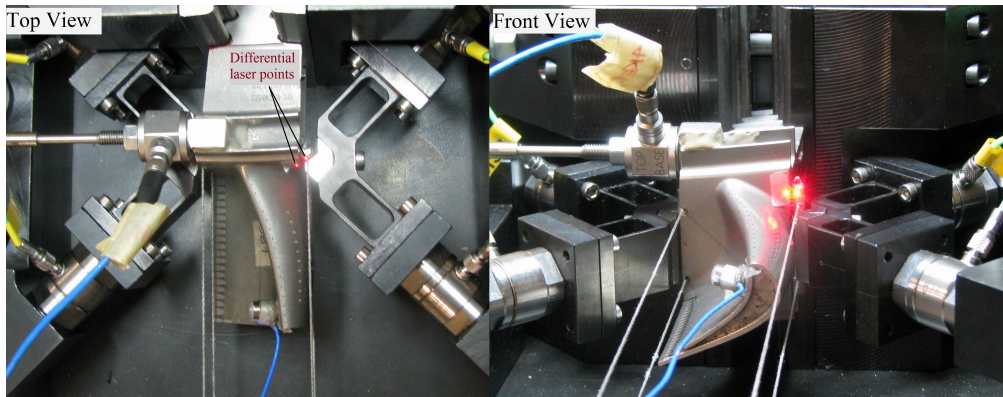


Fig. 6.6 Top and front view of the damper-blade assembly with differential laser points to measure the tangential relative displacement between the damper and blade

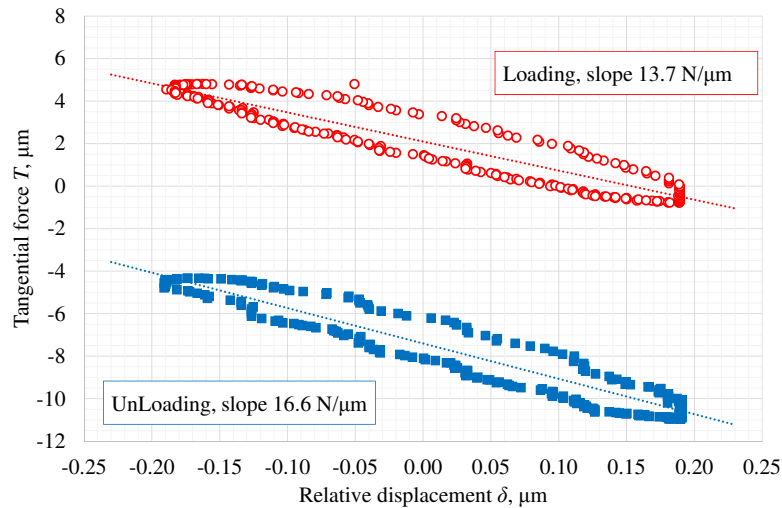


Fig. 6.7 hysteresis loops measured in Loading and UnLoading conditions. The equivalent stiffness (slope) is reported for both conditions. The applied centrifugal force is 94 N.

original friction contact. If such equivalent stiffness and damper are determined a linearized dynamic system can be obtained. In this estimation method a linear spring and a viscous damper were assumed to simulate the effect of the friction contact. In a linear system, the elastic forces are in phase with the displacement. For a given force  $F$ , its elastic component can be obtained by projecting the force along the displacement (inner product) and averaging the result on one period of the



oscillation. If the system is non-linear, this projection gives the linearized part of the elastic force from which the “equivalent” elastic stiffness can be derived. In this way, the equivalent stiffness can be written as:

$$K_{eq} = \frac{\int_{\tau} \langle T, \delta \rangle d\delta}{\int_{\tau} \langle \delta, \delta \rangle d\delta} \quad (6.1)$$

Similarly, the equivalent damping can be computed by observing that the viscous damper force  $F_{vd}$  is in phase with the velocity.

$$F_{vd} = C \cdot \dot{\delta} \quad (6.2)$$

$C$  being the viscous damping coefficient. Therefore, an equivalent viscous damping  $C_{eq}$  can be determined in the same way by projecting the measured tangential force  $T$  on the velocity and averaging the projection over one period of oscillation  $\tau$

$$C_{eq} = \frac{\int_{\tau} \langle T, \dot{\delta} \rangle d\delta}{\int_{\tau} \langle \dot{\delta}, \dot{\delta} \rangle d\delta} \quad (6.3)$$

### 6.3.1 Nonlinear SDOF model

To verify the correctness of this above mentioned numerical method, a non linear single degree of freedom system (SDOF) (as shown in Fig. 6.8a ) has been solved using time integration method and its equivalent contact damping and stiffness parameters are computed to get a linearized equivalent system as shown in 6.8b. In the nonlinear system given in Fig. 6.8a, the response of the system was considered to be periodic and a Jenkin contact element [110] loaded with a constant normal force  $N$  was applied. Whereas,  $K_d$ ,  $T$  and  $\mu$  corresponds to the slider contact stiffness, tangential friction force and friction coefficient between the ground and slider, respectively. The system was excited with a set of single harmonic external forces  $f_E(\omega, t)$  and numerically solved over a range of angular frequencies  $\omega$  to find its resonance frequency corresponding to the each excitation force level. Then, the equivalent contact damping and stiffness were computed, at each resonance frequency of the system, according to Eq. 6.3 and 6.1 respectively. In Fig. 6.10 these equivalent contact parameters are plotted as a function of the ratio between the normal load and the excitation force  $N/f_E(\omega, t)$ . In this figure, these parameters

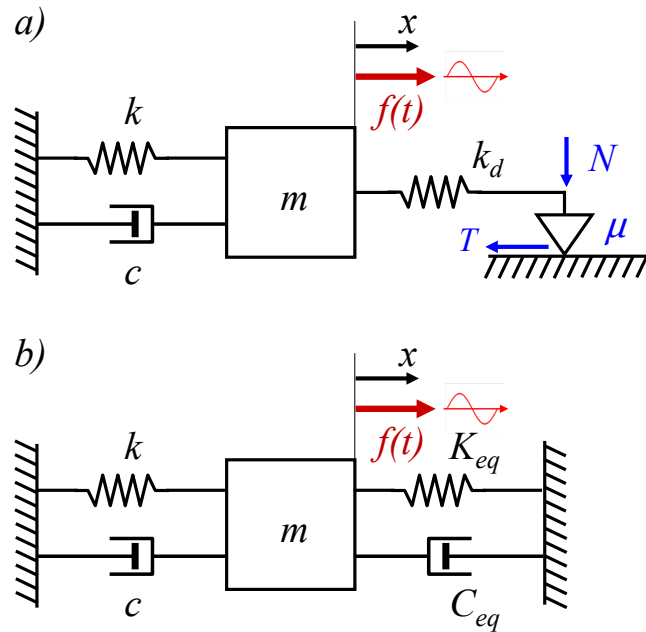


Fig. 6.8 a) Nonlinear single degree of freedom system with Jenkin contact element b) linearized equivalent system with equivalent contact stiffness  $K_{eq}$  and damping  $C_{eq}$

are plotted in a dimensionless form as stiffness ratio ( $K_{eq}/K_d$ ) and damping ratio ( $\zeta_{eq}$ ). A comparison between the response of the nonlinear system and linearized equivalent system is shown in Fig. 6.9. It can be observed that the response of the nonlinear system (shown in Fig. 6.8a) exactly matches with its equivalent linear system (shown in Fig. 6.8b).

As expected, in stick condition the contact behaves as a simple spring with stiffness  $K_d$  and no damping is added to the system (see Fig. 6.10). As the excitation force increases the relative displacements between the mass  $m$  and the contact point increases. When the tangential contact force  $T$  reaches the limiting value  $\mu N$  the contact point starts sliding. The effect of a sliding contact is to reduce the contact stiffness that monotonically decreases to zero for very high excitation force. The equivalent damping shows a different behavior. For small sliding displacement the equivalent damping increases up to a maximum value; then it starts decreasing approaching zero for very high excitation force. This method is exactly similar to the well-known Harmonic Balance Method (as explained in **Chap. 1** Sec. 1.2.1) in which it is assumed that if a periodic solution of a nonlinear system exist, it can

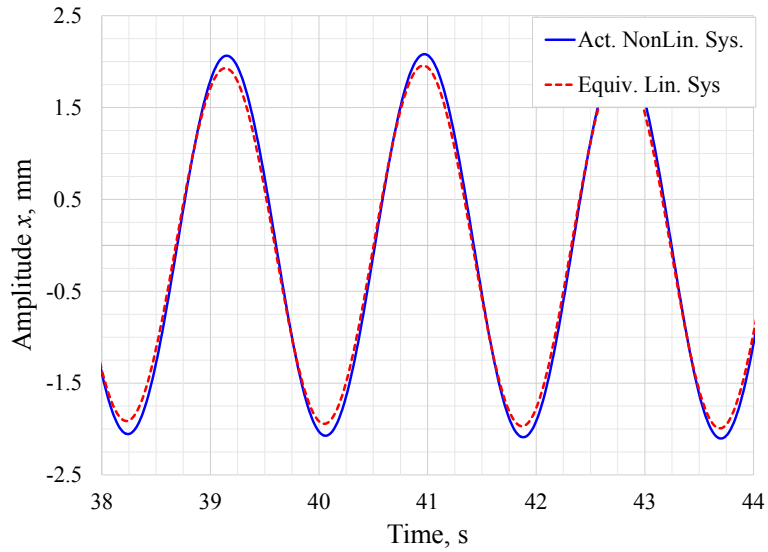


Fig. 6.9 Result comparison between the linear and equivalent nonlinear system

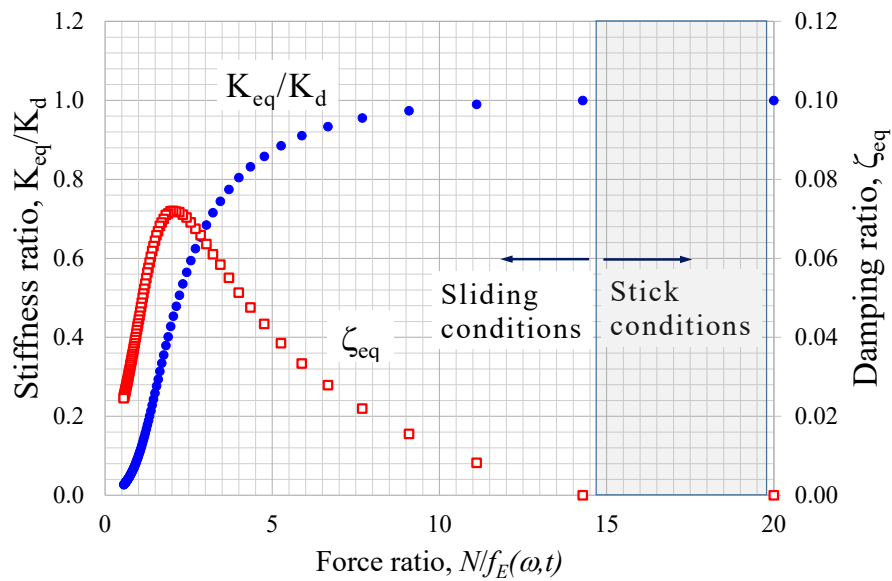


Fig. 6.10 Variations in numerically computed equivalent contact stiffness and damping w.r.t force ratio for the system shown in Fig.6.8 a. In stick region the contact behaves as a simple spring and no additional damping is added to the system.

be represented by a truncated Fourier Series whose coefficient are computed by satisfying the equation of motion of the system.

## 6.4 Novel method to associate the contact parameters with the blade dynamic

In this section, a new methodology has been presented to associate the equivalent contact stiffness and damping with the blade frequency response using damper performance curves i.e. amplitude performance curve and frequency performance curve ( shown in Fig. 6.13 and Fig. 6.14 already described in **Chap. 1** Sec. 1.2.2). An overview of this newly proposed strategy has been shown in Fig.6.11. Initially the FRFs of the blade are measured for a range of blade excitation force at given damper static load level. Then damper contact forces and damper-blade relative displacement were measured close to the each resonance frequency of the blade at corresponding excitation force level and the hysteresis loops are developed from there measured force and displacement(see examples in Fig. 6.15). From these measured blade FRFs and hysteresis loops, the standard damper performance curves and equivalent contact parameters (with the numerical method given in 6.3) are obtained, respectively.

To associate the local/contact behavior of the dampers, the estimated contact parameters i.e. equivalent contact stiffness and damping, are plotted together with the damper performance curves in terms of blade response amplitude and shift in frequency (macro-dynamic behavior), with respect to the force ratio ( $F_C/F_E$ ), as shown in Fig. 6.16 and Fig. 6.18 respectively. These two plots (Fig. 6.16 and Fig. 6.18) facilitate to understand the variation in the frequency response of the blade due to change in the damper contact parameters for a given load condition. Three different levels of the damper static load ( $F_C = 6, 26$  and  $96$  N) are investigated in these experiments. The details about the experimental procedures and the effect of the rigid rotation of the dampers on the equivalent contact parameters are given in **Appendix. D** (Sec.D.1 and Sec.D.2 respectively).

### 6.4.1 Results and observations

The FRFs given in Fig. 6.12 show the frequency response of the blade with and without any damper while the blade was excited with a stepped-sine force signal of  $F_E = 1$  N. From these FRFs the effect of under-platform dampers on the reduction in amplitude response and shift in resonance peak of the blade can easily be observed.

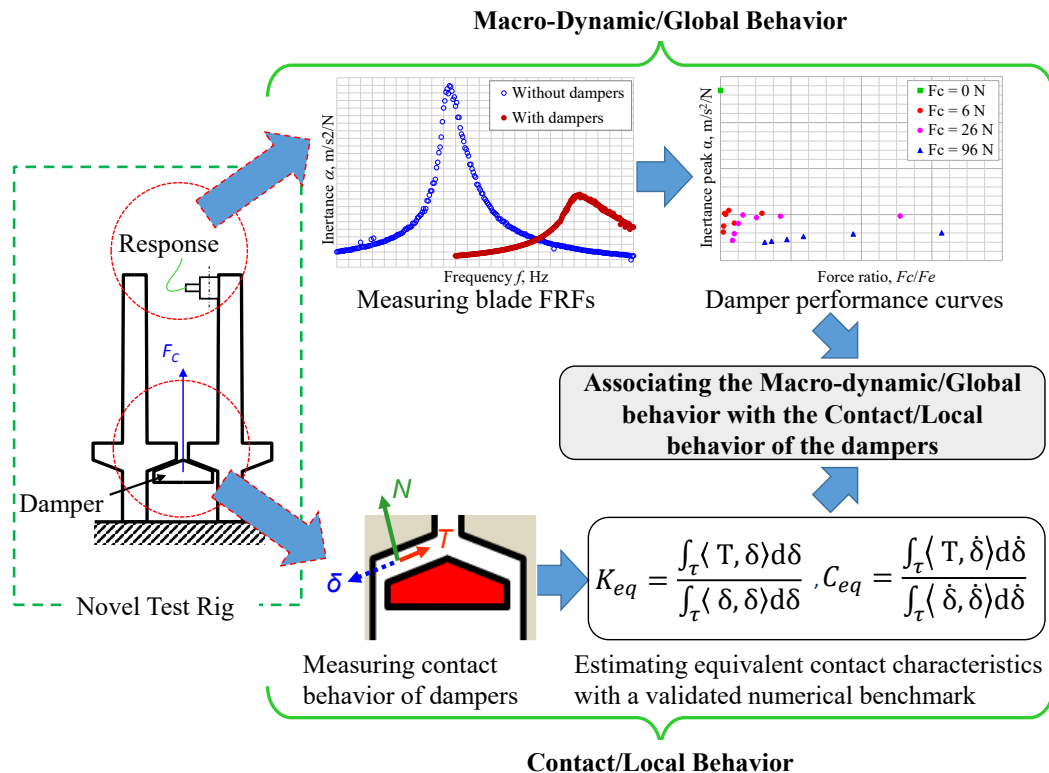


Fig. 6.11 A graphical representation of the strategy to associate the damper contact behavior with the macro-dynamic behavior of the damper-blade system

It can be noticed that higher static loads  $F_C$  on the dampers results in increase of resonance frequency and reduction in response amplitude of the blade for the same excitation force  $F_E$ . This is due to the fact that a higher static load applied on the dampers induces higher normal stiffness at the damper-blade contact. Damper performance curves with respect to inertance peak and blade resonance frequency for all three damper static loads are shown in Fig. 6.13 and 6.14.

In Fig. 6.16, the damper performance in terms of resonance frequency shift are plotted together with the equivalent contact stiffness  $K_{eq}$  for the three damper static load levels  $F_C$ . The resonance frequency and contact stiffness are consistent to each other whereas reduction in stiffness means reduction in resonance frequency. It can be observed that, for all the damper static loads, the resonance frequency of the blade reduces by reducing the force ratio  $F_C/F_E$  or, in other words, by increasing the excitation force. Furthermore, in these results (see Fig. 6.16), it can be seen that the blade resonance frequency is higher at higher static load for the same excitation

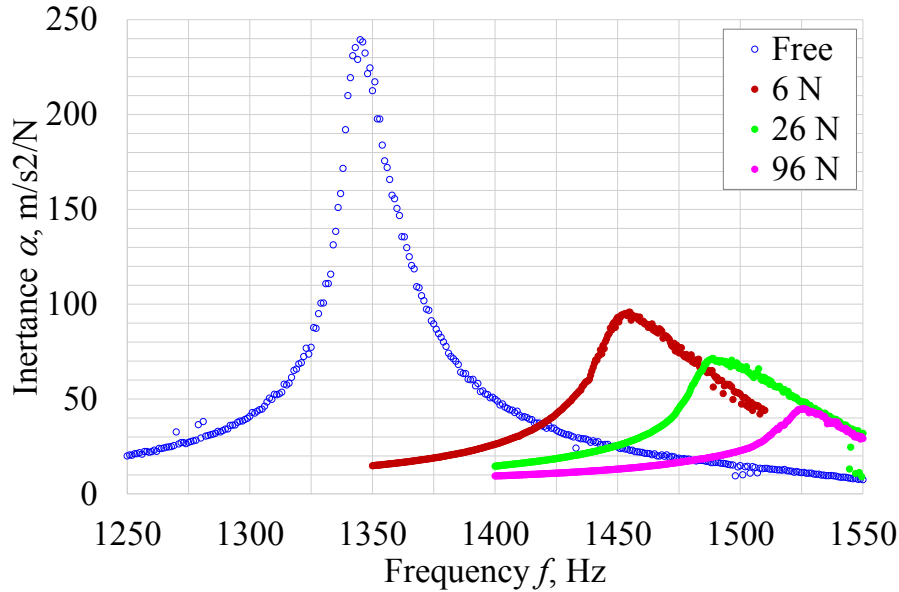


Fig. 6.12 Frequency response of the blade without damper (Free) and with dampers loaded with different static force  $F_C$ . The excitation force  $F_E$  is 1N in all cases.

force levels. The effect of the normal load in shifting the resonance frequency was already underlined in the standard FRFs shown in Fig. 6.12. This phenomenon can be explained by considering that the normal contact stiffness  $K_N$  highly depends on the normal load on the contact surfaces but it does not depend, at least with first-order approximation, on the excitation force. The average estimated values of the equivalent contact stiffness  $K_{eq}$  were 4.7 , 21.7 and 27.8 N/ $\mu\text{m}$  at 6, 26 and 96N damper static load levels respectively. It can also be seen that higher normal static load on the dampers results in higher values of the equivalent contact stiffness. The scatter of all the values of these stiffnesses  $K_{eq}$  for all three damper static load levels are shown in Fig. 6.17.

In Fig. 6.18 the damper performance curve in terms of blade tip acceleration (Inertance) is plotted together with the computed equivalent damping  $C_{eq}$ . By looking at the inertance at  $F_C$  6 and 26 N, it can be observed that reduction in the damping results in increasing the inertance. Whereas, by comparing the results at  $F_C$  26 and 96 N the inertance decreases with decrease in damping. This behavior is fairly expected because the inertance is affected also by the equivalent stiffness  $K_{eq}$  that is monotonically decreasing.

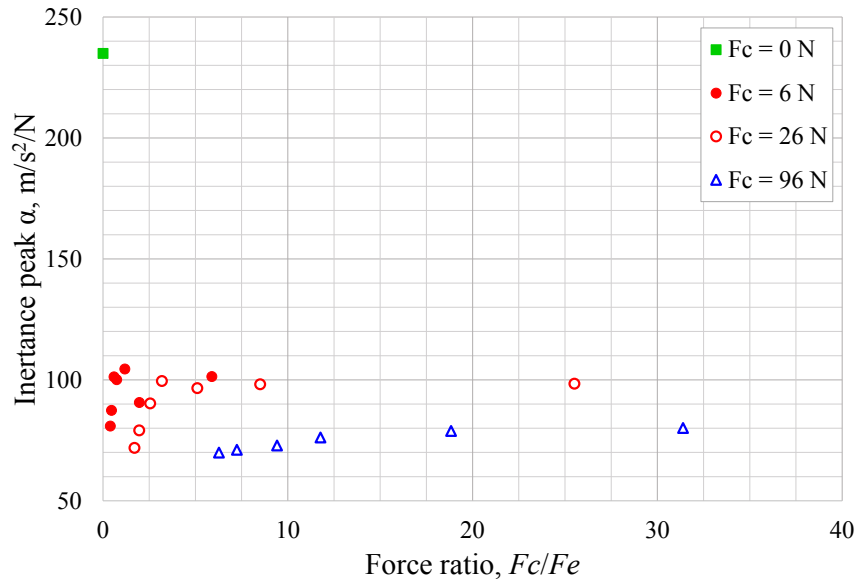


Fig. 6.13 Inertance peak as a function of the force ratio  $F_C/F_E$

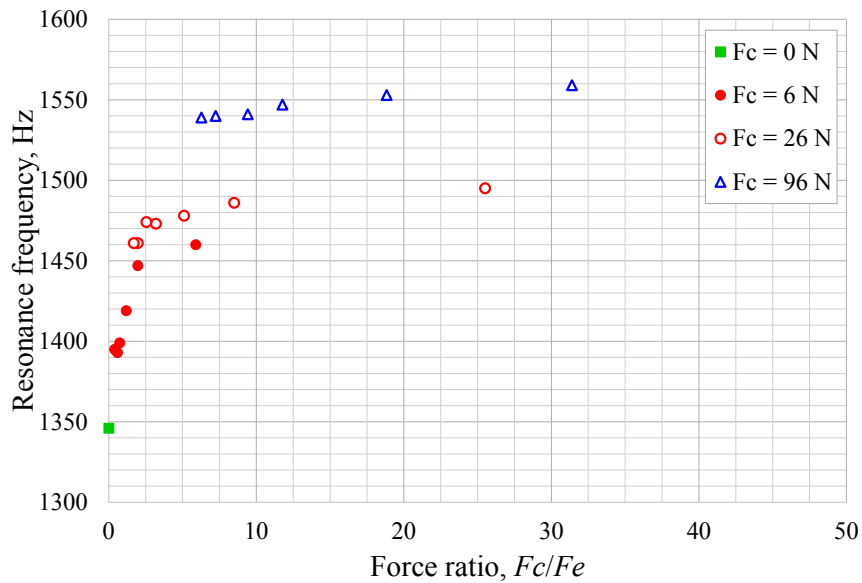


Fig. 6.14 Resonance frequency as a function of the force ratio  $F_C/F_E$

To assist in the analysis of these experimental results the best curve fitting method was applied to these equivalent parameters to show their overall trend. Figures 6.19 and 6.20 show the experimental points and the best fit curves for the equivalent stiffness and damping respectively. In Fig. 6.19, the overall trend of the equivalent tangential contact stiffness indicates that the contact stiffness decreases

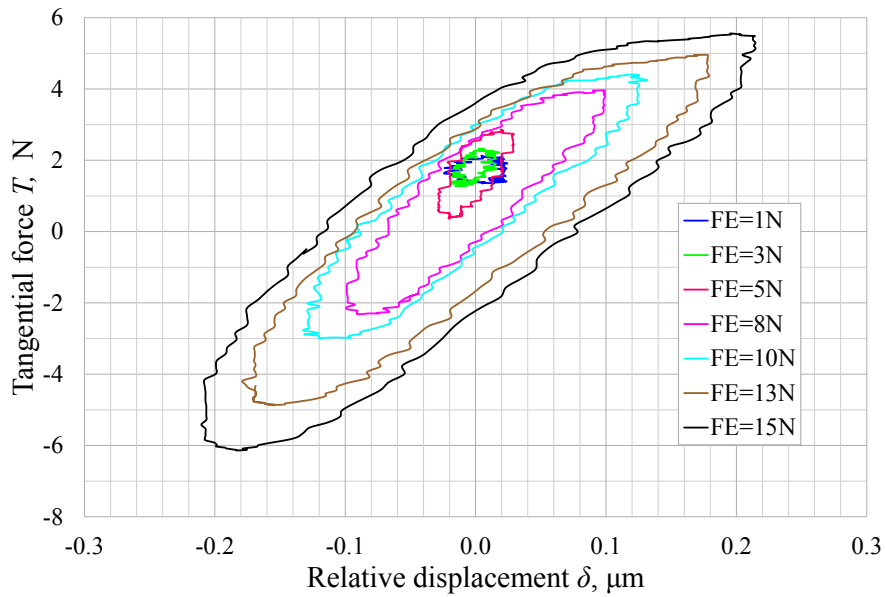


Fig. 6.15 Measured hysteresis loops for different excitation force levels at damper static load  $F_C=96\text{N}$

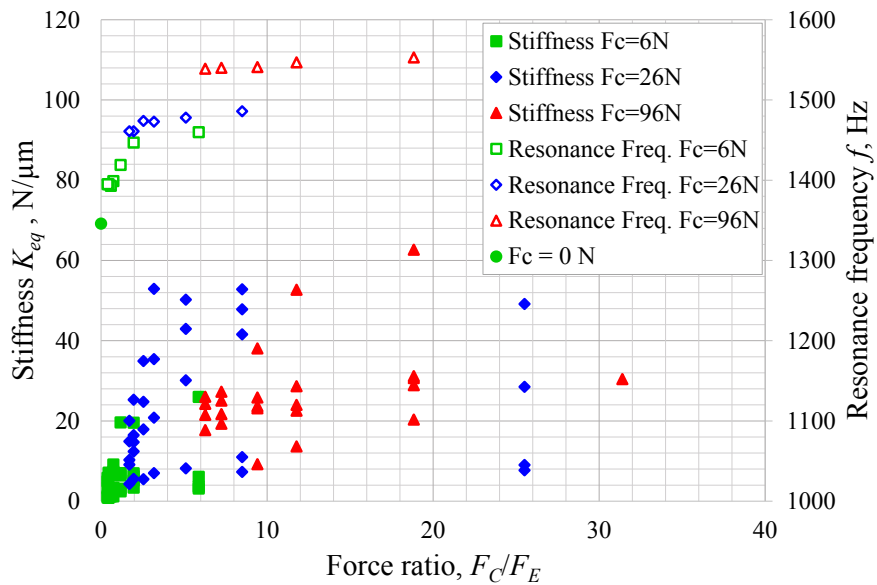


Fig. 6.16 Relationship between resonance frequencies and contact stiffness at different excitation levels and different static load  $F_C$

with increasing the excitation force. The equivalent stiffness shows a monotonic behavior approaching zero at high excitation levels. Fig. 6.20 shows that the equivalent damping is very low for low excitation force i.e. high force ratio  $F_C/F_E$ ,



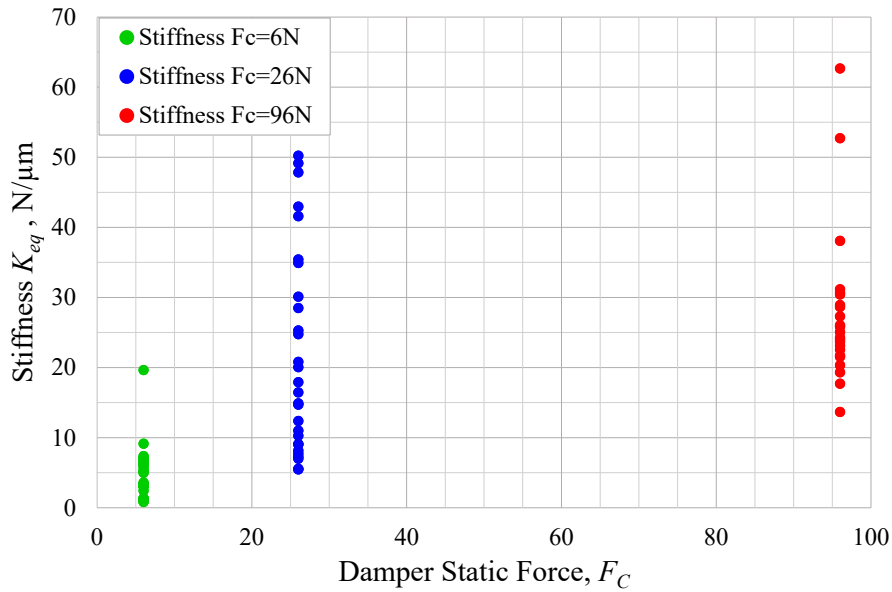


Fig. 6.17 Estimated equivalent contact stiffness  $K_{eq}$  for three damper static load levels  $F_C$

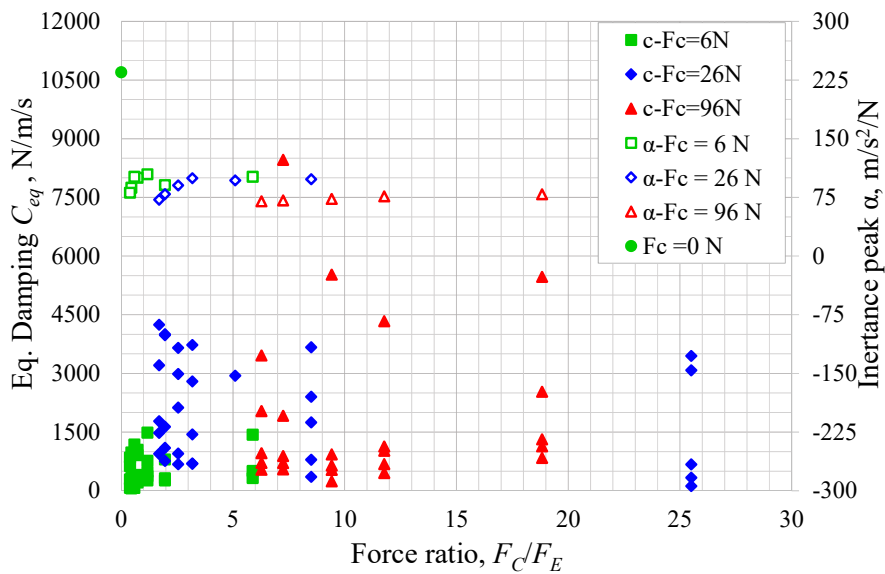


Fig. 6.18 Relationship between blade response amplitude and contact damping at different excitation levels and different static load  $F_C$

for a given damper static normal load. As the excitation force increases the equivalent damping also increases up to a maximum level. With a further increase in excitation

force results in decrease in equivalent damping until it approaches to zero. These experimentally observed behaviors of the equivalent stiffness  $K_{eq}$  and damping  $C_{eq}$  are consistent with the trend numerically computed on the single degree of freedom system as explained in Sec. 6.3.1 and shown in Fig. 6.10.

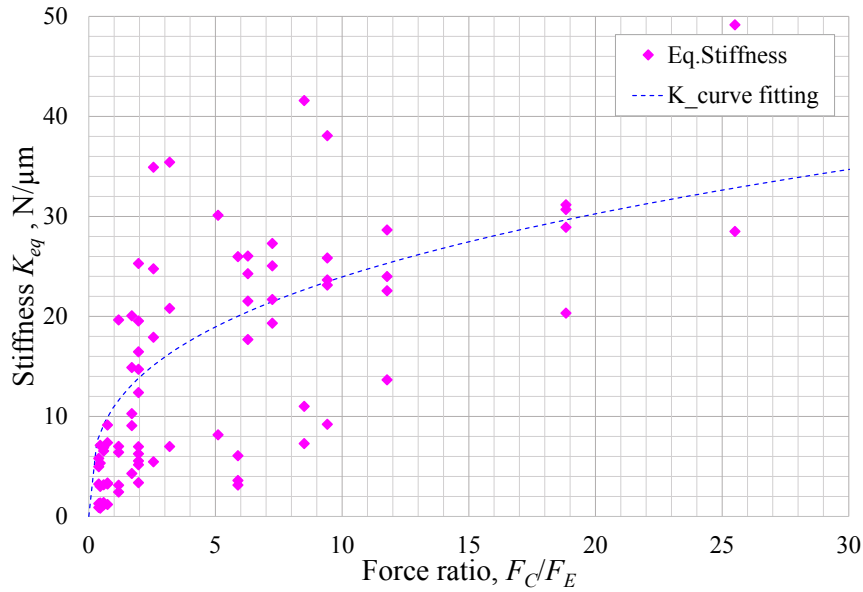


Fig. 6.19 Variations in experimentally measured equivalent contact stiffness w.r.t force ratio, the dotted blue line shows the overall trend of the data obtained by best curve-fit method

## 6.5 Conclusions

The results presented in the first part of this chapter, demonstrate the effect of damper static load on the response amplitude of the blade with a particularly defined damper loading and unloading sequence. It was observed that the static contact forces were always higher in Unloading sequence of the damper than the Loading sequence. This difference in the contact forces resulted in two different frequency response function of the blade due to variations in the damper-blade contact stiffnesses, exclusive obtained from the measured hysteresis loops. A similar numerical study was performed in [60, 111] which also underline the importance of the damper static conditions in the simulation of the blade amplitude response.

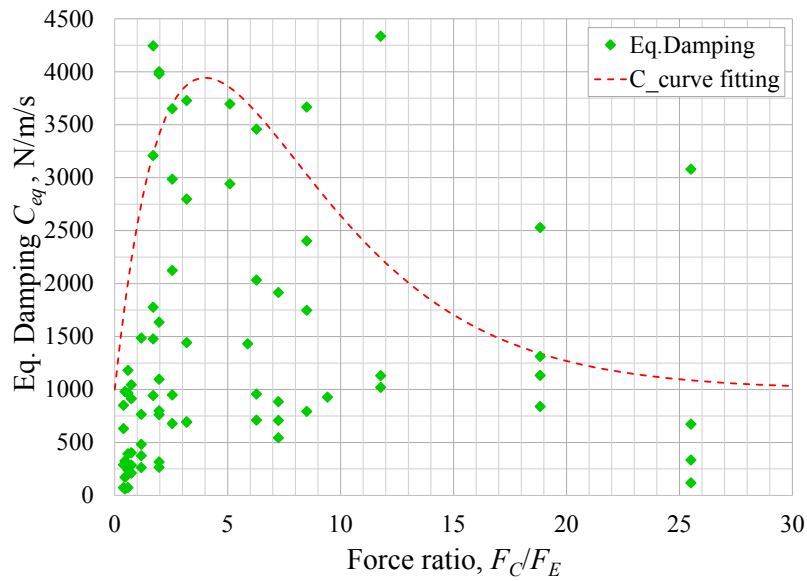


Fig. 6.20 Variations in experimentally measured equivalent contact damping w.r.t force ratio, the dotted red line shows the overall trend of the data obtained by best curve-fit method

In the second part, a numerical method was described to compute the equivalent tangential contact stiffness and damping from the measured hysteresis loops. The adequacy of this method was verified by solving a nonlinear SDOF system to get a linearized equivalent system .

In the final part, first time a method has been introduced to associate the damper local /contact behavior with the dynamic behavior of the blade. In this study, the results show that the contact stiffness decreases with increasing the excitation force or decreasing the static normal load on the damper. This observation is consistent with the measured reduction in resonance frequency of the blade. The equivalent damping increase up to a maximum level and then starts decreasing until approaches to zero for very high excitation force levels. However, the correlation between the equivalent damping and inertance peak is less evident than the effect that the equivalent stiffness has on the frequency shift. These experimental outcomes are in agreement with the theoretical simulations of damper-blade interaction. Further to add that the equivalent damping shows a broad dispersion of the values that highlights the non linear nature of the problem that hinders the measurement repeatability.

# Chapter 7

## Effect of contact force harmonic variation on the blade response

*“Begin at the beginning,” the King said gravely, “and go on till you come to the end: then stop.”*

- Lewis Carroll *Alice in Wonderland*

### 7.1 Introduction

In this investigation, the measured contact forces on the damper-blade system are included as external forces in the numerical model of the blade thus allowing to bypass the cumbersome procedure of computing the approximated nonlinear contact forces for forced response calculations. However, it will be shown that depending on the magnitude of the harmonic variation of the contact forces, the uncertainty level of the forces can restrain to validate the numerically computed FRFs with experimentally measured blade frequency response.

### 7.2 Forced response calculation

In the numerical model of the damper-blade system as described in **Chap. 1** Sec. 1.2.1, the two force vectors  $F_E$  and  $F_{NL}$  on the right side of Eq. 1.1 corresponds to

the externally applied periodic excitation force and nonlinear contact forces. If the damper is not present (i.e. clamped free blade), then  $F_{NL} = 0$ , the force equilibrium is linear and can be solved easily as a system of simple algebraic equation in the frequency domain:

$$\mathbf{Q}^1(t) = (-\omega^2 \mathbf{M} + i\mathbf{C} + \mathbf{K})^{-1} \mathbf{F}_E^1 \quad (7.1)$$

whereas,  $\mathbf{Q}^1(t)$  and  $\mathbf{F}_E^1(t)$  represent the vectors of the first harmonic Fourier components of the displacement and externally applied force with the help of shaker, respectively. If, on the other hand, the dampers are present, contact forces  $F_{NL}$  are non-zero which results from the Coulomb friction nonlinearities. These forces are generally computed with the help of valid contact model (Chap. 1 Sec. 1.2.1). Thanks to the novel test rig, as we can directly measure these contact forces, it is possible to apply these measured contact forces as external forces, on the blade contact nodes, in addition to its general excitation force. So, during experiments the contact forces and external forces are directly measured, decomposed in global coordinates, transformed in the frequency domain using Fourier Transform and then applied to the clamped free blade numerical model (free means without dampers) as shown in Fig. 7.1 and given in Eq. 7.2. Finally, the response of the blade is computed and compared with the experimentally measured blade FRFs for true validation. Mathematically:

$$\mathbf{Q}^1(t) = (-\omega^2 \mathbf{M} + i\mathbf{C} + \mathbf{K})^{-1} (\mathbf{F}_E^1 + \mathbf{F}_{NL,m}^1) \quad (7.2)$$

whereas,  $\mathbf{F}_{NL,m}^1$  corresponds to the first harmonic Fourier components of the measured contact forces. The dependence of the contact forces on relative displacements is still present, in fact different experimental conditions (different  $\omega$ , different excitation levels  $F_E$ ) yield different measured values of  $F_{NL,m}$ . However, no assumption on the formulation of this displacement-contact force relation is needed at this stage.

In this investigation, experiments were performed on the real turbine blade with cylindrical dampers shown in Fig. 6.1. Moreover, the uncertainty level of the contact force measurements is about  $0.75 \div 1\text{N}$ , and cannot be reduced further due to the mechanical tolerances, electronics/signal noise and uncertainty involved in the

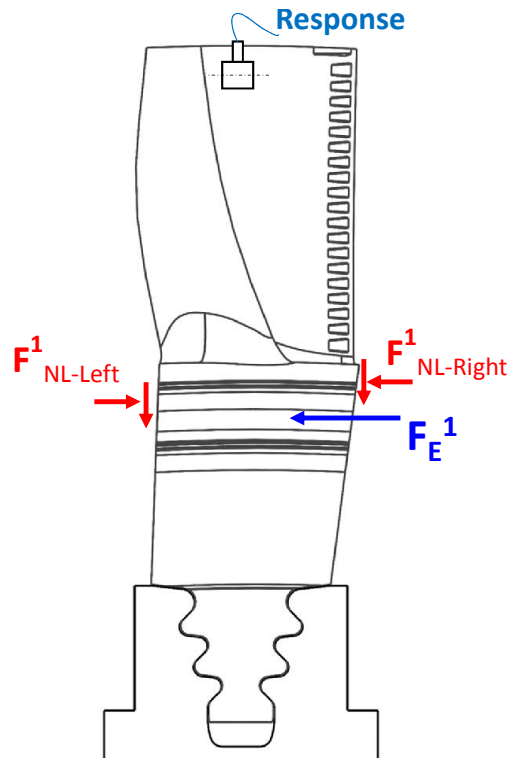


Fig. 7.1 Representation of the measured contact forces  $F_{NL}$  of both side dampers as external forces on the blade along with its general excitation force  $F_E$

estimation of platform angles. For numerical computation, the reduced order linear FE model of the blade (as explained in **Chap. 4** Sec. 4.3 ) has been used

### 7.2.1 Experimental and Numerical blade frequency response comparison

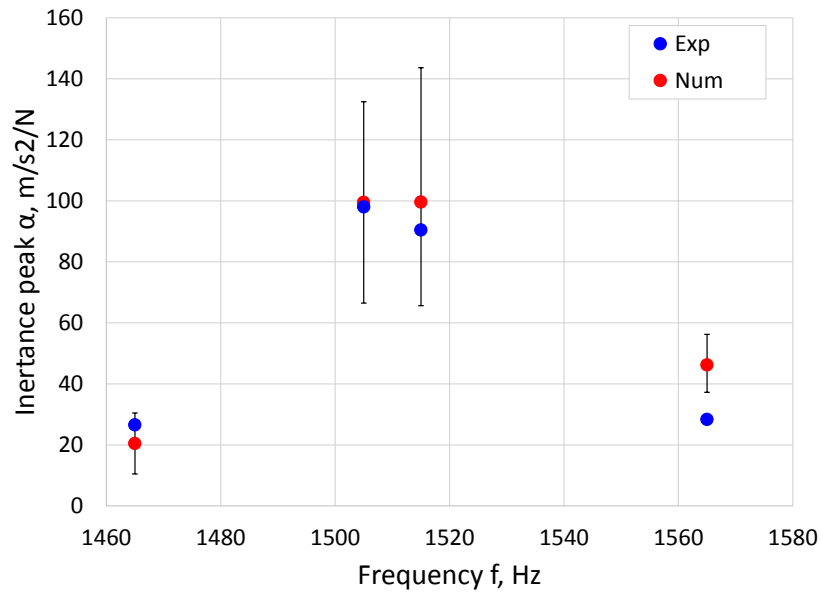
In this study, the contact forces and blade frequency response are obtained from the experimental measurements according to the similar procedure as given in **Appendix. D**. However, this time no relative displacement was measured between the damper-blade contact interface and the blade excitation level  $F_E = 1$  N was applied for all damper static load levels.

### Unsuccessful experimental-numerical comparison

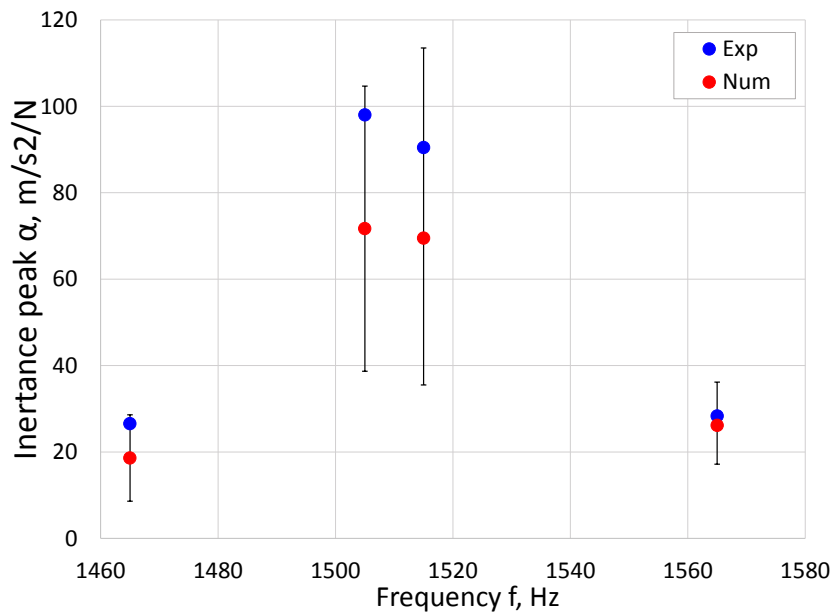
Initially, the contact forces on the both side blade platform (obtained from the contact force measurement as explained in **Chap. 2** Sec. 2.2.5) are applied on their respective side contact nodes along with the shaker excitation force on the blade numerical model (see Fig. 7.1). The blade frequency response is computed at the response node as shown in Fig. 4.8 in **Chap. 2**, and compared with the measured blade response. In the beginning, the numerically computed frequency response of the blade was always found different from the experimental measurements. Experiments were repeated several times at different damper static load levels but every time a significant discrepancy was there between the measured and simulated FRFs. Likewise, it becomes more confusing when dissimilar blade responses were found with substantial differences for repeated experiments at the same loading conditions (whereas, the experimental blade response was identical in those cases). A couple of examples of these incorrect results are shown in Fig. 7.2 in which a considerable difference between the measured and numerically computed amplitude response of the blade can be noticed. It can also be observed that in both examples, the numerical results are quite different from the experimentally measured response as well as from each other also, although the loading conditions in both cases are same.

After carefully going through the blade numerical model again, it has been concluded that the cause of this error does not reside in the model itself, rather in the measured contact force signals fed to the model. Now to identify the error contribution of the contact forces of two dampers individually, two simple and modified test configurations were decided. In each test setup only one side damper was placed on the blade at a time and the contact forces of only that particular damper has been measured and then introduced in the numerical model for validation as shown in as shown in Fig. 7.3.

In the first experiment, only the left side of the blade is considered and after doing all the post-processing of measured forces, the obtained normal and tangential blade contact forces are applied along the *Y-axis* and *Z-axis* on left side of the blade only as shown in Fig. 7.3 a. Similarly, in the second experiment, the odd side damper is placed at its nominal position on the blade only and this time the odd side contact forces are introduced in the numerical model as shown in 7.3 b. The experimental-numerical comparison of the results of both test configurations i.e.



(a)



(b)

Fig. 7.2 (a) Difference between the numerical and experimental results while both dampers are placed,  $F_C = 26\text{N}$ , error example-2. (b) Difference between the numerical and experimental results while both dampers are placed,  $F_C = 26\text{N}$ , error example-2



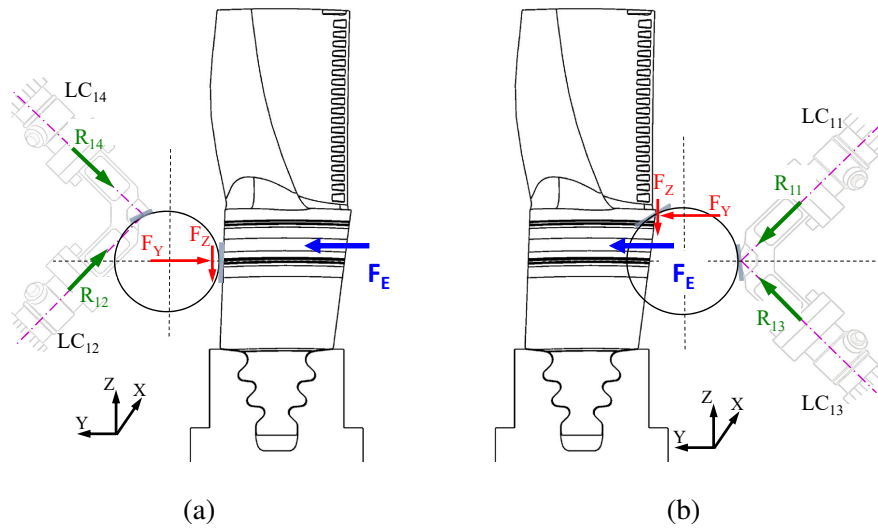


Fig. 7.3 (a) Even side damper placed at its nominal position to measure contact forces. (b) Odd side damper placed at its nominal position to measure contact forces

odd-side damper and even-side damper configuration, are shown in Fig. 7.6 a and 7.4 b, respectively. It can be seen that in the first case of even-side damper, there is still a large discrepancy between the measured FRF and numerical "prediction" as shown in 7.4 a. Whereas, in the case of odd-side damper, numerical results perfectly match with the experimentally measured amplitude response of the blade as shown in 7.4 b.

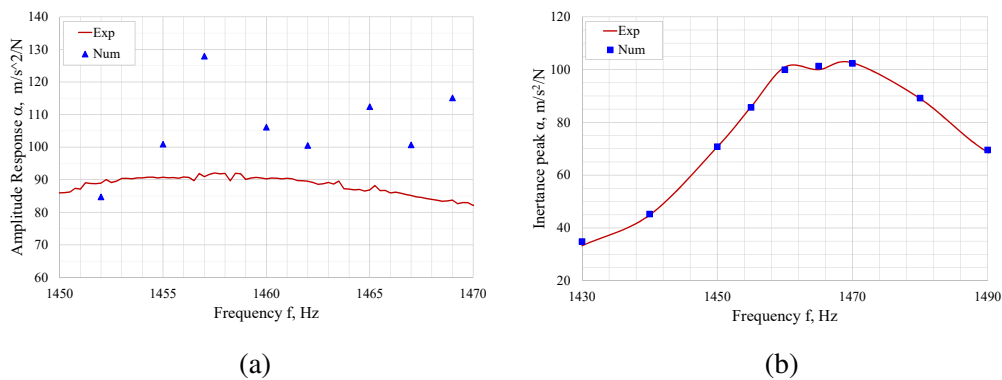


Fig. 7.4 (a) Numerical and experimental result for test configuration-1 with even side dampers only (b) Numerical and experimental result for test configuration-2 with even side dampers only.

After closely observing the measured damper contact forces in both test cases, it has been found that the harmonic variation of the even side contact force components ranges between 1 to 2N at most (see also Fig. 7.5 a) at the given excitation force level. Whereas, in case of odd side damper, this harmonic variation of the contact forces ranged between 5 to 8N (Fig. 7.5 b). Although the values of static components of these forces was found always higher than 15N in both cases (even and odd). Whereas, the magnitude of the harmonic variation of the force depends upon the contact angles of the corresponding blade side and the platform kinematics (i.e. blade mode shape and experimental set-up). So, in case of even side, the level of uncertainty on the contact force signals ( $\approx 0.75$  N) is of the same order of magnitude as the signal itself and this easily explains the very large discrepancies between numerical and experimental results for first test configuration.

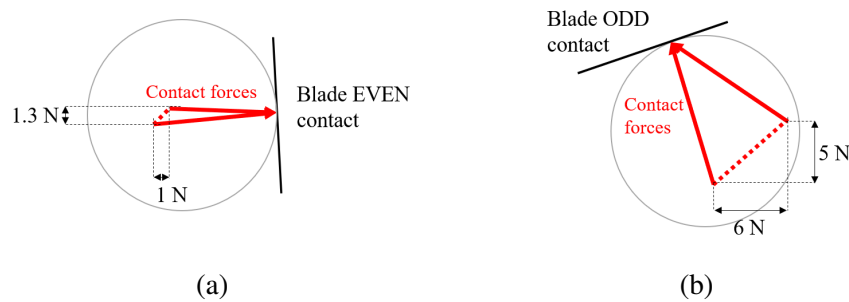


Fig. 7.5 (a) Typical contact forces harmonic variation when only the "even" side damper is present. (b) Typical contact forces harmonic variation when only the "odd" side damper is present.

### Error sensitivity analysis

To evaluate further the effect of the force measurement error on the blade response amplitude, a sensitivity analysis has been performed. A small sinusoidal force error has been added "numerically" to the measured force signals. The amplitude of this error was set equal to the contact forces uncertainty level (0.75 N) with a small phase shift varying from 0 to 15 degrees with respect to the measured contact force signals. This sensitivity analysis is performed for a single experimental condition, i.e. centrifugal load on the damper  $F_C = 26$  N and excitation force  $F_E = 1$ . The maximum and minimum values of the blade response produced by the perturbed contact force signals are shown in Fig. 7.6 a. These maximum and minimum limits

(green lines) depict that any value of the blade response can be found between these two limits with such a small error in the contact forces.

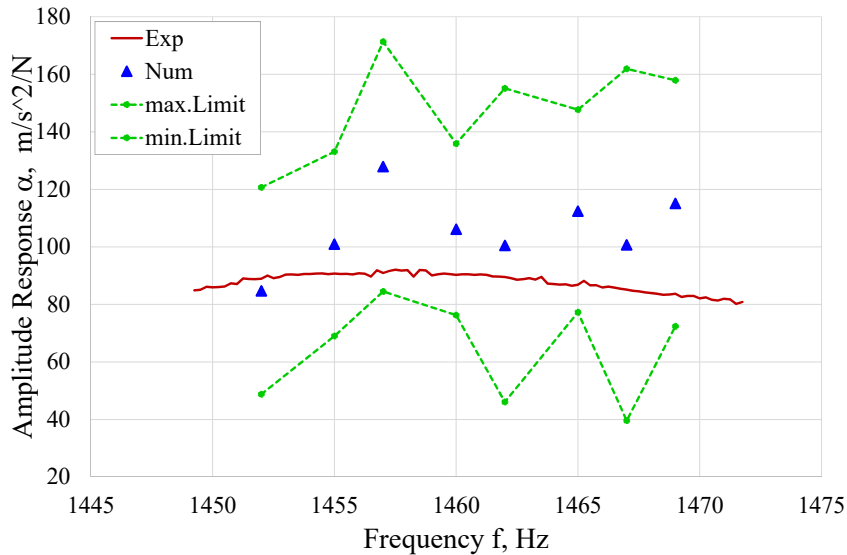


Fig. 7.6 Error sensitivity of blade response amplitude while applying only even side contact forces measurement at  $F_C = 26$  N

### Successful experimental-numerical comparison

The experimental set-up shown in Fig. 7.3 b, thanks to a different combination of choice of contact angles and platform kinematics, produces:

- higher harmonic variation of the measured contact forces (in this case recorded at the load cells  $LC_{11}$  and  $LC_{13}$ ), now ranging between 5 and 8 N (see also Fig. 7.5 b);
- increased stiffening effect, as shown in Fig.7.6 b, the peak for  $F_C=26$  N is now sharper and few Hz higher than that shown in Fig. 7.6 a.

Furthermore, in this case, the uncertainty level guaranteed by the load cell measurement is adequate (reasonably smaller than the force signals themselves). Conse-

quently, the validation procedure summarized in Eq. 7.2 can be safely applied. To further confirm these findings, this second test configuration of odd-side damper (see Fig. 7.3 b) was investigated for three different damper static load level  $F_C = 26, 46$  and  $86\text{N}$ . The final results of the experimental-numerical comparisons for all three levels of static load on the damper, are shown in Fig. 7.7, 7.8 and 7.9. It can be seen that the numerical results match their experimental counterpart quite reasonably for all the three investigated cases.

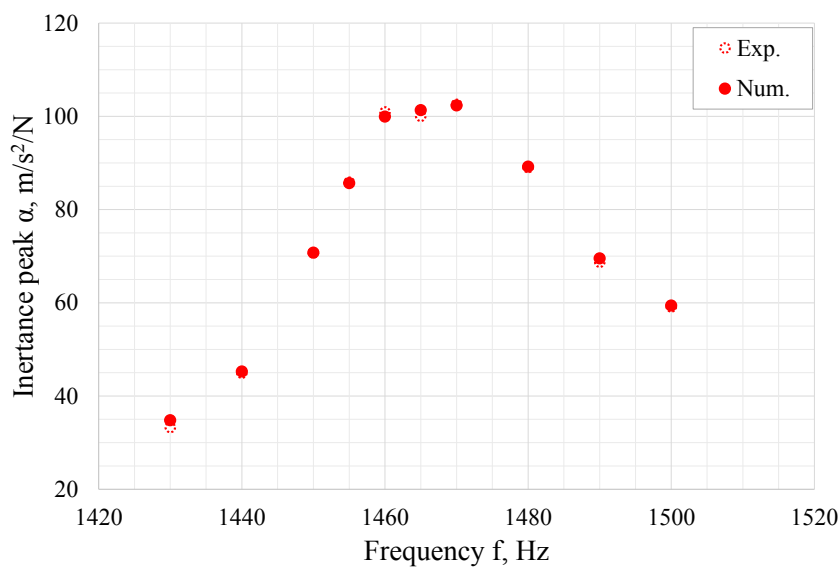


Fig. 7.7 Comparison of numerical and experiment results for a static damper centrifugal load values  $F_C = 26\text{ N}$

## 7.3 Conclusions

The main argument that was addressed in this chapter is: ‘if the linear numerical model of the blade is fed with the measured contact forces as external forces on the blade contact nodes, is it possible to validate the numerically computed response of the blade with the experimentally observed?’. The answer to this question was found, Yes. However, the limitations of this approach due to insufficient resolution

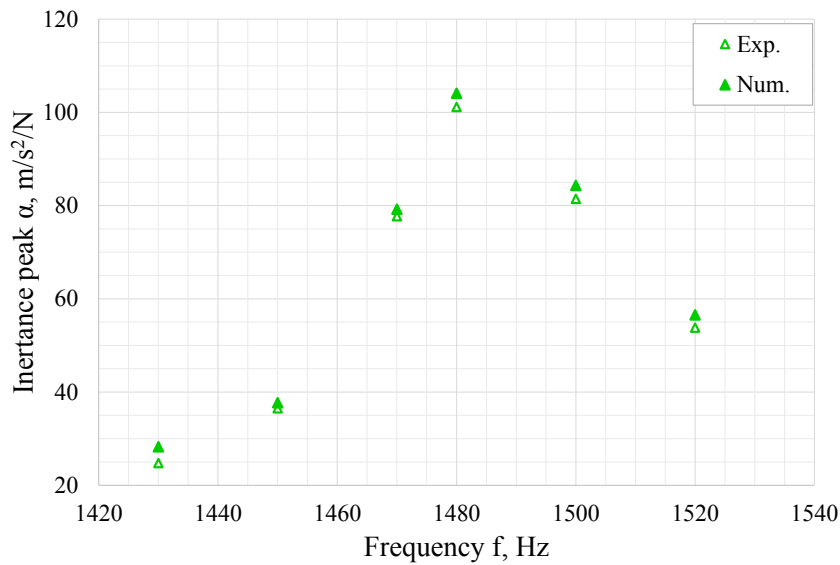


Fig. 7.8 Comparison of numerical and experiment results for a static damper centrifugal load values  $F_C = 46$  N

of the contact force signals for the given damper configurations are highlighted as an important warning for the experimenters. This method facilitates to avoid the complicated procedure of computing the approximated nonlinear contact forces. However, it has been found that the particular contact geometry of the damper-blade interface (very steep angles along the surface) results in very small harmonic variation (close to the force measurement resolution) in the measured contact forces. Therefore, while applying this method, it is important to verify that the dynamic contact force components are large enough, for the contact geometry under investigation, than the overall force measurement resolution .

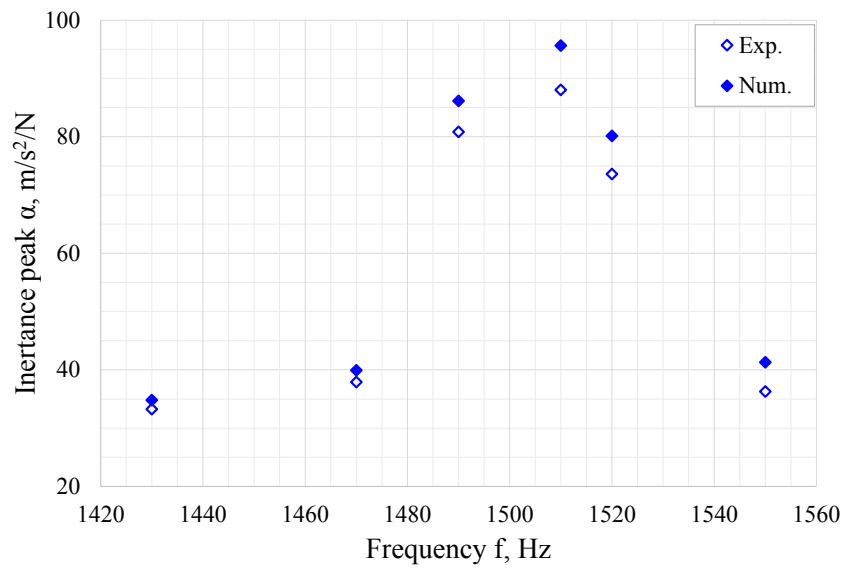


Fig. 7.9 Comparison of numerical and experiment results for a static damper centrifugal load values  $F_C = 86 \text{ N}$

# Chapter 8

## Conclusions

*"Problems worthy of attack, prove their worth by hitting back."*

- Piet Hein

The overall outcomes of this thesis are summarized as follows:

### 8.1 Conclusions on the Test Rig capabilities

In this thesis, a novel test rig has been designed which is first of its kind that directly measures, in addition to the standard blade FRFs, the damper contact forces and relative displacement between the damper and respective platform (blade or fixed platform). Therefore, it is possible to produce the contact hysteresis loops, force equilibrium and platform kinematics for each point on a FRF. This set of diagrams is particularly helpful in explaining the unexpected phenomena (e.g. FRFs lack of repeatability, unprecedented trend of the FRFs etc..) which often make experimental characterization of damper-blade systems difficult.

Furthermore, this newly developed test setup includes a distinct blade clamp mechanism in which it is possible to regulate and measure the clamping force applied at the bottom of the blade root. This clamping force in form of pushing force simulates the actual centrifugal clamping force experienced by the blade while the turbine runs. The clamp has capability to apply up to 300KN force on the blade

which makes it possible to separate the effect or contribution of blade root damping from the under-platform damping contributions up to the required level of accuracy. Moreover, due to the presence of strain gauge based load cell in the clamp mechanism, it is possible to measure and control the applied clamping force on the blade. This feature of the rig facilitates to investigate the damping contributions of the blade root at various clamping force levels. In addition to this, use of replaceable clamp adapter and ground or blade platforms/pads makes it possible to test more than one blade and dampers with a minor modification in the setup.

Two turbine blades (dummy and a real turbine blade) are investigated with their set of under-platform dampers are investigated numerically and experimentally during this study. The outcomes of the investigation of the corresponding damper-blade combination are encapsulated separately in the proceeding sections.

## 8.2 Linear Numerical Blade models

In this part of the thesis, the procedure to obtain the linear finite element model of the both blades (dummy and real blade) is described. As the focus of this study is only on the under-platform dampers, a very high clamping force was applied on both blades to avoid any damping contribution from their roots during testing. Moreover, in case of dummy blade, a commonly used method of fully constraining the randomly selected root nodes was adapted to match the linear numerical and experimental dynamic response of the blade without dampers.

Although this fixed node method somehow serves the purpose (for dummy blade, the experimental results match successfully with the numerical simulation) but due to over-approximation and difficulty to match the higher blade frequencies, an alternative method has been proposed for the second blade. So, for real blade, a method of attaching the 3D spring element to the blade root and corresponding structure (with the ground/clamp in our case) was introduced. These 3D spring elements are parameterized to match the numerical and experimental response of the blade. Finally, the Hurty/Craig-Bampton model order reduction technique is applied on both blade full FE model to reduce their size without losing the accuracy.



### **8.3 Dummy Blade investigation**

In this part of the thesis, two semi-cylindrical dampers were studied experimentally and numerically in combination with the newly designed dummy blade. A dummy blade i.e. much simple and symmetric than real blade, was also purposely developed during this thesis to extend the experimental investigation of the dampers contact kinematics which were not possible on the real blade due to its complex geometry and contact angles.

#### **Conclusions on blade-platform kinematics**

In this study, it was found that the blade-platform motion can strongly influence the damper performance. A numerical technique i.e. instantaneous center of rotation (ICR), was introduced to reconstructed the blade platforms motion. Through this technique, it was found in the investigated case that the platform motion is almost orthogonal to the flat-on-flat interface, which, as a result, fails to reach the gross slip condition. This hypothesis was confirmed by the measured hysteresis loops and also by the results obtained through a numerical model of the damper-blade system.

#### **Conclusions on measured contact parameters**

From the measured data on novel test rig, friction contact parameters (tangential contact stiffness and friction coefficient) were estimated, which compare extremely well with the values found for the same damper on a different test rig. These findings speak for the soundness of both test rigs and for the contact parameter estimation procedure. In these results, it was observed that neither the frequency nor the platform kinematics (amplitude and direction) influences friction parameters.

#### **Conclusions on damper-blade numerical model simulation**

The measured contact parameters are fed to a numerical model representing the semi-cylindrical damper placed between two platforms. Measured and simulated results were compared only “a-posteriori” for a true validation.

## 8.4 Real Turbine Blade investigation

In this part of the thesis work, a real turbine blade with two cylindrical dampers was studied to investigate the damper performance and their contact behavior. A combination of numerical and experimental investigation on this second damper-blade combination leads to the following conclusions:

### **Conclusions on the effect of damper static load**

During this experimental investigation, it was found that the different static load conditions of the dampers (changing the damper loading/unloading sequence) can lead to the different frequency response of the blade even if the same damper-static load is applied. Exactly same results were found in [60] in which damper-blade system is studied numerically to get its forced response calculation. This effect of static forces was verified by the estimated contact stiffness from the measured hysteresis loops. Moreover, a best fitting curve procedure was also applied on the frequency response of the blade to identify the modal parameters and it has been determined that the modal stiffness is always higher in case of higher static contact force measurements. From these findings, it can be concluded that a slight change in contact condition, e.g. changing the damper loading sequence, can result in different response functions of the blade/damper systems at the same static load levels on the dampers.

### **Conclusions on equivalent contact stiffness and damping estimation**

It is possible to estimate accurately the equivalent contact stiffness and damping of the damper using measured hysteresis on the rig. A numerical method has been explained to extract these equivalent parameters. Moreover, the adequacy of this method was verified by replacing the nonlinear Jenkin contact element with these equivalent parameters in a 1DOFs nonlinear system. To confirm the correctness of this method the response of the nonlinear system, solved with the help of time integration, is compared with linearized system response.

### **Conclusions on associating the damper Local/Contact behavior with Macro-dynamic behavior**

For the first time the dynamic response of the blade, called Macro Dynamic behavior, is related with the equivalent contact parameters of the damper-blade contact interfaces, called contact/local behavior. It has been found that the damper performance curves can be used together the equivalent contact parameters to link the blade frequency and amplitude variation with the variation in equivalent contact stiffness and damping.

### **Conclusions on the contact forces as external forces**

In this investigation, a validated numerical model of the blade is provided by introducing the contact forces as external forces and numerical results are compared with experimentally measured FRFs. Thanks to the novel test rig, the contact forces are measured directly and the cumbersome steps for the estimation of nonlinear contact forces, with the help of suitable contact model, were surpassed. These contact forces are decomposed into normal and tangential direction of the contact and included in the numerical model of the blade with a correct amplitude and phase as external forces on the respect contact nodes of the damper-blade contact interface in addition to the general blade excitation force. These contact forces were transferred from the time domain to the frequency domain with the help of Fourier Transform and added in the force vector of the blade numerical model to solve its system of equations.

In this study, it was worth noticing that the measured contact forces can be introduced as external forces only if the harmonic variation of the force is considerably large enough with compare to overall resolution of the contact force measurement system. Moreover, the harmonic variation of the contact forces, along with the other parameters, highly depends upon the contact geometry of the damper and blade interface.

## 8.5 Future Work

The focus of this work was only on the under-platform dampers and any damping contribution of the blade root were separated by applying very high clamping force. However, in reality these damping contribution of the blade roots are also present depending upon the shape, centrifugal force acting on the blade root and root/bucket contact conditions. Therefore, a possible area to further extend this work can be including the damping contribution of the roots in the blade along with under-platform dampers contribution. From the experimental point of view, thanks to the novel test rig that it is possible to change the blade adapter and apply a controlled clamping force on the blade. This feature of the test rig can be further explored and an in-depth experimental observations can be gathered for the different blade root geometries at different clamping force levels to support the numerical simulation. Similarly, the suggested numerical method of applying the 3D contact spring at the root of the blade can be extended by replacing these springs with the standard contact elements in the numerical model of the blade.

Moreover, the method of estimating the equivalent damping and stiffness from the measured hysteresis loops can be further extended to an actual damper-blade system. The contacts between the damper and blade can be modeled with these equivalent contact stiffness and damping parameters and an approximated linearized system damper-blade system can be obtained. Finally, the numerical response of this equivalent system can be validated with its experimental counter-part.

## Publications

- D. Botto, and **M. Umer**, A novel test rig to investigate under-platform damper dynamics, *Mechanical Systems and Signal Processing*, Volume 100, 2018, Pages 344-359, ISSN 0888-3270, <http://dx.doi.org/10.1016/j.ymssp.2017.07.046>
- D. Botto, **M. Umer**, C. Gastaldi, and MM. Gola, An experimental investigation of the dynamics of a blade with two under-platform dampers. In: *Journal of Engineering for Gas Turbines and Power*. - ISSN 0742-4795. doi: 10.1115/1.4037865
- **M. Umer**, D. Botto, C. Gastaldi, and MM. Gola, Experimental study of under-platform damper kinematics in presence of blade dynamics. In: *IOP Conference Series: Materials Science and Engineering*, Volume 302 doi: 10.1088/1757-899X/302/1/012016
- D. Botto, **M. Umer**, C. Gastaldi, MM. Gola, An Experimental Investigation of the Dynamic of a Blade With Two Under-Platform Dampers. *ASME. Turbo Expo: Power for Land, Sea, and Air, Volume 7B: Structures and Dynamics V07BT35A029*. doi:10.1115/GT2017-64928.
- **M. Umer**, C. Gastaldi and D. Botto, The effect of friction damping on the dynamic response of vibrating structures: an insight into model validation . *ISMA. International Conference on Noise and Vibration Engineering*. ISBN:978-907380299-5, 2018, Leuven, Belgium.
- **M. Umer** and D. Botto, Measurement of contact parameters on under-platform dampers coupled with blade dynamics, *International Journal of Mechanical Sciences*. 2019 (Under-review)
- **M. Umer**, D. Botto, and S. Zucca, Effect of variation in contact friction on the performance of the under-platform dampers, *International Congress on Sound and Vibration(ICSV26) 2019, Montréal, Canada (Accepted)*

# Bibliography

- [1] M. M. Gola, M. Braga, and T. Liu. Design of a new test rig to evaluate underplatform damper performance. In *ASME 2010 10th Biennial Conference on Engineering Systems Design and Analysis*, pages 85–94. ASME, 2010.
- [2] R. Schafrik and R. Sprague. Gas turbine materials. *Adv. Mater. Process*, 5:29–34, 2004.
- [3] Geoffrey W Meetham. *The development of gas turbine materials*. Springer Science & Business Media, 2012.
- [4] EP Petrov and DJ Ewins. State-of-the-art dynamic analysis for non-linear gas turbine structures. *Proceedings of the Institution of Mechanical Engineers, Part G: Journal of Aerospace Engineering*, 218(3):199–211, 2004.
- [5] B. A. Cowles. High cycle fatigue in aircraft gas turbines—an industry perspective. *International Journal of Fracture*, 80(2-3):147–163, 1996.
- [6] J. Hou, B. J. Wicks, and R. A. Antoniou. An investigation of fatigue failures of turbine blades in a gas turbine engine by mechanical analysis. *Engineering Failure Analysis*, 9(2):201–211, 2002.
- [7] Australian Transportation Safety Board (ATSB). In-flight engine malfunction – 100 km south-east of bali international airport, indonesia – 9 may 2011, vh-ogh, boeing co 747-438. techreport ISBN 978-1-74251-304-1, Australian Transport Safety Bureau, 2012.
- [8] Jeff Green. *Controlling forced response of a high pressure turbine blade*. PhD thesis, KTH, 2006.
- [9] A. V. Srinivasan. Flutter and resonant vibration characteristics of engine blades. *Journal of engineering for gas turbines and power*, 119(4):742–775, 1997.
- [10] J. H. Griffin. Friction damping of resonant stresses in gas turbine engine airfoils. *Journal of Engineering for Power*, 102(2):329–333, 1980.
- [11] C. M. Firrone and I. Bertino. Experimental investigation on the damping effectiveness of blade root joints. *Experimental Mechanics*, 55:981–988, 2015.

- [12] I. A. Sever. *Experimental validation of turbomachinery blade vibration predictions*. PhD thesis, Imperial College London (University of London), 2004.
- [13] Kenan Y Sanliturk, David J Ewins, and Anthony B Stanbridge. Underplatform dampers for turbine blades: theoretical modelling, analysis and comparison with experimental data. In *ASME 1999 international gas turbine and aeroengine congress and exhibition*, pages V004T03A037–V004T03A037. American Society of Mechanical Engineers, 1999.
- [14] J. Szwedowicz. Bladed disks: non linear dynamics. *Structural design of aircraft engines: key objectives and techniques*, 2008.
- [15] J. H. Griffin. A review of friction damping of turbine blade vibration. *International Journal of Turbo and Jet Engines*, 7(3-4):297–308, 1990.
- [16] B. Shorr, N. Serebriakov, G. Mel’nikova, Dmitri S., B. Vasilyev, and A. Stadnikov. Numerical and experimental estimation of the turbine blade damper efficiency. In *ASME Turbo Expo 2018: Turbomachinery Technical Conference and Exposition*, pages V07CT35A040–V07CT35A040. American Society of Mechanical Engineers, 2018.
- [17] J. Szwedowicz. Bladed disks: Non linear dynamics. *Structural Design of Aircraft Engines: Key Objectives and Techniques; Seinturier, E., Paniagua, G., Eds*, 2008.
- [18] M. Krack, L. Salles, and F. Thouverez. Vibration prediction of bladed disks coupled by friction joints. *Archives of Computational Methods in Engineering*, 24(3):589–636, 2017.
- [19] J. Awrejcewicz and Y. Pyr’yev. *Nonsmooth dynamics of contacting thermoelastic bodies*, volume 16. Springer Science & Business Media, 2008.
- [20] M. M. Gola and T. Liu. A direct experimental–numerical method for investigations of a laboratory under-platform damper behavior. *International Journal of Solids and Structures*, 51(25-26):4245–4259, 2014.
- [21] L. Panning, W. Sextro, and K. Popp. Spatial dynamics of tuned and mistuned bladed disks with cylindrical and wedge-shaped friction dampers. *International Journal of Rotating Machinery*, 9(3):219–228, 2003.
- [22] S. Firrone, C. M. and Zucca. Modelling friction contacts in structural dynamics and its application to turbine bladed disks. In *Numerical Analysis-Theory and Application*. InTech, 2011.
- [23] L. Panning, K. Popp, W. Sextro, F. Gotting, A. Kayser, and I. Wolter. Asymmetrical underplatform dampers in gas turbine bladings: theory and application. In *ASME Turbo Expo 2004: Power for Land, Sea, and Air*, pages 269–280. American Society of Mechanical Engineers, 2004.

- [24] M. M. Gastaldi, C. and Gola. On the relevance of a microslip contact model for under-platform dampers. *International Journal of Mechanical Sciences*, 115:145–156, 2016.
- [25] C. Gastaldi and M. M. Gola. Pre-optimization of asymmetrical underplatform dampers. *Journal of Engineering for Gas Turbines and Power*, 139(1):012504, 2017.
- [26] M. M. Gola and C. Gastaldi. Understanding complexities in underplatform damper mechanics. In *ASME Turbo Expo 2014: Turbine Technical Conference and Exposition*, pages V07AT34A002–V07AT34A002. American Society of Mechanical Engineers, 2014.
- [27] C. Gastaldi, M. M Gola, et al. Estimation accuracy vs. engineering significance of contact parameters for solid dampers. *Journal of the Global Power and Propulsion Society*, 1:VLXC9F, 2017.
- [28] E. P. Petrov. Explicit finite element models of friction dampers in forced response analysis of bladed disks. *Journal of engineering for gas turbines and power*, 130(2):022502, 2008.
- [29] S. Nacivet, C. Pierre, F. Thouverez, and L. Jezequel. A dynamic lagrangian frequency–time method for the vibration of dry-friction-damped systems. *Journal of Sound and Vibration*, 265(1):201–219, 2003.
- [30] M. Herzog, A. and Krack, Panning L., and J. Wallaschek. Comparison of two widely-used frequency-time domain contact models for the vibration simulation of shrouded turbine blades. In *ASME Turbo Expo 2014: Turbine Technical Conference and Exposition*, pages V07BT33A018–V07BT33A018. American Society of Mechanical Engineers, 2014.
- [31] Alberto Luiz Serpa and Fernando Iguti. Contact with friction using the augmented lagrangian method: a conditional constrained minimization problem. *Journal of the Brazilian Society of Mechanical Sciences*, 22(2):273–289, 2000.
- [32] M. Mitra, S. Zucca, and B. I. Epureanu. Adaptive microslip projection for reduction of frictional and contact nonlinearities in shrouded blisks. *Journal of Computational and Nonlinear Dynamics*, 11(4):041016, 2016.
- [33] E. Cigeroglu, N. An, and C. H. Menq. A microslip friction model with normal load variation induced by normal motion. *Nonlinear Dynamics*, 50(3):609, 2007.
- [34] C. W. Schwingshackl, E. P. Petrov, and D. J. Ewins. Effects of contact interface parameters on vibration of turbine bladed disks with underplatform dampers. *Journal of Engineering for Gas Turbines and Power*, 134(3):032507, 2012.
- [35] J. Szwedowicz, M. Kissel, B. Ravindra, and R. Kellerer. Estimation of contact stiffness and its role in the design of a friction damper. In *ASME Turbo Expo 2001: Power for Land, Sea, and Air*, pages V004T03A049–V004T03A049. American Society of Mechanical Engineers, 2001.



- [36] C. Gastaldi, T. M. Grossi, E. and Berruti, et al. On the choice of contact parameters for the forced response calculation of a bladed disk with underplatform dampers. *Journal of the Global Power and Propulsion Society*, 1:5D19RH, 2017.
- [37] T. Hoffmann, Panning L., and J. Wallaschek. Modelling friction characteristics in turbine blade vibrations using a fourier series expansion of a real friction hysteresis. *Procedia engineering*, 199:669–674, 2017.
- [38] C. Pierre, A. A. Ferri, and E. H. Dowell. Multi-harmonic analysis of dry friction damped systems using an incremental harmonic balance method. *Journal of applied mechanics*, 52(4):958–964, 1985.
- [39] L. Salles, L. Blanc, F. Thouverez, A. M. Gouskov, and P. Jean. Dual time stepping algorithms with the high order harmonic balance method for contact interfaces with fretting-wear. *Journal of Engineering for Gas Turbines and Power*, 134(3):032503, 2012.
- [40] C. Siewert, L. Panning, J. Wallaschek, and C. Richter. Multiharmonic forced response analysis of a turbine blading coupled by nonlinear contact forces. *Journal of Engineering for Gas Turbines and Power*, 132(8):082501, 2010.
- [41] A. Grolet and F. Thouverez. On a new harmonic selection technique for harmonic balance method. *Mechanical Systems and Signal Processing*, 30:43–60, 2012.
- [42] C. M. Firrone, D. Botto, and M. M. Gola. Modelling a friction damper: analysis of the experimental data and comparison with numerical results. In *ASME 8th Biennial Conference on Engineering Systems Design and Analysis*, pages 469–478. American Society of Mechanical Engineers, 2006.
- [43] D. Süß, M. Jerschl, and K. Willner. Adaptive harmonic balance analysis of dry friction damped systems. In *Nonlinear Dynamics, Volume 1*, pages 405–414. Springer, 2016.
- [44] E. J. Berger. Friction modeling for dynamic system simulation. *Applied Mechanics Reviews*, 55(6):535–577, 2002.
- [45] W. D. Iwan. A distributed-element model for hysteresis and its steady-state dynamic response. *Journal of Applied Mechanics*, 33(4):893–900, 1966.
- [46] W. D. Iwan. On a class of models for the yielding behavior of continuous and composite systems. *Journal of Applied Mechanics*, 34(3):612–617, 1967.
- [47] D. J. Segalman. A four-parameter iwan model for lap-type joints. *Journal of Applied Mechanics*, 72(5):752–760, 2005.
- [48] M. R. W. Brake. A reduced Iwan model that includes pinning for bolted joint mechanics. *Nonlinear Dynamics*, 87(2):1335–1349, 2017.

- [49] L. Dongwu and X. Chao. Modelling of mechanical systems with friction interfaces considering variable normal contact load and tangential micro/macro slip. In *ASME 2016 International Mechanical Engineering Congress and Exposition*, pages V04BT05A017–V04BT05A017. American Society of Mechanical Engineers, 2016.
- [50] B. J. Deaner, M. S. Allen, M. J. Starr, D. J. Segalman, and H. Sumali. Application of viscous and iwan modal damping models to experimental measurements from bolted structures. *Journal of Vibration and Acoustics*, 137(2):021012, 2015.
- [51] J. D. Reid and N. R. Hiser. Detailed modeling of bolted joints with slippage. *Finite elements in analysis and design*, 41(6):547–562, 2005.
- [52] M. Allen, R. L. Mayes, and D. Rixen. *Dynamics of Coupled Structures, Volume 4: Proceedings of the 34th IMAC, A Conference and Exposition on Structural Dynamics 2016*. Springer, 2016.
- [53] E.P. Petrov and D.J. Ewins. Generic friction models for time-domain vibration analysis of bladed discs. In *ASME Turbo Expo 2003, collocated with the 2003 International Joint Power Generation Conference*, pages 223–233. American Society of Mechanical Engineers, 2003.
- [54] D. Li, C. Xu, T. Liu, M. M. Gola, and L. Wen. A modified iwan model for micro-slip in the context of dampers for turbine blade dynamics. *Mechanical Systems and Signal Processing*, 121:14–30, 2019.
- [55] B. D. Yang, M. L. Chu, and C. H. Menq. Stick–slip–separation analysis and non-linear stiffness and damping characterization of friction contacts having variable normal load. *Journal of Sound and vibration*, 210(4):461–481, 1998.
- [56] E. P. Petrov and D. J. Ewins. Analytical formulation of friction interface elements for analysis of nonlinear multi-harmonic vibrations of bladed disks. *ASME. J. Turbomach.*, 125(2):364–371, 2003.
- [57] K. Y. Sanliturk and D. J. Ewins. Modelling two-dimensional friction contact and its application using harmonic balance method. *Journal of sound and vibration*, 193(2):511–523, 1996.
- [58] C. H. Menq and B. D. Yang. Non-linear spring resistance and friction damping of frictional constraint having two-dimensional motion. *Journal of Sound and Vibration*, 217(1):127–143, 1998.
- [59] B. D. Yang and C. H. Menq. Characterization of 3d contact kinematics and prediction of resonant response of structures having 3d frictional constraint. *Journal of Sound and Vibration*, 217(5):909–925, 1998.
- [60] S. Zucca, D. Botto, and M.M. Gola. Range of variability in the dynamics of semi-cylindrical friction dampers for turbine blades. In *ASME Turbo Expo: Power for Land, Sea, and Air*, volume 5: Structures and Dynamics, Parts A and B, pages 519–529, 2008.

- [61] E. Cigeroglu, N. An, and C. H. Menq. Forced response prediction of constrained and unconstrained structures coupled through frictional contacts. *J. Eng. Gas. Turbines Power-Trans. ASME*, 131(2):022505–022505–11, 2009.
- [62] E. P. Petrov. A high-accuracy model reduction for analysis of nonlinear vibrations in structures with contact interfaces. *Journal of Engineering for Gas Turbines and Power*, 133(10):102503, 2011.
- [63] B. Besselink, U. Tabak, A. Lutowska, N. Van, H. Nijmeijer, D. J. Rixen, M. E. Hochstenbach, and W. H. A. Schilders. A comparison of model reduction techniques from structural dynamics, numerical mathematics and systems and control. *Journal of Sound and Vibration*, 332(19):4403–4422, 2013.
- [64] R. Craig and M. Bampton. Coupling of substructures for dynamic analyses. *AIAA journal*, 6(7):1313–1319, 1968.
- [65] W. C. Hurty. Dynamic analysis of structural systems using component modes. *AIAA journal*, 3(4):678–685, 1965.
- [66] D. J. Segalman. Model reduction of systems with localized nonlinearities. *Journal of Computational and Nonlinear Dynamics*, 2(3):249–266, 2007.
- [67] S. Zucca and B. I. Epureanu. Bi-linear reduced-order models of structures with friction intermittent contacts. *Nonlinear Dynamics*, 77(3):1055–1067, 2014.
- [68] I. A. Sever, E. P. Petrov, and D. J. Ewins. Experimental and numerical investigation of rotating bladed disk forced response using underplatform friction dampers. *J. Eng. Gas. Turbines Power-Trans. ASME*, 130(4):042503–11, 2008.
- [69] W. Sextro, K. Popp, and I. Wolter. Improved reliability of bladed disks due to friction dampers. In *ASME Turbo Expo: Power for Land, Sea, and Air*, volume 4: Manufacturing Materials and Metallurgy; Ceramics; Structures and Dynamics; Controls, Diagnostics and Instrumentation; Education, page V004T14A035, Orlando, Florida, USA, 1997.
- [70] A. Bessone, F. Toso, and T. Berruti. Investigation on the dynamic response of blades with asymmetric under platform dampers. In *ASME Turbo Expo: Power for Land, Sea, and Air*, volume 7B: Structures and Dynamics, page V07BT33A003, Montreal, Quebec, Canada, 2015.
- [71] F Pfeiffer and M Hajek. Stick-slip motion of turbine blade dampers. *Phil. Trans. R. Soc. Lond. A*, 338(1651):503–517, 1992.
- [72] B. D. Yang and C. H. Menq. Characterization of contact kinematics and application to the design of wedge dampers in turbomachinery blading: Part 1 - stick-slip contact kinematics. *J. Eng. Gas. Turbines Power-Trans. ASME*, 120(2):410–417, 1998.

- [73] K. H. Koh and J. H. Griffin. Dynamic behavior of spherical friction dampers and its implication to damper contact stiffness. *Journal of Engineering for Gas Turbines and Power*, 129(2):511–521, 2007.
- [74] L. Panning, W. Sextro, and K. Popp. Optimization of interblade friction damper design. In *ASME Turbo Expo: Power for Land, Sea, and Air*, volume 4: Manufacturing Materials and Metallurgy; Ceramics; Structures and Dynamics; Controls, Diagnostics and Instrumentation; Education, page V004T03A068, Munich, Germany, 2000.
- [75] C. H. Menq, J. H. Griffin, and J. Bielak. The influence of microslip on vibratory response, part ii: A comparison with experimental results. *J. Sound Vibr.*, 107(2):295–307, 1986.
- [76] J. Szwedowicz, C. Gibert, T. P. Sommer, and R. Kellerer. Numerical and experimental damping assessment of a thin-walled friction damper in the rotating setup with high pressure turbine blades. *J. Eng. Gas. Turbines Power-Trans. ASME*, 130(1):012502–012510, 2008.
- [77] T. Berruti. A test rig for the investigation of the dynamic response of a bladed disk with underplatform dampers. *Mech. Res. Commun.*, 37(6):581–583, 2010.
- [78] C.M. Firrone. Measurement of the kinematics of two underplatform dampers with different geometry and comparison with numerical simulation. *J. Sound Vibr.*, 323:313–333, 2009.
- [79] L. Pesaresi, L. Salles, A. Jones, J. Green, and C. Schwingshackl. Modelling the nonlinear behaviour of an underplatform damper test rig for turbine applications. *Mech. Syst. Signal Proc.*, 85:662–679, 2017.
- [80] K. Y. Sanliturk, A. B. Stanbridge, and D. J. Ewins. Friction dampers: measurement, modelling and application to blade vibration control. In *Proceeding of Design Engineering Technology Conferences*, pages 84–2, 1995.
- [81] C.W. Schwingshackl, E.P. Petrov, and D.J. Ewins. Validation of test rig measurements and prediction tools for friction interface modelling. In *ASME Turbo Expo: Power for Land, Sea, and Air*, volume 6: Structures and Dynamics, Parts A and B, pages 1015–1024, 2010.
- [82] M. Lavella, D. Botto, and M. M. Gola. Test rig for wear and contact parameters extraction for flat-on-flat contact surfaces. In *ASME/STLE International Joint Tribology Conference*, pages 307–309, 2011.
- [83] D. Botto, M. Lavella, and M. M. Gola. Measurement of contact parameters of flat on flat contact surfaces at high temperature. In *ASME Turbo Expo: Power for Land, Sea, and Air*, volume 7: Structures and Dynamics, Parts A and B, pages 1325–1332. ASME, 2012.

- [84] M. Lavella, D. Botto, and M. M. Gola. Design of a high-precision, flat-on-flat fretting test apparatus with high temperature capability. *Wear*, 302:1073–1081, 2013.
- [85] D. Botto, A. Campagna, M. Lavella, and M. Gola. Experimental and numerical investigation of fretting wear at high temperature for aeronautical alloys. In *ASME Turbo Expo: Power for Land, Sea, and Air*, volume 6: Structures and Dynamics, Parts A and B, pages 1353–1362. ASME, 2010.
- [86] D. Botto and M. Lavella. A numerical method to solve the normal and tangential contact problem of elastic bodies. *Wear*, 330-331:629–635, 2015.
- [87] M. M. Gola, M. Bragas dos Santos, and T. Liu. Measurement of the scatter of underplatform damper hysteresis cycle: experimental approach. In *ASME International Design Engineering Technical Conferences and Computers and Information in Engineering Conference*, volume 1, pages 359–369, 2012.
- [88] D. Botto and M. Umer. A novel test rig to investigate under-platform damper dynamics. *Mech. Syst. Signal Proc.*, 100:344–359, 2018.
- [89] G. Csaba and M. Andersson. Optimization of friction damper weight, simulation and experiments. In *Turbo Expo: Power for Land, Sea, and Air*, volume 4, page V004T14A031, Florida, USA, 1997.
- [90] D. Botto, S. Zucca, S. Pavone, and M. Gola. Parametric study of the kinematic behaviour of the underplatform damper and correlation with experimental data. In *International Conference on Noise and Vibration Engineering ISMA 2008*, Leuven-Belgium, 2008.
- [91] S. Zucca, T. Berruti, and L. Cosi. Experimental and numerical investigations on the dynamic response of turbine blades with tip pin dampers. *Journal of physics. Conference Series*, 744(1), 2016.
- [92] C. Gastaldi and T. M. Berruti. A method to solve the efficiency-accuracy trade-off of multi-harmonic balance calculation of structures with friction contacts. *International Journal of Non-Linear Mechanics*, 92:25–40, 2017.
- [93] T. M. Cameron, J. H. Griffin, R. E. Kielb, and T. M. Hoosac. An integrated approach for friction damper design. *Journal of Vibration and Acoustics*, 112(2):175–182, 1990.
- [94] B. D. Yang and C. H. Menq. Characterization of contact kinematics and application to the design of wedge dampers in turbomachinery blading: Part 2 – prediction of forced response and experimental verification. *J. Eng. Gas. Turbines Power-Trans. ASME*, 120(2):418–423, 1998.
- [95] S.S. Chen and A.A. Sinha. Probabilistic method to compute the optimal slip load for a mistuned bladed disk assembly with friction dampers. *ASME. J. Vib. Acoust.*, 112(2):214–221, 1990.

- [96] L. Pesaresi, L. Salles, A. Jones, J. S. Green, and C. W. Scwingshackl. Numerical and experimental investigation of an underplatform damper test rig. *Applied Mechanics and Materials*, 849:1–12, 2016.
- [97] C Gastaldi. *Vibration control and mitigation in Turbomachinery*. PhD thesis, Ph. D. thesis, Politecnico di Torino, Turin, Italy, 2017.
- [98] R. D. Mindlin. Compliance of elastic bodies in contact. *J. Appl. Mech., ASME*, 16:259–268, 1949.
- [99] D. Wang, C. Xu, X. Fan, and Q. Wan. Reduced-order modeling approach for frictional stick-slip behaviors of joint interface. *Mechanical Systems and Signal Processing*, 103:131–138, 2018.
- [100] M. M Gola, T. Liu, and M. Bragas Dos Santos. Investigation of under-platform damper kinematics and its interaction with contact parameters (nominal friction coefficient). In *5th World Tribology Congress*, 2013.
- [101] C. Gastaldi and M. M. Gola. An improved microslip model for variable normal loads. In *Proceedings of the 9th IFToMM International Conference on Rotor Dynamics*, pages 169–179. Springer, 2015.
- [102] C. Gastaldi, T. M. Berruti, and M. M. Gola. The relevance of damper pre-optimization and its effectiveness on the forced response of blades. *Journal of Engineering for Gas Turbines and Power*, 140(6):062505, 2018.
- [103] NTN. *NTN Needle Roller Bearing handbook*, chapter Needle Roller Bearing, page 8. Cat. No. 9013/A. NTN.BEARING CORPORATION, 2009.
- [104] K.L. Johnson. *Contact Mechanics*, chapter Non-Hertzian elastic contact of conforming bodies, pages 114–118. Cambridge University Press, UK, 1985.
- [105] *Instruction Manual , Press force sensors Type 9323AA,9323A, 9333A, Type 9323AA,9323A, 9333A, 9343A, 9363A, 9383A, 9393A9343A, 9363A, 9383A, 9393A by KISTLER.*
- [106] P. Pennacchi, S. Chatterton, N. Bachschmid, E. Pesatori, and G. Turozzi. A model to study the reduction of turbine blade vibration using the snubbing mechanism. *Mechanical Systems and Signal Processing*, 25(4):1260–1275, 2011.
- [107] D. Botto, C. Gastadi, M. M. Gola, and M. Umer. An experimental investigation of the dynamics of a blade with two under-platform dampers. *J. Eng. Gas Turbines Power*, 140(3):032504–032509, 2017.
- [108] D. Botto, C. Gastaldi, M. M. Gola, and M. Umer. Experimental study of under-platform damper kinematics in presence of blade dynamics. *IOP Conference Series: Materials Science and Engineering*, 302:012016, 2018.

- 
- [109] C. Gastaldi and M. M. Gola. Testing, simulating and understanding underplatform damper dynamics. In *Proceedings of the VII European Congress on Computational Methods in Applied Sciences and Engineering (ECCOMAS Congress 2016)*, 2016.
- [110] C. M. Firrone and S. Zucca. *Numerical Analysis-Theory and Application*, chapter Modelling Friction Contacts in Structural Dynamics and its Application to Turbine Bladed Disks, pages 301–334. InTech, 2011.
- [111] C. M. Firrone, S. Zucca, and M.M. Gola. The effect of underplatform dampers on the forced response of bladed disks by a coupled static/dynamic harmonic balance method. *Int. J. Non-Linear Mech.*, 46(2):363–375, 2011.

# Appendix A

## Appendix to Chap. 2

### A.1 Sensors

Following sensors are used and attached with the test rig to perform different experimental activities during this study.

- Accelerometers to measure the blade vibration amplitude
- Load cells to measure the damper contact forces
- Electromagnetic shaker to excite the blade
- Impact Hammer
- Strain gage based force transducer to measure blade clamping force
- Load cell to measure and control the shaker excitation force
- Single point laser to measure velocity or displacement of a point
- double point differential doppler laser (resolution  $20nm$ ) to measure relative velocity or displacement between two point of a vibrating structure-Polytec OFV-512 as shown in Fig. [A.16](#).

The calibration certificates of all the above mentioned sensors are given at the end of this appendix chapter.



## A.2 Friction loss calculation in the blade clamp

The complete derivation of the actual clamp force given in Eq. 2.1 to define the overall efficiency of the clamp mechanism can be obtained as follows with refer to the Fig. A.1:

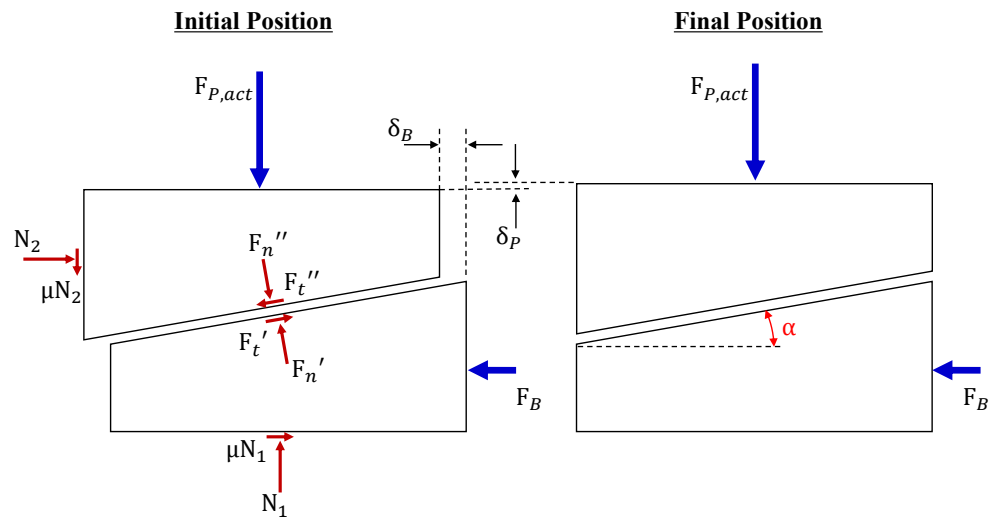


Fig. A.1 Clamp forces free body diagram.

$$\delta_n' = \delta_n'' = \delta_A \sin \alpha$$

$$\delta_t' = \delta_B \cos \alpha$$

$$\delta_t'' = \delta_n'' \tan \alpha$$

$$\delta_t'' = \delta_n' \tan \alpha$$

$$\delta_t'' = \delta_B \sin \alpha \tan \alpha$$

$$\delta_P = \sqrt{(\delta_t'')^2 + (\delta_n'')^2}$$

$$\delta_P = \delta_B \tan \alpha$$

### **Lower wedge block**

$$F_B \delta_B - \mu N_1 \delta_B - F_n \delta_n' - F_t \delta_t' = 0$$

$$F_B \delta_B - \mu (\cos \alpha - \mu \sin \alpha) \delta_B - F_n \delta_B \sin \alpha - F_t \delta_B \cos \alpha = 0$$

$$F_t = \mu F_n$$

$$F_B \delta_B - \mu (\cos \alpha - \mu \sin \alpha) \delta_B - F_n \delta_B \sin \alpha - \mu F_n \delta_B \cos \alpha = 0$$

$$F_n = \frac{F_B}{\sin \alpha + 2\mu \cos \alpha - \mu^2 \sin \alpha}$$

### **Upper wedge block**

$$F_{P,act} \delta_P + \mu N_2 \delta_P - F_n \delta_n'' + F_t \delta_t'' = 0$$

$$F_{P,act} \delta_B \tan \alpha + \mu N_2 \delta_P - F_n \delta_n'' + F_t \delta_t'' = 0$$

$$F_{P,act} \delta_B \tan \alpha + \mu F_n (\sin \alpha + \mu \cos \alpha) \delta_B \sin \alpha - F_n \delta_B + F_t \delta_t'' \sin \alpha + \mu F_n \sin \alpha \tan \alpha = 0$$

$$F_{P,act} = F_n (\sin \alpha + 2\mu \sin \alpha - \mu^2 \cos \alpha)$$

$$F_{P,act} = \frac{\cos \alpha - 2\mu \sin \alpha - \mu^2 \cos \alpha}{\sin \alpha + 2\mu \sin \alpha - \mu^2 \sin \alpha} F_B$$

## A.3 Contact force formulation

As explained in Chap. 2 that each damper is in contact with the blade on one side and on the other side with fixed platform of the force measurement system that forms a rigid support. As shown in Figs. 2.12 and 2.13, the measured contact forces are then post processed by applying static force equilibrium on the damper to compute tangential and normal contact force components of the both contact interfaces of the damper. The final outcome of this post processing is given in Table. 2.1 whereas, each step of the formulation with refer to the corresponding force triangle is given as follows:

### A.3.1 ODD SIDE

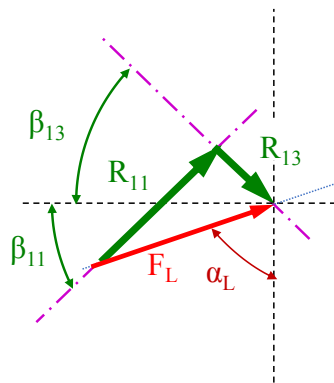


Fig. A.2 Forces on the L-Separator; odd load cells LC11/LC13-1

From Figure A.2

$$\beta_{13}^* = \beta_{13} + \delta_L$$

$$\beta_{11}^* = \beta_{11} - \delta_P$$

$$F_L = \sqrt{R_{11}^2 + R_{13}^2}$$

$$\sin \alpha_L = \frac{R_{11} \cos \beta_{11} + R_{13} \cos \beta_{13}}{F_L}$$

$$\cos \alpha_L = \frac{R_{11} \sin \beta_{11} - R_{13} \sin \beta_{13}}{F_L}$$

$$\alpha_L = \arctan(\cos \alpha_L, \sin \alpha_L)$$

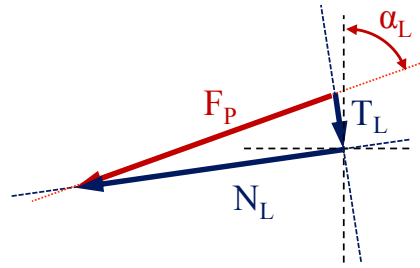


Fig. A.3 Forces on the L-Separator; odd load cells LC11/LC13-2

From Figure A.3

$$N_L = F_L \cos\left(\left(\frac{\pi}{2} - \alpha_P\right) - \delta_L\right)$$

$$T_L = F_L \sin\left(\left(\frac{\pi}{2} - \alpha_L\right) - \delta_L\right)$$

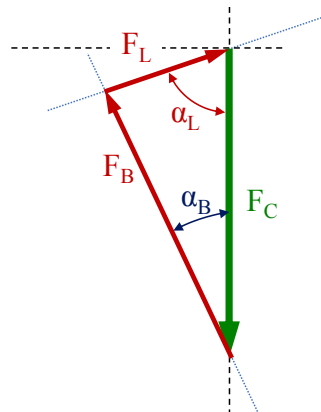


Fig. A.4 Forces on the damper; odd load cells LC11/LC13-3

From Figure A.4

$$F_B = \sqrt{F_C^2 + F_L^2 - 2F_C F_L \cos \alpha_L}$$

$$\sin \alpha_L = F_L \frac{F_C - F_B \cos \alpha_B}{F_B}$$

$$\alpha_B = \arctan(\cos \alpha_B, \sin \alpha_B)$$

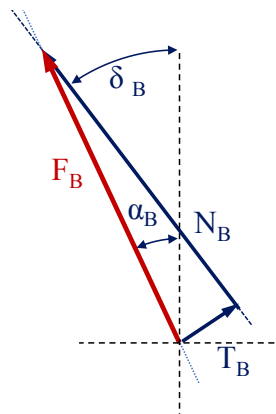


Fig. A.5 Forces on the damper; odd load cells LC11/LC13-4

From Figure A.5

$$N_B = F_B \cos(\alpha_B - \delta_B)$$

$$T_B = F_B \sin(\alpha_B - \delta_B)$$

### A.3.2 EVEN SIDE

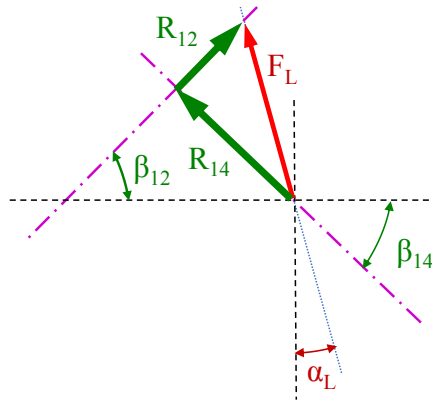


Fig. A.6 Forces on the L-Separator; Even load cells LC12/LC14-1

From Figure A.6

$$F_L = \sqrt{R_{12}^2 + R_{14}^2}$$

$$\sin \alpha_L = \frac{R_{14} \cos \beta_{14} - R_{12} \cos \beta_{12}}{F_L}$$

$$\cos \alpha_L = \frac{R_{12} \sin \beta_{12} + R_{14} \sin \beta_{14}}{F_L}$$

$$\alpha_L = \arctan(\cos \alpha_L, \sin \alpha_L)$$

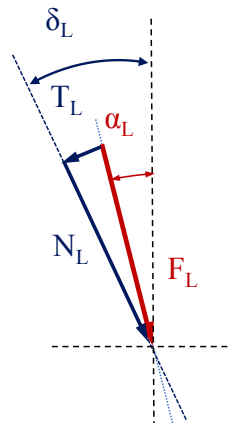


Fig. A.7 Forces on the L-Separator; Even load cells LC12/LC14-2

From Figure A.7

$$N_L = F_L \cos(\delta_L - \alpha_L)$$

$$T_L = F_L \sin(\delta_L - \alpha_L)$$

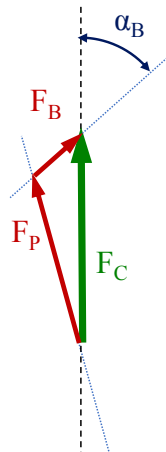


Fig. A.8 Forces on the damper; Even load cells LC12/LC14-3

From Figure A.8

$$F_B = \sqrt{F_C^2 + F_L^2 - 2F_C F_L \cos \alpha_L}$$

$$\sin \alpha_B = F_L \frac{\sin \alpha_L}{F_B}$$

$$\cos \alpha_B = \frac{F_C - F_L \cos \alpha_L}{F_B}$$

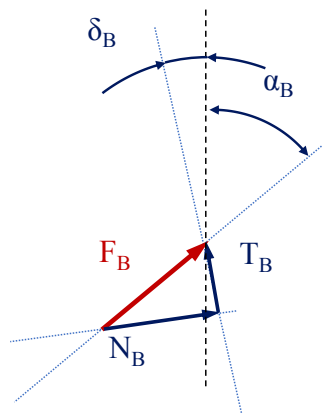


Fig. A.9 Forces on the damper; Even load cells LC12/LC14-4

From Figure A.9

$$N_B = F_B \cos((\frac{\pi}{2} - \alpha_B) - \delta_B)$$

$$T_B = F_B \sin((\frac{\pi}{2} - \alpha_B) - \delta_B)$$

## A.4 Important things to consider before experiments

1. Before starting any experiment, ensure that blade is clamped at a required clamping force and is in a right position (middle of the adapter groove). HBM



software (Quantum X Assistant) installed in lab PC will provide clamping force value through the strain gauge based load cell of the clamp mechanism. The displayed value is required to be multiplied by the correct amplification factor of the clamp due to slope of wedge blocks as explained in Chap. 2 Sec. 2.2.1. The clamping force indicated by the software is in “KN”

2. Always turn on respective Data Acquisition System (DAS-I or DAS-II) before starting the PC in both cases according to the required test.
3. After selecting the type of sensor (measured quantity), add the correct value of sensitivity and range of the sensor with correct units in the channel setup of the data acquisition systems.
4. Before generating the signal with NI-card and FGen i.e. while using DAS-II, ensure to set a very high “output impedance” (say >1M $\Omega$ ) in the device configuration of FGen software control panel.
5. Also it is suggested to verify the signal generated by the FGen with the help of any scope before connecting the data acquisition system DAS-II directly to the shaker. This additional step ensures the prevention of any sudden or abrupt damages to the connected structure in case of false signal generated by FGen.
6. In case of DAS-II, ensure all the respective I/P or O/P channels are connected properly and are designated with the correct number in the NI software “Signal Express” (“ai or ao” written on the NI card mean analogue input/output respectively).
7. It is recommended to turn on “reaction force measuring load cell amplifiers” as well as NI card for around 20-30 minutes before starting any experiment to get a more reliable reading of damper contact forces.
8. While exciting the shaker with signal generator, initially put the amplifier connected with shaker at a smaller master gain value of 2 or 3. and gradually increase the knob of the amplifier to increase/adjust the excitation force at the required level.
9. To get the readings of reaction forces from the load cells, press “Measure” button on the amplifier of the corresponding load cell before loading the dampers.

10. While measuring the relative displacement with the differential laser, press “Clear” button on the laser device to reset the signal.
11. Always perform a dummy measurement before starting any experiment with the lower excitation level initially. After ensuring that all the sensors and accessories connected with the test rig are working properly, proceed with the full experimental campaign.

## **A.5 Overall characteristics of the Novel Test Rig**

The test rig possesses following features:

1. it is rigid enough to work at higher frequency of approximately 5000 Hz
2. clamping of the blade is done by pushing it from its bottom at its root which allows to simulate the actual centrifugal force experienced by the blade while turbine runs.
3. a strain gage based load cell is placed between main bolt and lower wedge block to measure and control the clamping force applied on the blade
4. linear flat roller bearings are introduced between the wedge block sliding surfaces to minimize the friction losses
5. by simply substituting the adapter of turbine blade and damper platforms, we are able to test a number of blades and dampers on a single test rig
6. test rig includes a contact force measurement mechanism for each damper which is capable to measure both static and dynamic components of the damper contact forces along normal and tangential direction
7. a self-aligning pin was placed between the pushing block and upper wedge to allow a uniform clamping force at the bottom of the blade root even if a small misalignment is present between two wedges of the clamp
8. “Nord-Lock Washers” were used with all assembly fastening screws and bolts to minimize the structural vibration. These washers increase the over all stiffness of the rig and support it to work at higher frequencies.



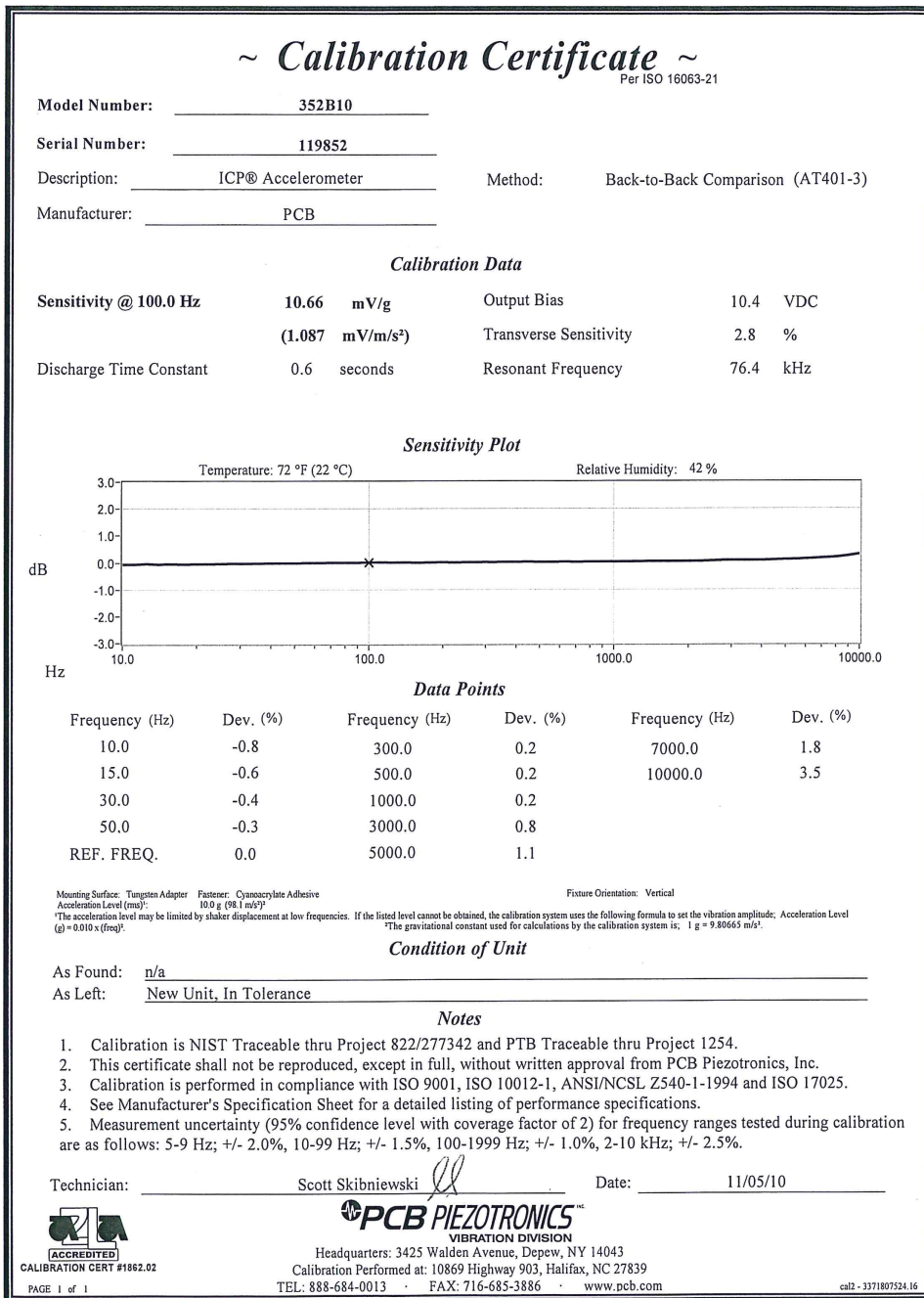



Fig. A.11 Accelerometer1 to measure blade response



## Prüfprotokoll

test certificate / protocole d'essai



---

Typ: type / type	C9C	Auftrag: order no / commission	801222937
Nennmessbereich: range / portée	50 kN	Prüfer: examiner / contrôleur	Sawal
IdentNr: serial no / N° ident	190210327	Datum: test date / date d'essai	2015-01-29

---

**Prüfergebnisse:**  
test results / résultats d'essai

Eingangsgröße des Messbereichs [%] input quantity / échelle d'essai	Ausgangsgröße [mV/V] output quantity / résultats
	Druck compression / compression
0	0.0000
50	0.5005
100	0.9999
50	0.5003
0	-0.0001

---

**Aus den Prüfergebnissen berechnete messtechnische Kenngrößen:**  
Metrological characteristic quantities computed from the test results:  
Grandeurs caractéristiques de mesure calculées à partir des résultats d'essai :

Kennwert C [mV/V] sensitivity / sensibilité	0.9999
Linearitätsabweichung [%vC] linearity deviation / linéarité (Abweichung von der bestpassenden Geraden durch das Nullsignal) (deviation from best fit through zero / écart par rapport à la meilleure droite passant par le zéro)	0.033
Relative Umkehrspanne 0,5 Fnom [%vC] relative hysteresis / hystérésis relatif	-0.019

Alle aus den Messergebnissen ermittelten Kenngrößen entsprechen den Spezifikationen gemäß Datenblatt.  
All characteristic quantities determined from the measurement results correspond to the specifications per datasheet.  
Toutes les grandeurs caractéristiques déterminées à partir des résultats de mesure correspondent aux spécifications selon les caractéristiques techniques.

---

**Allgemeine Zusatzinformationen:**  
general information / informations complémentaires

Alle weiteren messtechnischen Eigenschaften des Aufnehmers sind durch Typprüfungen und laufende Produktaudits des Qualitätswesens abgesichert.  
All other metrological characteristics of the transducer are verified by type testing and regular product audits of the quality department.  
Toutes les autres caractéristiques techniques du capteur sont garanties par le Service Qualité, au moyen d'essais et d'audits suivis sur le produit.

Hottinger Baldwin Messtechnik GmbH, Im Tiefen See 45, 64293 Darmstadt, Germany | www.hbm.com  
Registered as GmbH (German limited liability corporation) in the commercial register at the local court of Darmstadt, HRB 1147  
Company domiciled in Darmstadt | CEO: Andreas Hüllhorst | Chairman of the board: James Charles Webster

Zertifiziert nach ISO 9001 und ISO 14001 / ISO 9001 and ISO 14001 certified / Certification selon ISO 9001 et ISO 14001  
Akkreditierungen gemäß ISO 17025 / Accreditations per ISO 17025 / Accréditations selon ISO 17025

Nr. 230 Seite / Page 1 (1)

Fig. A.13 strain gage based load cell to measure the clamping force



Fig. A.14 Load cell amplifiers to measure damper contact force measurements 1



Fig. A.15 Load cell amplifiers to measure damper contact force measurements 1





Fig. A.16 Differential laser polytec sensor head with vibrometer controller

# Appendix B

## Appendix to Chap. 3

### B.1 Design details of the Dummy blade

Dummy blade was designed according to the required modal and dynamic properties mentioned in **Chap.3**. However, few additional design constraints were imposed by the test rig itself due to assembly and configuration of contact force measurement mechanism. The detail drawings of the dummy blade are given below in Fig. [B.1](#) and [B.2](#).

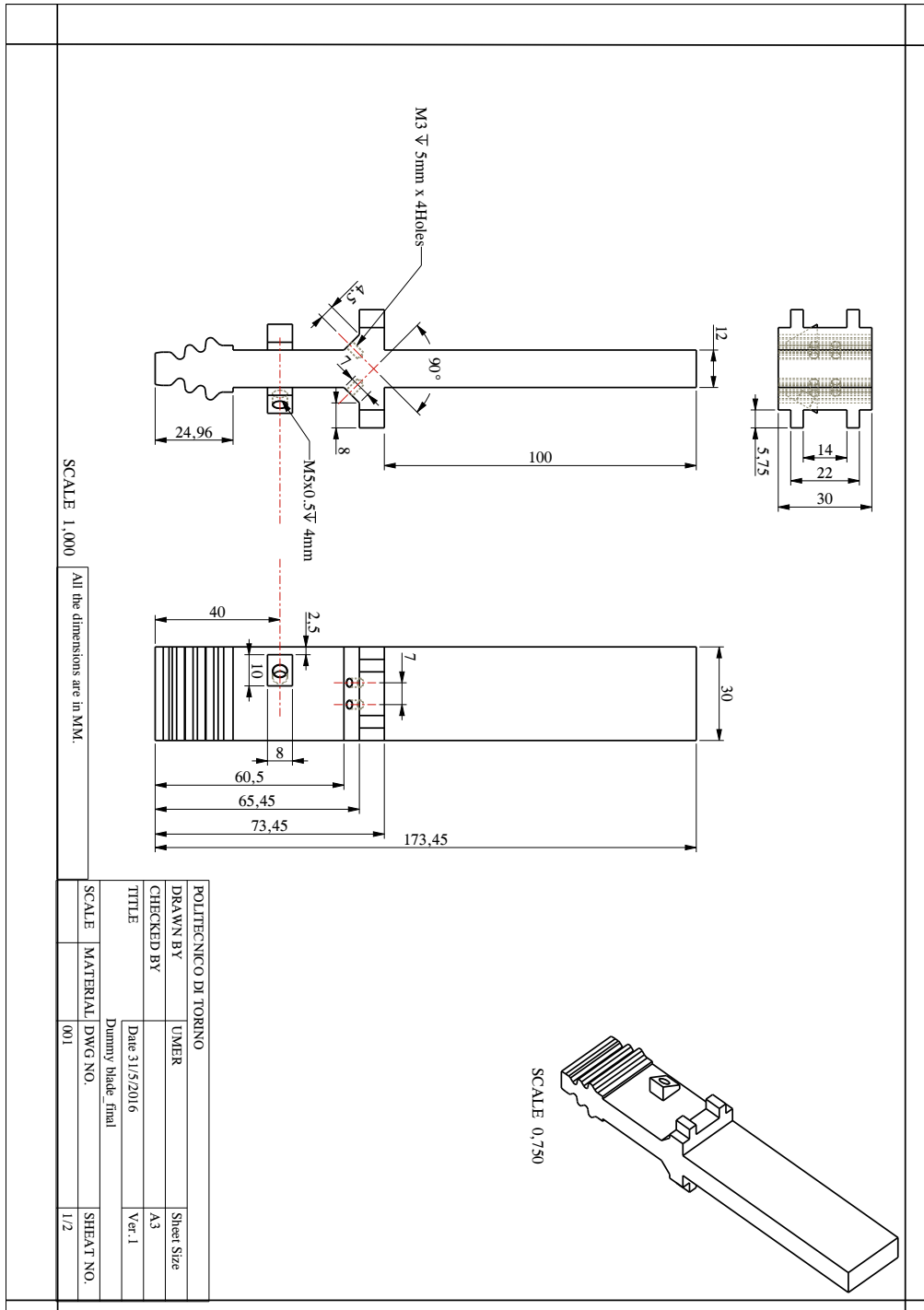


Fig. B.1 dummy blade drawing 1/2



# Appendix C

## Appendix to Chap. 4

### C.1 Dummy blade FE Model

With refer to Fig. 4.5, the following nodes are selected as master nodes:

- (A) 1-acceleration node (response/output node) where the accelerometer is placed on the blade as shown in Fig.5.2 a.
- (B) 16-contact nodes on the blade platforms (4 corresponds to each contact pad where the damper flat surface interact with the blade)
- (C) 1-excitation node (input node) is selected corresponding to the position of the shaker stinger as shown in Fig. 5.2 a.

Although we are working on only first resonance peak and corresponding mode of the blade but first 50 modes of the blade are extracted in the reduced model to avoid any potential error due to this reduction. The reduced model of the blade (mass and stiffness matrices) can be further imported in the MATLAB and used to simulate the hysteresis loops by introducing a valid contact model at the selected blade contact nodes. The total imported size of the blade in terms of d.o.f was :  $N_{\text{dof}} = 50 + 3 * (1 + 1 + 16) = 104$ .

## C.2 Real blade FE Model

The physical properties of the real turbine blade are as follows:

- Material = single crystal (SX) turbine airfoil alloy
- Volume = 52024 mm<sup>3</sup>
- Mass = 0.44209 kg

Following are the details about the full and reduced order blade model.

- **No. of elements of full blade model** = 27334
- **No. of Nodes of full blade model** = 47991
- **Selected master nodes**
  - Excitation node = 1
  - Response node = 1
  - Right contact nodes = 7
  - Left contact nodes = 7
  - Right root nodes = 94
  - Left root nodes = 95
- **No. of elements of the reduced blade model** = 120
- **No. of Nodes of reduced blade model** = 205

# Appendix D

## Appendix to Chap. 6

### D.1 Experimental procedure to measure FRFs and Hysteresis Loops

In these experiments, a static normal force  $F_C$  simulates the centrifugal load experienced by the dampers during actual working conditions of a turbine. The experimental results presented in **Chap. 6** Sec. 6.4 were obtained in two phases. In the first phase standard frequency response functions were measured while loading the damper with three static force levels  $F_C$ , i.e 6, 26 and 96 N. Several FRFs were measured at different excitation force values  $F_E$  for each static force level of the dampers. An electromagnetic shaker was used to excite the blade, through a stinger attached close to the blade root, at the desired frequency range and excitation force. The excitation force  $F_E$ , applied as stepped-sine signal, ranged from 1 to 15 N. It was not possible to excite the blade higher than 15 N for given frequency range because the available commercial code was unable to control the force within a tolerance of 0.5 db. In this part of the experiments, blade structure was excited for a given frequency range with a stepped-sine force signal  $F_E$  to investigate blade first resonance mode. The second phase of the testing was conducted to measure the contact forces and relative kinematics, namely displacement  $\delta$  and velocity  $\dot{\delta}$ , between the blade and the damper. The static normal force  $F_C$  on the dampers and excitation force  $F_E$  on the blade were applied at the same amplitude levels as in the first phase of the experiments. However, this time the excitation force was a

sinusoidal signal of single frequency corresponding to the resonance frequency of the blade. The blade acceleration was also recorded and controlled to ensure that the contact variable were measured at the same dynamic conditions as observed in the first phase of the experiment. The contact forces and relative kinematics, measured in the time domain, were post-processed to compute an equivalent tangential stiffness ( $K_{eq}$ ) and equivalent tangential damping ( $C_{eq}$ ) of the contact. The procedure to compute the equivalent contact characteristics is described in Sec. 6.3 .

This complete experimental campaign was split into two phases because it was not possible to work in the time and frequency domain with the two Data Acquisition Systems (DAS) simultaneously connected to the test rig. The details to simultaneously utilized the two different and independent DAS, namely DAS-I and DAS-II has been explained in **Chap. 2** Sec. 2.5.

## D.2 Rigid rotation of the damper

Accuracy of equivalent contact stiffness and damping calculated from hysteresis loop depends also on the correctness of the measured damper-blade relative kinematics. Rigid rotation of the damper gives absolute displacements that the measuring system recognizes as relative to the blade if no other reference is available. This rotation of the damper can introduce a significant error in the relative kinematics measurement that affects the subsequent calculations. Therefore, an additional test was performed to measure damper maximum rigid rotation at highest excitation level.

In this experiment, both beams of differential laser were pointed at two extreme points of the damper,  $p_1$  and  $p_2$  at a distance of  $d_0$  as shown in Fig. D.1. During this experiment, the blade was excited at its first resonance frequency with the maximum excitation force. A rigid rotation  $2\beta$  of  $1.59 \times 10^{-4}$  rad was measured as  $2\beta = x/d_0$ , whereas  $x$  is the relative displacement between points  $p_1$  and  $p_2$ . This rigid rotation leads to a very small displacement of  $\pm 0.016 \mu m$  which is negligible with respect to the actually measured relative displacement between the damper and blade. From this measurement it was concluded that such a small rigid rotation of the damper had negligible effect on the results for equivalent contact stiffness and damping.



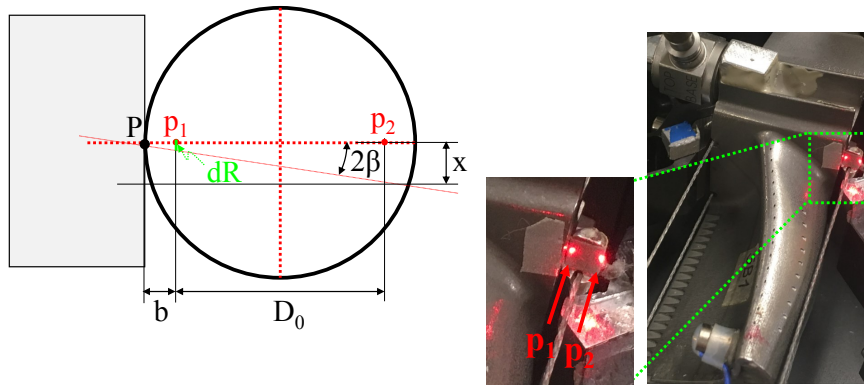


Fig. D.1 Measuring the rigid rotation of the damper with differential laser.  $p_1$  and  $p_2$  are the two points on damper where the beams of differential laser are placed.

